

國立臺灣大學電機資訊學院光電工程研究所

碩士論文

Graduate Institute of Photonics and Optoelectronics
College of Electrical Engineering and Computer Science
National Taiwan University

Master Thesis

以穿透式電子顯微術探討氮化物半導體奈米結構

Investigation of Nitride Semiconductor Nanostructures
with Transmission Electron Microscopy



李仁宏

Jen-Hung Li

指導教授：楊志忠 博士

Advisor: C. C. Yang, Ph.D.

中華民國九十八年七月

July, 2009

國立臺灣大學碩士學位論文
口試委員會審定書

以穿透式電子顯微術探討氮化物半導體奈米結構
Investigation of Nitride Semiconductor
Nanostructures with Transmission Electron
Microscopy

本論文係李仁宏君（學號 R96941080）在國立臺灣大學
光電工程學研究所完成之碩士學位論文，於民國 98 年 7 月
22 日承下列考試委員審查通過及口試及格，特此證明

口試委員：

楊志忠

（指導教授）

黃建璋

吳育仁

所長

黃壯龍

誌謝

首先感謝指導教授楊志忠博士兩年的指導與鼓勵，帶領我進入多采多姿的光電領域，並讓我了解團體中待人處事的道理，而且提供豐富的設備和資源使我得以完成我的研究，在此致上我由衷的感謝。

其次要感謝貴儀中心 300kv FEG TEM 操作技術人員陳學人以及博士後研究員蔡鴻麟學長。此外，還要感謝台大光電所陳永昇學長、張文明學長、廖哲浩學長、已畢業的台大光電所王俊凱學長在試片製作及實驗上給我的建議，讓我可以順利完成我的論文。

接著感謝黃政傑學長、陳志諺學長、盧彥丞學長在磊晶與光學量測方面的協助，以及蕭文裕學長在 XRD 方面的量測，還有博士後研究員黎欣怡(Nola Li)學姊指導我英文技巧，使得這篇論文內容更加完善，再來感謝陳永昇學長、蕭文裕學長、陳正言學長、沈坤慶學長、呂志鋒學長、唐宗毅學長、黃政傑學長、盧彥丞學長、林政宏學長、張文明學長、丁紹滢學長、廖哲浩學長、陳志諺學長、謝劭同學、吳碩彥同學、吳聲霈學弟、黃哲偉學弟、楊凱閔學弟、李俊賢學弟等等這些實驗室的夥伴們在研究生活中相互的鼓勵與討論。

最後要感謝我的家人朋友，不管是精神還是物質上，他們給我相當多的支持和鼓勵，讓我在遭遇挫折或者心情沮喪時還能重新站起，最終能順利地完成碩士學位。謹以此文獻給我的父母、哥哥及女友。

摘要

本論文中的第一部份，是以高解析穿透式電子顯微鏡術，來研究單一和雙重氮化銦鎔/氮化鎔異質結構樣品的奈米結構和光學特性。此兩系列的樣品皆是以有機金屬化學氣相沉積法的方式來成長四片不同厚度的氮化銦鎔層的樣品，分別是25,50,100,和200奈米。由於異質結構所導致的應變和相分離現象，我們利用測量倒置空間圖和光激螢光的結果來了解不同深度下的晶體品質和能隙。在掃描式電子顯微鏡的結果圖中，我們發現當應變開始釋放時，樣品表面的粗糙度會上升。在雙重異質結構的樣品中，由高解析穿透式電子顯微術所得到的影像，我們可以觀察到銦滴的結構，而且發現當氮化銦鎔層的厚度下降時，銦滴的密度也會下降。

在本論文的第二部份，我們來比較兩片不同結構的氮化銦鎔/氮化鎔多層結構的晶體品質。我們利用測量光激螢光的結果發現氮化銦鎔層較薄氮化鎔層較厚的樣品(8奈米-6對)有比較好的光學特性。從高解析穿透式電子式顯微鏡的影像中也發現，(8奈米-6對)樣品的銦分佈較均勻，而且氮化銦鎔和氮化鎔的界面較清晰。透過應力分布分佈軟體去計算氮化銦鎔井內的平均濃度及銦原子濃度的變化範圍，再加上能量散佈光譜儀的測量結果，我們發現在(8奈米-6對)樣品中，氮化銦鎔井內的銦濃度的變化範圍較小。

Abstract

The objective of the proposed research uses high resolution transmission electron microscope (HRTEM) to compare the nanostructures and optical properties of single and double MOCVD-grown InGaN/GaN heterostructures as well as the nanostructures of two InGaN/GaN multi-layers of different structures.

The single and double heterostructures comprised of varying InGaN thicknesses of 25, 50, 100, and 200 nm. RSM and PL measurements demonstrated the depth-dependent crystal quality and band gap due to the effects of heterostructure-induced strain and phase separation in these samples. SEM results showed that as the strain started to relax the surface roughness rose. HRTEM results of the DH samples showed formations of indium droplets depicting a trend where the density of indium droplets decreased as the InGaN thickness decreased.

The second part of this research compared the crystal quality of two InGaN/GaN multi-layers of different structures. PL result implied a better optical quality in the 8nm-6P sample (thinner InGaN thickness and thicker GaN barrier) than in the 10nm-5P sample. HRTEM results showed that the indium distribution was more uniform and the interfaces between the

InGaN wells and GaN barriers were clearer in the 8nm-6P sample than in the 10nm-5P sample. The SSA calibrated average indium contents and indium composition fluctuation, which gave us local information about the two samples. We find that the 8nm-6P sample has a weaker indium composition fluctuation than the 10nm-5P sample based on SSA results. EDX demonstrated the same results as SSA.



Contents

口試委員會審書	I
誌謝	II
中文摘要	III
Abstract	IV
Chapter 1 Introduction.....	1
1.1 Applications of Nitride-Based Materials.....	1
1.2 III-Nitride Materials Growth Issues.....	2
1.2.1 Crystal Structure of III-Nitride Semiconductors.....	2
1.2.2 Substrate for Nitride Epitaxy.....	3
1.2.3 Defects in Nitrides.....	5
1.3 Review on the Characteristics of InGaN/GaN Structures.....	6
1.3.1 Strain Effect.....	6
1.3.2 Piezoelectric Fields.....	7
1.3.3 Spinodal Decomposition and Phase Separation.....	9
1.4 Research Motivation and Research Problems.....	11
Chapter 2 Analysis Methods.....	27
2.1 Specimen Preparation of Cross-section TEM.....	27
2.2 Material Analysis.....	30
2.2.1 High-resolution Transmission Electron Microscopy (HRTEM).....	30

2.2.2	Energy Dispersive X-ray Spectrum (EDX).....	35
2.2.3	Strain-state Analysis (SSA).....	36
2.2.4	X-ray Diffraction (XRD).....	39
2.2.5	Scanning Electron Microscopy (SEM).....	40
2.3	Optical Analysis - Photoluminescence (PL).....	41

**Chapter 3 InGaN/GaN Single-heterostructures (SH)
and Double-heterostructures (DH) With
Various InGaN Thicknesses.....55**

3.1	Sample Growth and Measurement Conditions.....	55
3.2	Strain Conditions of SH and DH Samples.....	56
3.3	InGaN/GaN Single-heterostructures.....	57
3.3.1	XRD and HRTEM Results.....	57
3.3.2	SEM Results.....	58
3.3.3	PL Measurements and EDX Results.....	59
3.4	InGaN/GaN Double-heterostructures.....	60
3.4.1	XRD, HRTEM Results, and SEM Results.....	60
3.4.2	PL Measurements and EDX Results.....	62
3.5	Discussions.....	63

**Chapter 4 Comparison between InGaN/GaN
Multi-layer Samples under Different
Growth Conditions.....87**

4.1 Sample Growth and Measurement Conditions.....	87
4.2 PL and HRTEM Results.....	88
4.3 EDX and SSA Results.....	89
4.4 Discussions.....	92
Chapter 5 Conclusions.....	113
References.....	115



Chapter 1

Introduction

1.1 Applications of Nitride-Based Materials

III-V nitrides have many unique properties, such as wide direct bandgap, high-thermal conductivity, and chemical stability. These properties have made III-V nitrides attractive in recent years. III-nitride semiconductors have been considered for light-emitting device applications in the blue and ultraviolet wavelength ranges because they have a very broad band gap range (see Fig 1.1.1). In fact, III-V nitride-based blue and green light-emitting diodes (LEDs) with an InGaN/GaN multiple-quantum-well (MQW) active region are now commercially available [1]. These nitride-based blue and green LEDs could be used in versatile applications, such as full-color displays, full-color indicators, and traffic lights, etc. Another application of GaN-related compounds is in fabricating blue laser diodes (LDs) for extremely high-density optical storage systems. Because the storage density of optical compact discs (CDs) and digital video discs (DVDs) is inversely proportional to the square of the laser wavelength, a four- to eight-fold increase in capacity can be realized with short-wavelength laser diodes. As the wavelength of the light gets shorter, the focal diameter becomes smaller. The storage density is predicted to go up from today's 1 Gb to about 40 Gb per compact

disk when blue lasers are used.

There is great development potential for white leds in the field of lighting. Nichia Corporation is the first company who used blue-LED chips with yellow phosphors to make white LEDs. The common light sources today are light bulbs and fluorescent tubes; however, they are high-energy consuming and short life time. The nitride-based LEDs are more reliable and efficient than conventional light sources, therefore much effort must be paid on generating white light with nitride-based LEDs.

1.2 III-Nitride Materials Growth Issues

1.2.1 Crystal Structure of III-Nitride Semiconductors

Like most other semiconductors, the atoms in the nitrides are tetrahedrally coordinated. The s and p orbitals in the outer electron shells combine to produce hybrid sp^3 orbitals where the probability of finding an electron in a p-state is 3 times as much as finding it in an s-state. As a result, each atomic site has four nearest neighbors occupying the vertices of a regular tetrahedron, in a manner similar to the diamond-cubic structure.

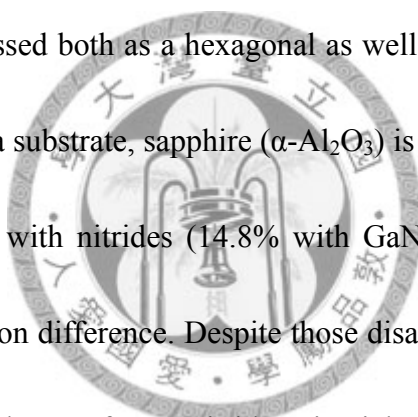
There are three common crystal structures in nitride semiconductors: the wurtzite (Wz), the zinblende (ZB), and the rocksalt structures. At room-temperature, the wurtzite structure is the most stable. The space group for the wurtzite structure is $P6_3mc (C_{6v}^4)$

as shown in Fig. 1.2.1(a). The wurtzite structure has a hexagonal unit cell consisting of two interpenetrating Hexagonal Close Packed (HCP) sublattices, and two lattice constants, c and a . The parameters of the hexagonal wurtzite structure GaN are $a = 3.189\text{\AA}$ (Table.1.1). For the Wz structure, the stacking sequence of the (0001) plane is ABABAB in the $\langle 0001 \rangle$ direction as shown in Fig. 1.2.1(b). The space group for the zincblende structure is $F\bar{4}3m(T_d^2)$ as shown in Fig. 1.2.2(a). The zincblende structure has a cubic unit cell, containing four group-III elements and four nitrogen elements. The lattice parameters of the zincblende structure GaN are $a = 4.52\text{\AA}$ (Table.1.1). For the ZB structure, the stacking sequence of the (111) plane is ABCABC in the $\langle 111 \rangle$ direction as shown in Fig. 1.2.2(b) [2]. These lattices are polar in nature, since the anions and the cations occupy planes that are displaced from one another along the $\langle 0001 \rangle$ and the $\langle 111 \rangle$ directions for the hexagonal and cubic structures, respectively.

1.2.2 Substrate for Nitride Epitaxy

One of the major difficulties, which has hindered GaN research, is the lack of a suitable substrate material that is lattice matched and thermally compatible with GaN. There are several substrates such as ZnO, SiC, and sapphire for growing thin films of GaN. ZnO has the wurtzite structure, and is mismatched by only 1.8% to GaN. Unfortunately, ZnO crystals are not easy to make, and ZnO is not as thermally stable as

might be desired. Nevertheless, ZnO is important for MBE growth [3]. Another choice of substrate is SiC because it also has a smaller lattice mismatch (3.3%) with GaN. However, there are problems in using SiC. For example, the defect densities of the grown samples both in bulk and surface structure are still quite high [4]. Also, the p-type contacts and p-type dopant activation are still quite poor [5]. The high price is another drawback of using SiC as substrate. Nowadays, sapphire is the most commonly used substrate for epitaxy growth of nitrides. Sapphire (α -Al₂O₃) has a hexagonal structure that can be expressed both as a hexagonal as well as a rhombohedral unit cell as shown in Fig. 1.2.3. As a substrate, sapphire (α -Al₂O₃) is inferior to others because of the large lattice mismatch with nitrides (14.8% with GaN and 25.4% with InN) and significant thermal expansion difference. Despite those disadvantages, sapphire remains the most frequently used substrate for III-nitride epitaxial growth owing to its low cost, its stability at high temperatures, its hexagonal symmetry, and a fairly mature technology for nitride growth on it. The orientation order of GaN films grown on principal sapphire planes: c(basal)-plane, a-plane ($11\bar{2}0$), and r-plane ($1\bar{1}02$) was studied in great detail by Electron Cyclotron Resonance-MBE (ECR-MBE). The quality of GaN films grown directly on sapphire was very poor before the advent of buffer layers. AlN was first used as a buffer layer by Amano and Akasaki. Nakamura et al., grew a GaN buffer layer on a sapphire substrate for the first time. They lowered the

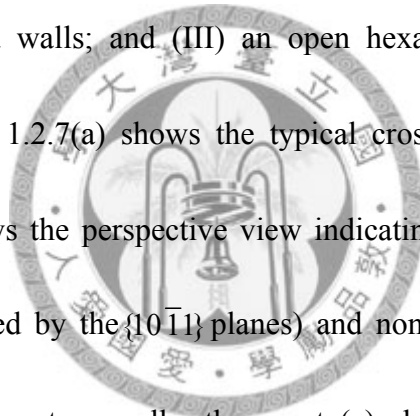


substrate temperature to between 450°C and 600°C to grow the buffer layer. Then, the substrate temperature was elevated to above 1000°C to grow the GaN films [6].

1.2.3 Defects in Nitrides

GaN epitaxial layers are usually grown on sapphire substrates. However, GaN and sapphire have poor matching in the lattice parameter and thermal expansion coefficient, resulting in a high density of threading dislocations (TD) ($10^8 \sim 10^{10} \text{ cm}^{-2}$). There are three kinds of threading dislocations, edge, screw, and mixed types. A dislocation is a line defect that is defined by its Burgers vector b and line direction. The Burgers vector b describes the lattice displacement for the dislocation within the crystal. The dislocation is an edge type if the b and dislocation are perpendicular, as shown in Fig. 1.2.4, whereas it is a screw type if these vectors are parallel, as shown in Fig. 1.2.5. A mixed dislocation has both an edge and a screw component (see Fig 1.2.6) [7]. A threading dislocation usually terminates with a V-shaped defect on the sample surface. It is well-known that such dislocations act as nonradiative centers in III–V and II–VI semiconductors [8], [9]. Hino et al. discovered threading dislocations having a screw-component burgers vector act as strong nonradiative centers in GaN epitaxial layers, whereas edge dislocations, which are the majority, do not as nonradiative centers [10]. It was believed that the density of V-shape defects would be reduced if GaN

epitaxial layers were grown on GaN free-standing substrates. Generally speaking, increasing the quantum well numbers in MQW structures or increasing the indium contents in the QWs enhances the formation of V-shaped defects. The formation of V-shaped defect is for strain relaxation and the reduced Ga incorporation on the $\{10\bar{1}1\}$ planes, in comparison with the (0001) surface [11]. The V-shape defect consists of three important features: (I) the initiation point at a threading dislocation (TD), which is buried below the bottom of the open apex; (II) buried MQWs on the $\{10\bar{1}1\}$ planes, pyramid walls; and (III) an open hexagonal inverted pyramid as shown in Fig. 1.2.7. Fig. 1.2.7(a) shows the typical cross-section TEM of V-shape defects. Fig. 1.2.7(b) shows the perspective view indicating the six sides of the open hexagonal pyramid (defined by the $\{10\bar{1}1\}$ planes) and non-crystallographic plane that terminates the side-wall quantum wells; then part (c) shows the cross-section view indicating the open V (defined by the $\{10\bar{1}1\}$ planes), the side-wall quantum wells, and the inclined noncrystallographic plane that terminates the side-wall quantum wells [11].



1.3 Review on the Characteristics of InGaN/GaN Structures

1.3.1 Strain Effect

During hetero-structure growth, strain is introduced near the interface because of

the lattice mismatch between sapphire and GaN or between GaN and InN. The epilayer is thicker; the stored strain energy is larger. Beyond a certain thickness, known as the critical thickness (t_c), the strain energy is relaxed by forming misfit dislocations (see Fig. 1.3.1). A misfit dislocation forms at the interface between crystals of the same orientation but different lattice parameter. The atoms at the interface adjust their positions to give regions of good and bad registry [12]. If a_e and a_s are lattice constants of an epilayer (thickness t) and the substrate, respectively, when $a_e > a_s$, and $t < t_c$, the epilayer will experience a compressive stress and hence compressive strain is built (see Fig. 1.3.2). In this situation, a misfit strain is built in the epilayer, which is parallel to the interface. Such a layer is called pseudomorphic strained layer. When $a_e < a_s$, the epilayer is affected by a tensile stress and hence tensile strain is produced. If $t > t_c$, the strain is relaxed and misfit dislocation is produced.

1.3.2 Piezoelectric Fields

Perfectly lattice matched conditions between the well and the barrier materials are implicitly assumed in the theory. Generally speaking, lattice constants in the lateral plane of the well and of the barrier material are different and there exist strains in one or both of the components. The nitrides are piezoelectric materials, so the heterostructures, including GaN/AlN, AlN/GaN, and InGaN/GaN can induce static electric fields via

piezoelectric effect [13]. Takeuchi et al. demonstrated that the piezoelectric field can induce the quantum-confined Stark effect and plays an important role in InGaN/GaN quantum wells. Strain caused by lattice mismatch or different thermal expansion coefficient between the substrate and the epitaxial layers lead to piezoelectric field. The biaxial strains also lead to the piezoelectric field along the z direction in a wurtzite structure. This field caused the electrons and the holes to move toward opposite directions in the well. The overlap of the electron and hole wavefunctions is reduced; thus, the quantum confinement energy levels are different from those in the original confinement potential. This reduction is expected to result in the decrease of the recombination rate. In crystals with a wurtzite structure, the piezoelectric tensor is written as:



$$\begin{pmatrix} 0 & 0 & 0 & 0 & e_{15} & 0 \\ 0 & 0 & 0 & e_{15} & 0 & 0 \\ e_{31} & e_{31} & e_{33} & 0 & 0 & 0 \end{pmatrix}$$

where e_{ij} are the piezoelectric constants. The piezoelectric polarization along the z-axis,

P_{PE} , arises as:

$$P_{PE} = e_{33}\epsilon_z + e_{31}(\epsilon_x + \epsilon_y) \quad (1.1)$$

Charge neutrality condition leads to the electric field along the Z-axis, F_z , as:

$$F_z = -P_{PE} / \epsilon_r / \epsilon_0, \quad (1.2)$$

where ϵ_r is the dielectric constant in vacuum and ϵ_0 is the dielectric constant along the z-axis. Bernardini et al. [14] have predicted that in addition to the high piezoelectric polarization, the spontaneous polarization P_{SP} (polarization at zero strain) cannot be ignored in group-III nitrides. Therefore, the total polarization is the sum of the piezoelectric and spontaneous polarization as:

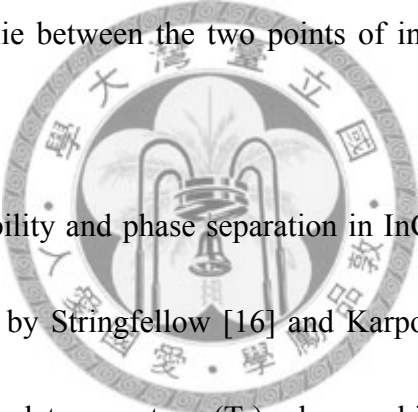
$$P = P_{PE} + P_{SP} \quad (1.3)$$

Several research groups have reported the values of ϵ_{ij} as shown in Table 1.2. As shown in Fig. 1.3.3, the macroscopic polarization in the material, comprising the active region of the multiple quantum wells, gives rise to the net electric field perpendicular to the plane of the well. This field, if strong enough, will induce a spatial separation of electron and hole wavefunctions in the well. This phenomenon is also called quantum confined Stark effect (QCSE). Hence, the wavefunction overlap decreases and the interband recombination rate is reduced.

1.3.3 Spinodal Decomposition and Phase Separation

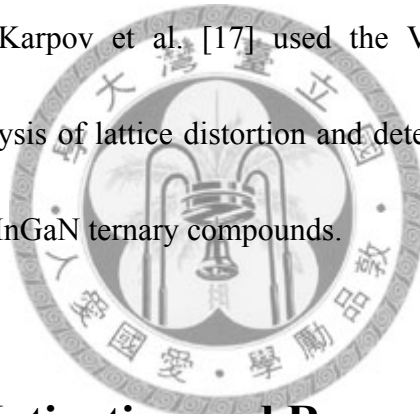
Spinodal decomposition is a transformation process in which there is no barrier to nucleation. Consider a phase diagram with a miscibility gap (see Fig. 1.3.4). If an alloy

with composition X_0 is treated at a high temperature T_1 and then quenched to a lower temperature T_2 , the composition will initially be the same everywhere and its free energy will be G_0 on the G curve. However, the alloy will immediately become unstable because small fluctuations in composition that produce A-rich and B-rich regions will cause the total free energy to decrease. Therefore, “up-hill” diffusion takes place until the equilibrium compositions X_1 and X_2 are reached. The above process can occur for any alloy composition where the free energy curve is concave in shape, i.e. $d^2G/dx^2 < 0$. Therefore, the alloy must lie between the two points of inflection on the free energy curve.



Solid phase immiscibility and phase separation in InGaN related to elastic strain [15] have been deliberated by Stringfellow [16] and Karpov et al. [17]. According to Stringfellow [16], the critical temperature (T_c), above which the InN-GaN system is completely miscible is found to be near 1250 K. At a typical growth temperature of 800 °C, the solubility of InN in GaN is calculated to be less than 6%. Stringfellow and Chen stressed that spinodal decomposition can occur in several situations including clustering, phase separation, and ordering. The reaction that occurs is determined by the growth kinetics. Both thermodynamic and kinetic factors play roles in determining the degree of order for specific epitaxial growth parameters and on which planes the compositional modulations occur. The thermodynamic driving force leads to a reduction of the

microscopic strain energy due to stretching and bending of the bonds. Certain ordered alloys have lower energies than a disordered alloy. The formation of two separate, incoherent phases will result in even lower energy configuration. However, this is prevented in practice by the coherency strain energy inherent in the initial stages of phase separation. The kinetic effect plays an important role in growth parameters such as the growth temperature, growth rate and substrate orientation. Behbehani et al. [18] reported on the existence of simultaneous phase separation and ordering of $\text{In}_x\text{Ga}_{1-x}\text{N}$ samples with $x > 0.25$. Karpov et al. [17] used the Valence Force Field (VFF) approximation for the analysis of lattice distortion and determination of the interaction energy of GaN and InN in InGaN ternary compounds.



1.4 Research Motivation and Research Problems

The (Al, Ga, In)N material system has been extensively investigated due to their potential applications in light-emitting diodes (LEDs), laser diodes, and photodetectors.

[19] In recent years, InGaN alloys emerge as a new solar cell material system due to their characteristics of high absorption, broad spectral coverage, and radiation hardness.

InGaN is particularly useful for converting sunlight in the visible range into electrical power. For this purpose, the growth of high-quality InGaN thin films with indium content higher than 20 % becomes important [20]. However, because of the large lattice

mismatch (11 %) between GaN and InN, phase separation occurs when the InGaN thickness is larger than its critical thickness, which is smaller than 60 nm for indium content higher than 20% [21]. Within the critical thickness, under the heterostructure-induced strain, indium incorporation is relatively lower leading to lower-indium growth. Beyond the critical thickness, relaxed strain leads to more significant indium incorporation. Although an InGaN thin film has been widely grown, its indium composition distribution and hence band gap distribution are not well understood yet. In particular, the possible indium droplet formed in phase separation when a p-type GaN cap layer of high-temperature growth is added to form a p-i-n structure has not been well studied.

In this research, we present our measurement results of cross sectional transmission electron microscopy (TEM), scanning electron microscopy (SEM), energy dispersive X-ray spectrum (EDX), X-ray diffraction (XRD), and photoluminescence (PL) on InGaN/GaN single-heterostructures (SH) and double-heterostructures (DH) with various InGaN thicknesses.

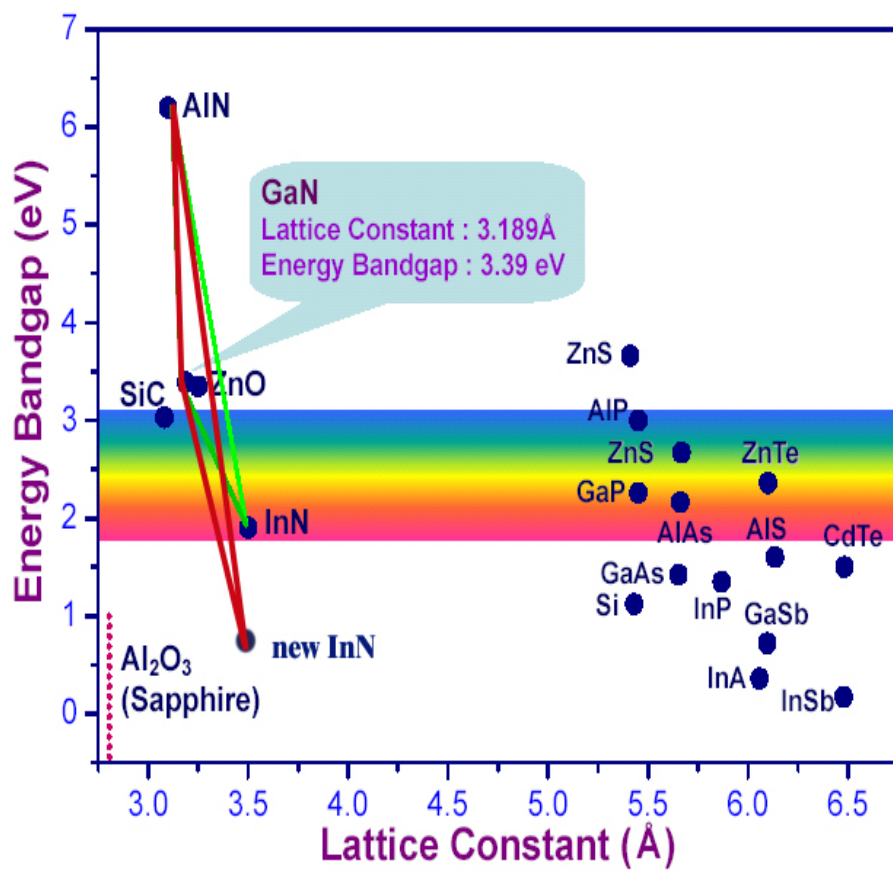
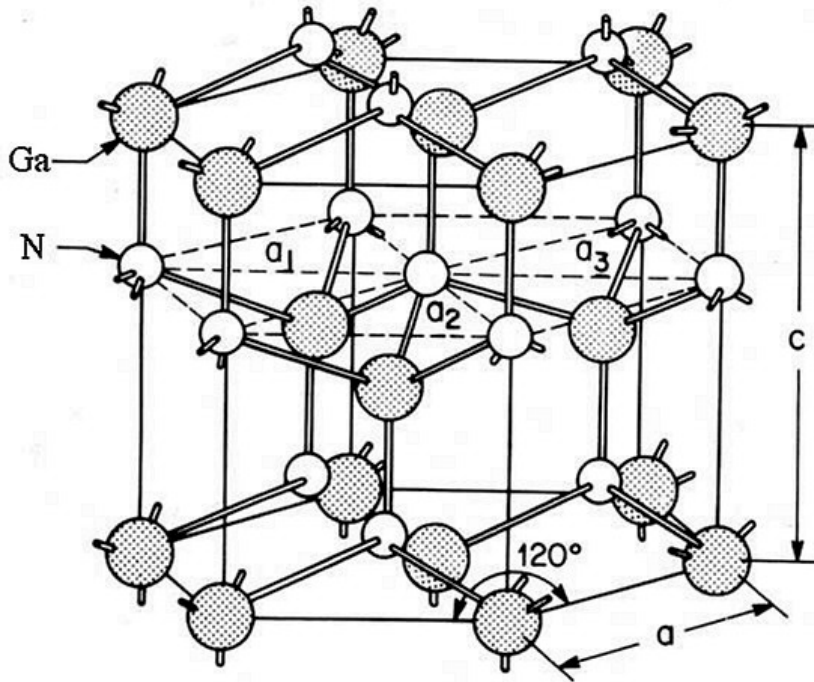


Fig. 1.1.1 Energy band gap versus lattice constant in II-VI and III-V compound semiconductors.



<http://kottan-labs.bgsu.edu/teaching/workshop2001/chapter5.htm>

Fig. 1.2.1(a) Hexagonal Wurtzite structure of GaN.

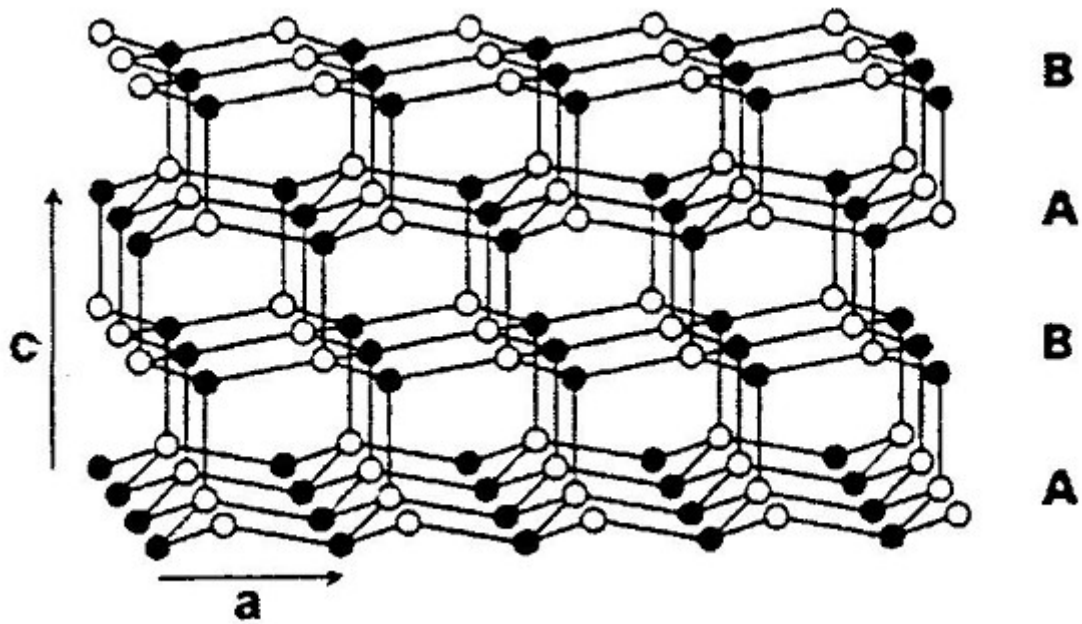
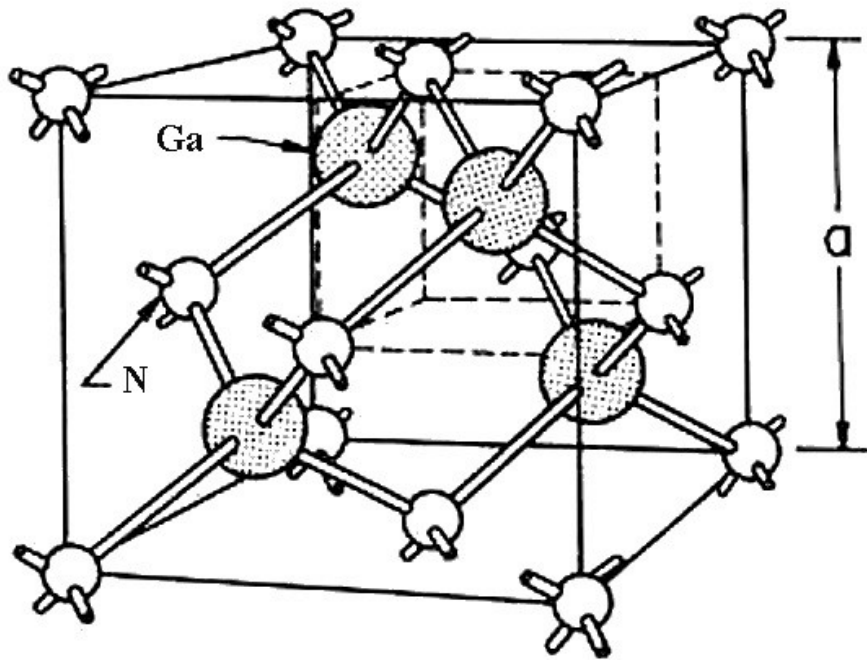


Fig. 1.2.1(b) Crystalline layer sequences of hexagonal Wurtzite structure.



<http://kottan-labs.bgsu.edu/teaching/workshop2001/chapter5.htm>

Fig. 1.2.2(a) Cubic Zincblende structure of GaN.

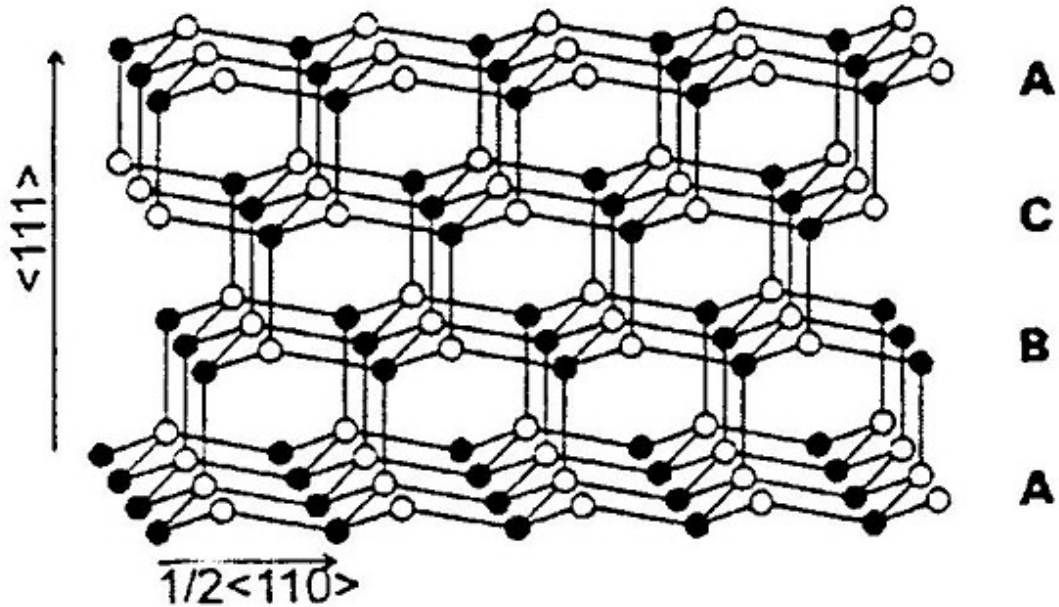


Fig. 1.2.2(b) Crystalline layer sequences of cubic Zincblende structure.

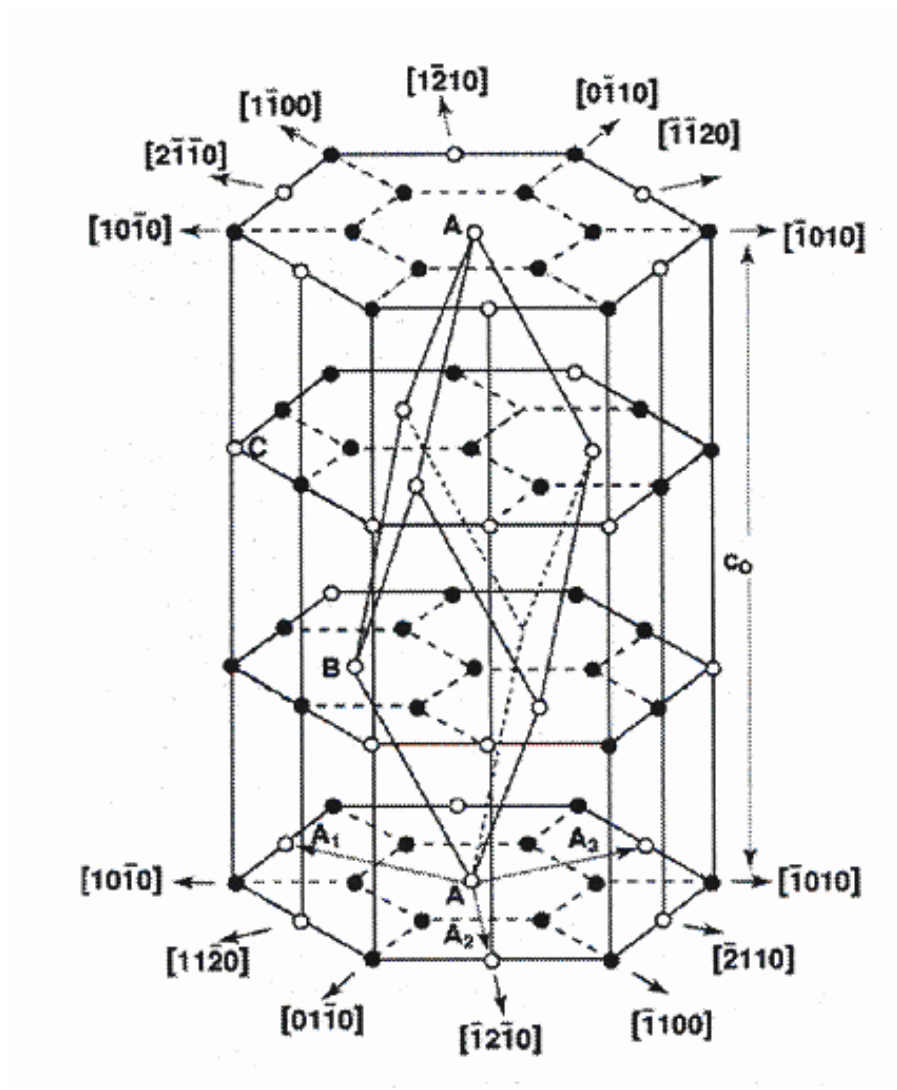


Fig. 1.2.3 Crystal lattice of sapphire.

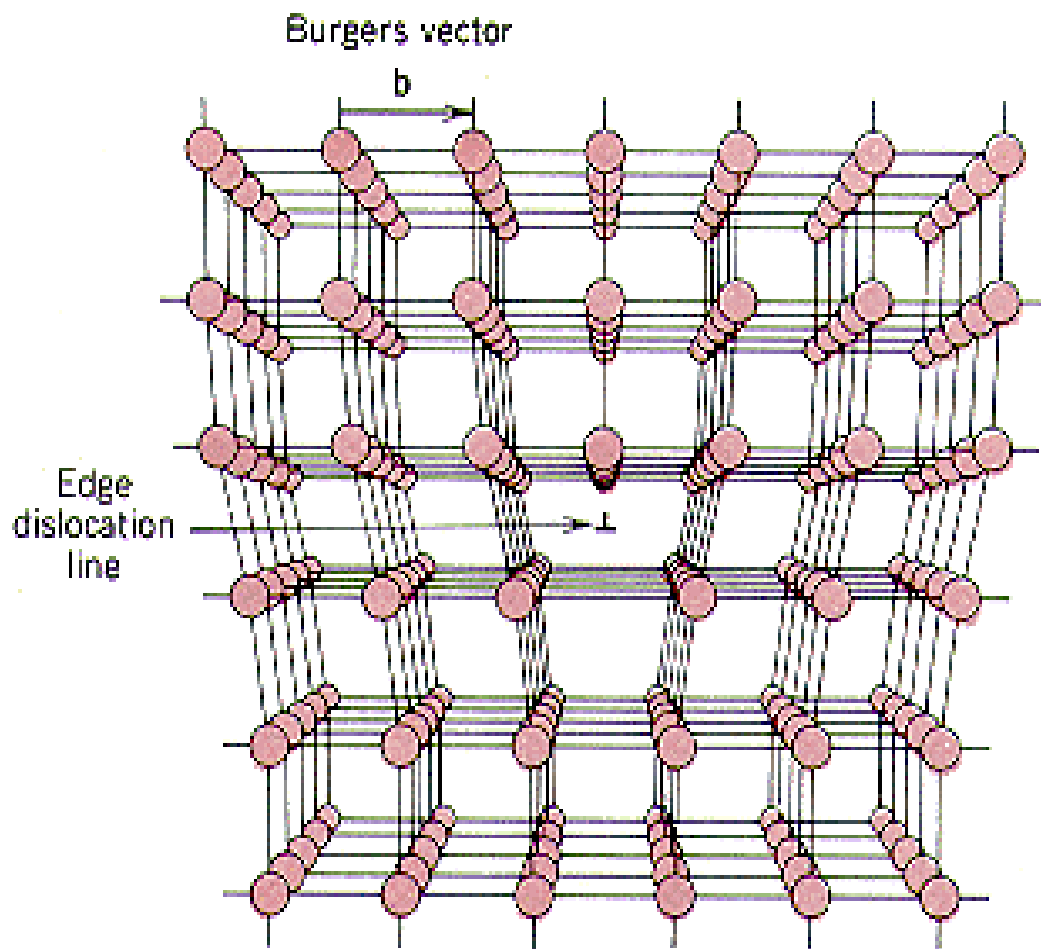


Fig. 1.2.4 Edge Dislocation.

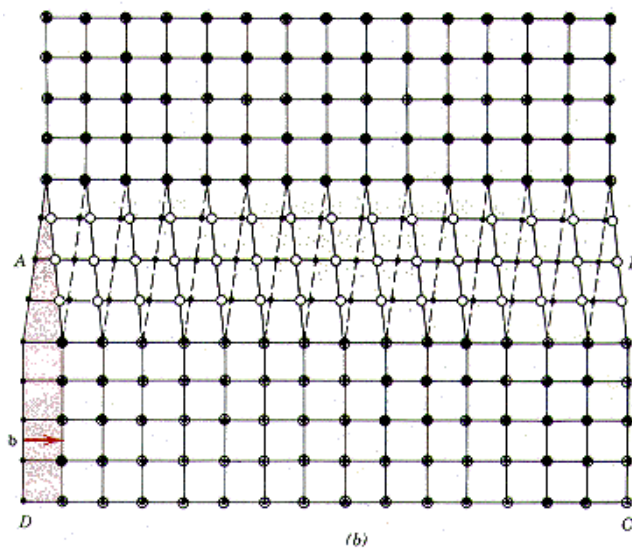
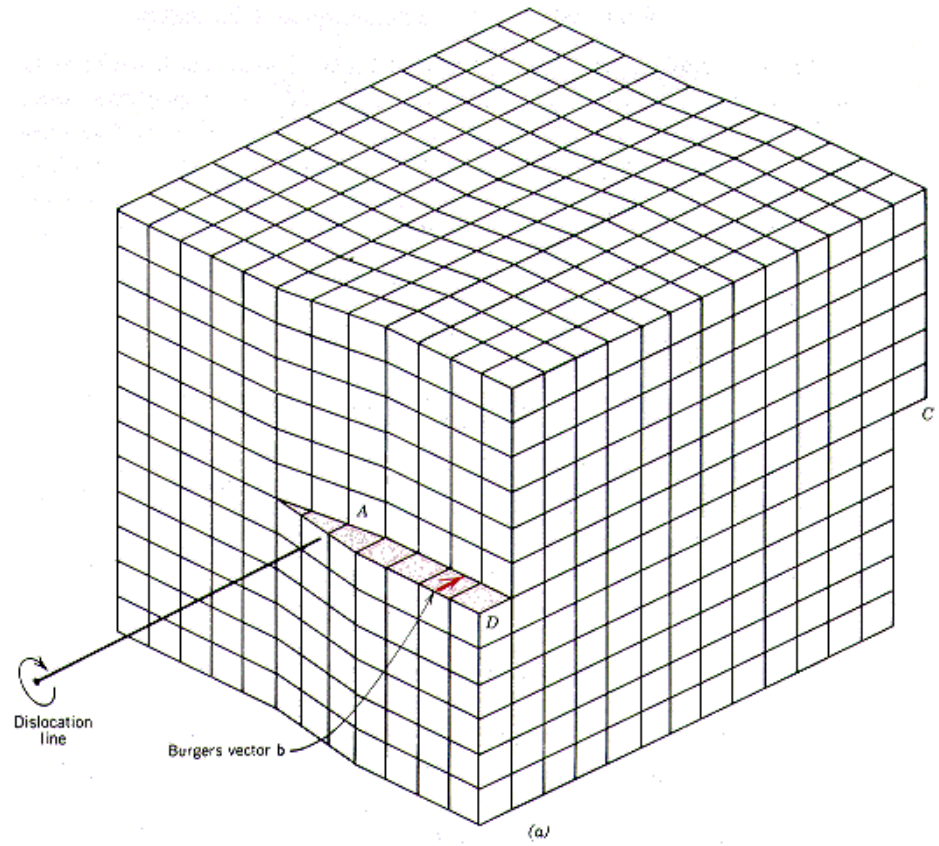


Fig. 1.2.5 Screw Dislocation.

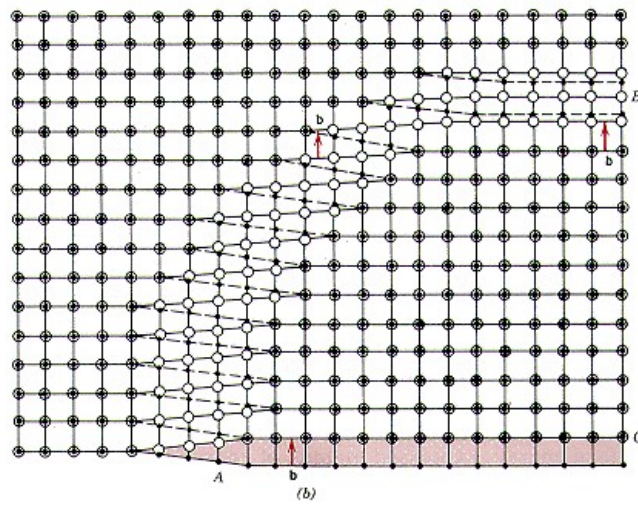
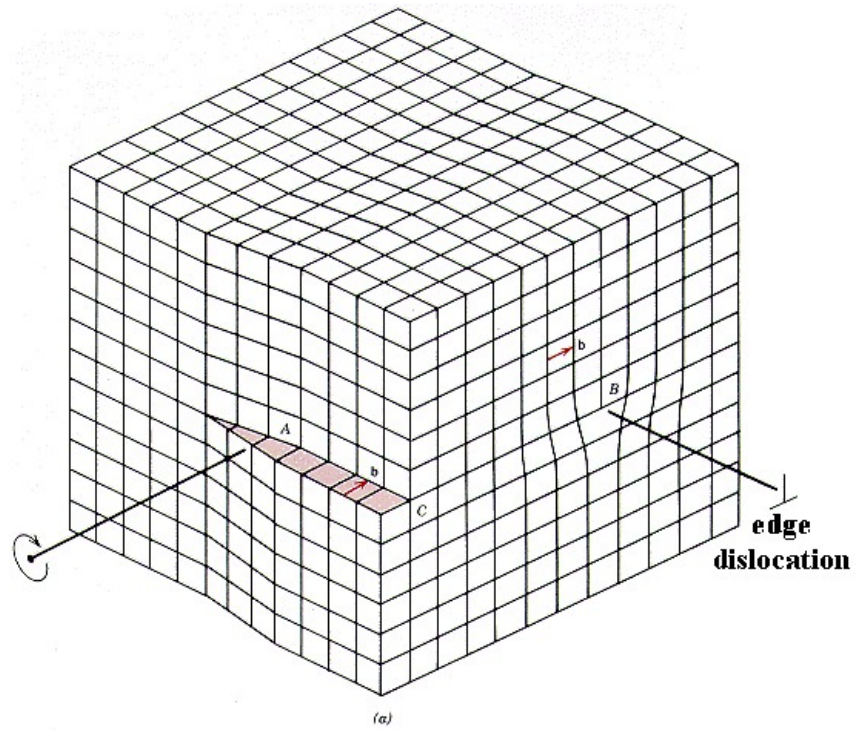


Fig. 1.2.6 Mixed Dislocation.

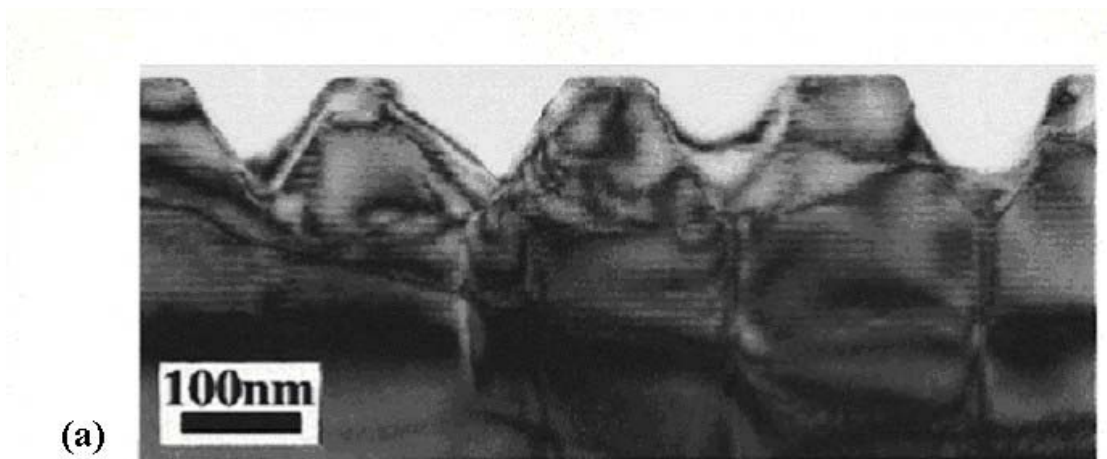


Fig.1.2.7(a) Typical cross-section TEM of V-shaped defects.

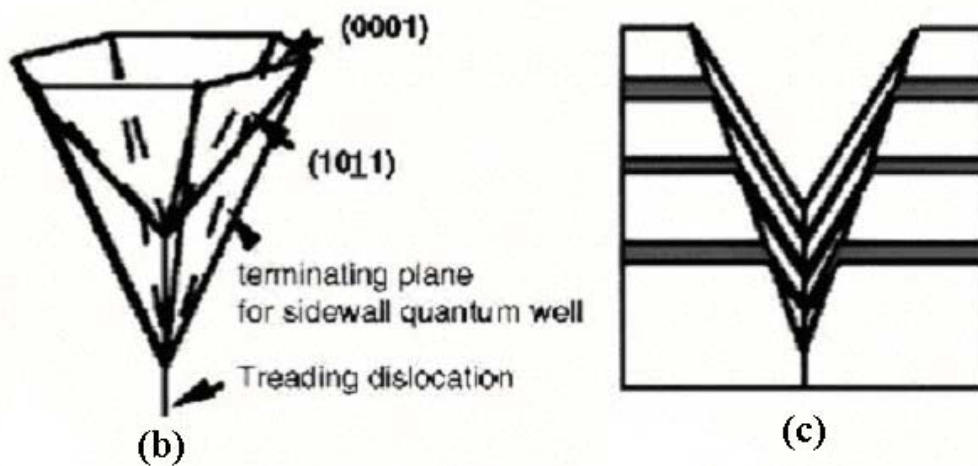
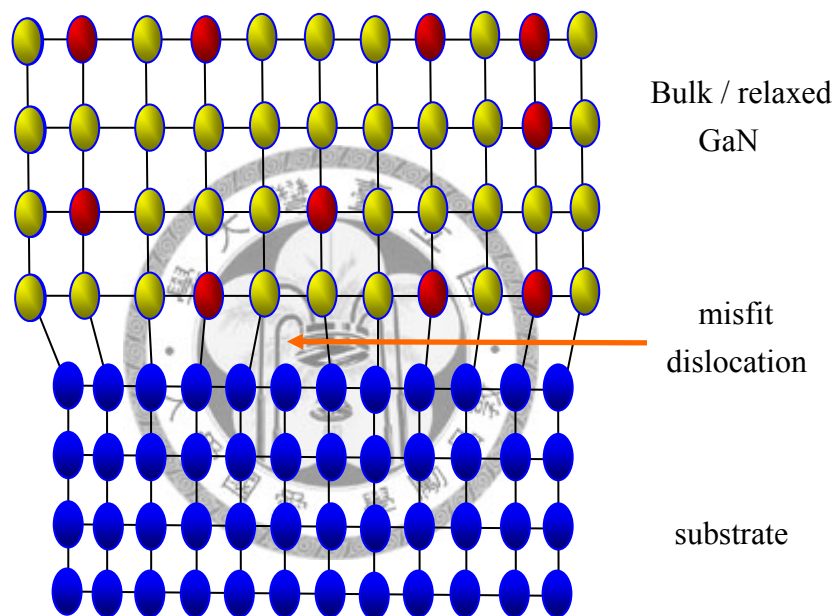


Fig. 1.2.7(b) Perspective view and (c) cross-section view of V-shaped defects.



<http://www.sp.phy.cam.ac.uk/~dp350/Misfit.html>

Fig. 1.3.1 Schematic illustration of a misfit dislocation formed during epitaxial growth.

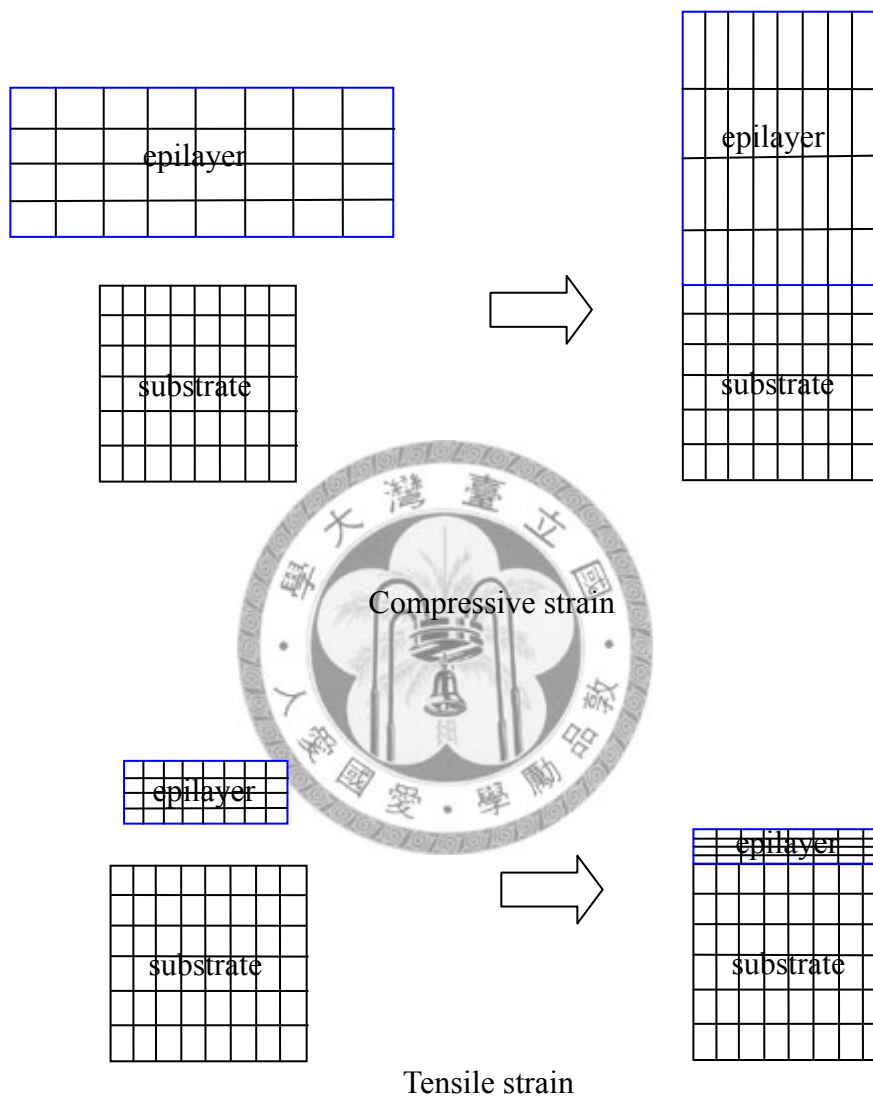
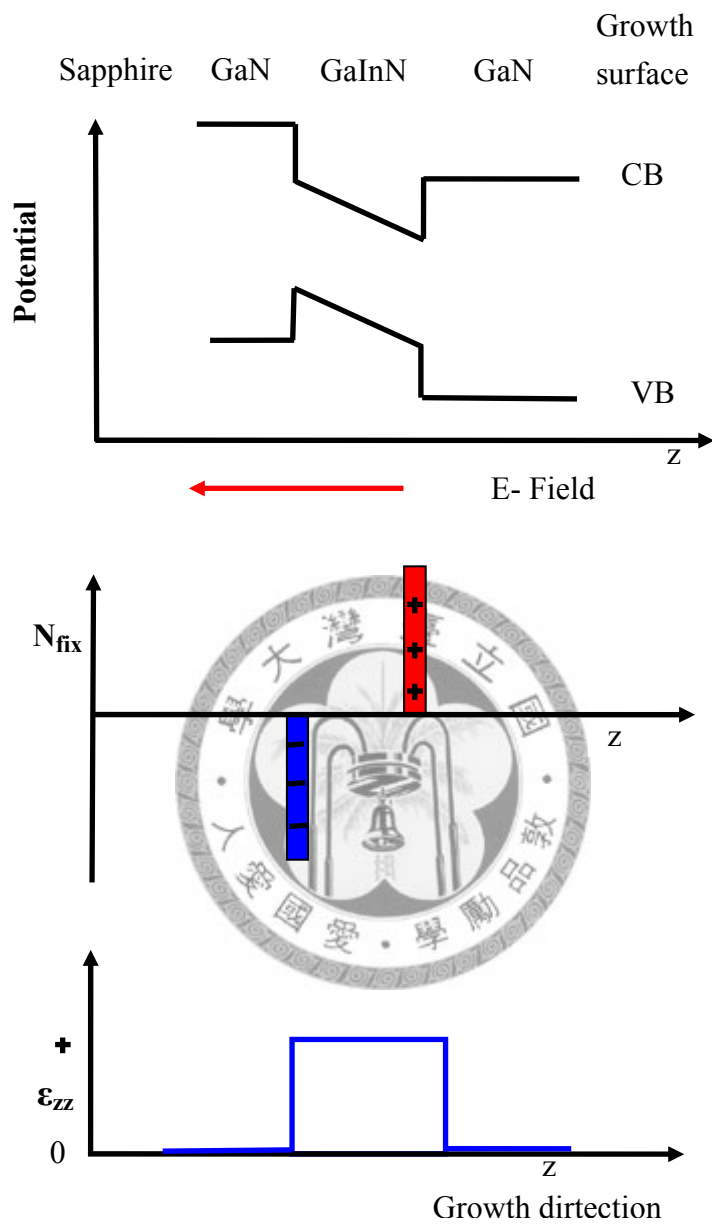


Fig.1.3.2 Compressive and tensile strains



<http://nsr.mij.mrs.org/3/31/tnfigures.html>

Fig. 1.3.3 Schematic of the strain induced along the growth direction, the resulting piezoelectric charges, and the bandstructure of a GaN-GaInN-GaN heterostructure.

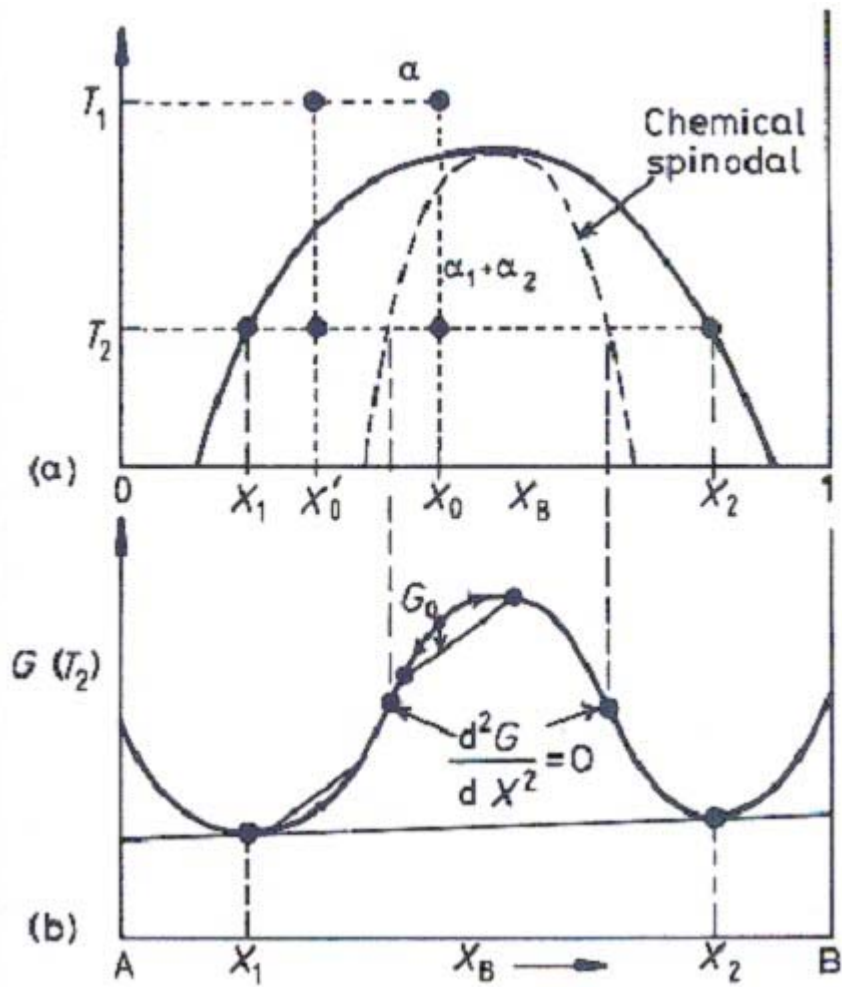


Fig. 1.3.4 A phase diagram with a miscibility gap.

Table 1.1 The basic parameters of InN, GaN, and AlN wurtzite structures.

Parameter	Units	GaN	AlN	InN
Lattice constant, c	Å	5.186	4.982	5.693
Lattice constant, a	Å	3.189	3.112	3.533
Bandgap energy, E_g	eV	3.39	6.2	0.76
Effective electron mass, m_e	m_0	0.19(∥)	0.33(∥)	0.11(∥)
		0.17(⊥)	0.25(⊥)	0.10(⊥)
Effective heavy hole mass, m_{hh}	m_0	1.76(∥)	3.53(∥)	1.56(∥)
		1.61(⊥)	10.42(⊥)	1.68(⊥)
Effective light hole mass, m_{lh}	m_0	1.76(∥)	3.53(∥)	1.56(∥)
		0.14(⊥)	0.24(⊥)	0.11(⊥)
Piezoelectric constant, e_{31}	C/m ²	-0.33	-0.48	-0.57
Piezoelectric constant, e_{33}	C/m ²	0.65	1.55	0.97
Spontaneous polarization, $P_{ }$	C/m ²	-0.029	-0.081	-0.032
Radiative recombination coefficient	cm ³ /s	4.7×10^{-11}	1.8×10^{-11}	5.2×10^{-11}
Refractive index at 555nm		2.4	2.1	2.8
Absorption coefficient at the photon Energy $h\nu \sim E_g$	10^5cm^{-1}	1	3	0.4

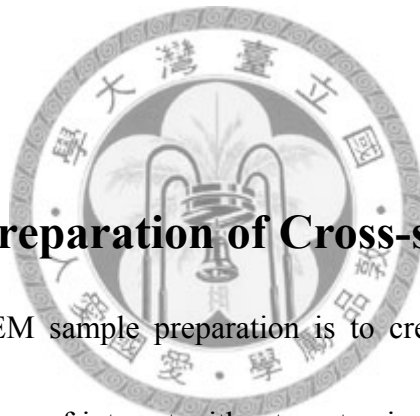
Table 1.2 Piezoelectric constants and spontaneous polarization
for III-nitrides.

Reference		ZB		WZ		
		e_{14}	p_z^{eq}	e_{33}	e_{31}	e_{15}
BN						
Shimada et al. (1998)	Calc	-0.64	-	-0.85	0.27	-
AlN						
Tsubouchi and Mikhshiba (1985)	Exp.	-	-	1.55	-0.58	-
Davydov and Tikhonov (1996)	Clac	0.67	-	-	-	-
Bernardini et al. (1997)	Clac	-	-0.081	1.46	-0.60	-
Shimada et al. (1998)	Clac	0.59	-	1.29	-0.38	-
GaN						
O'clock and Duffy (1973)	Exp.	0.6	-	-	-	-
Bykhovski et al. (1996)	Exp.	0.375	-	0.43	-0.22	-0.22
Davydov and Tikhonov(1996)	Clac	0.68	-	-	-	-
Bernardini et al. (1997)	Clac	-	-0.029	0.73	-0.49	-
Shimada et al. (1998)	Clac	0.50	-	0.63	-0.32	-
InN						
Bernardini et al. (1997)	Clac	-	-0.032	0.97	-0.57	-

Chapter 2

Analysis Method

This chapter will describe the methods used to analyze our samples including materials and optical analysis methods. High resolution transmission electron microscopy (HRTEM), strain state analysis (SSA), energy dispersive X-ray spectrum (EDX), x-ray diffraction (XRD), and scanning electron microscopy (SEM) are used to analyze material properties. Photoluminescence (PL) is used to analyze the optical properties.



2.1 Specimen Preparation of Cross-section TEM

The objective of TEM sample preparation is to create an electron transparent region containing the features of interest without contamination and artifacts. There are many different methods to make TEM specimen. Among them, only three types of techniques are commonly used, including the dimpling and ion milling technique, the focused ion beam technique, and the wedge technique. The dimpling technique works well for the blanket films, large features, and repeated patterns. However, it provides smaller thin areas and is difficult to target to a special feature. The focused ion beam technique offers a reliable method to make high precision cross-sections of the specific area. However, this method provides a very limited area of view and is easy to introduce

damages. The wedge technique provides highest flexibility over other techniques. It can be used to make plan view, regular cross-section specimen and precision cross-section specimens. We can thin the sample down to less than 1 μm by pure mechanical polishing. More importantly, the electron transparent area can be as large as millimeters. We will explain the details about this technique since all TEM specimens used for this research are made by the wedge technique. Several steps are as follows:

1. The first step is to have the wafer sectioned into rectangular slabs that are at least 3 mm in width and about 10 mm in length, as shown in Fig. 2.1.1(a). To do this, a diamond wafering saw or a diamond pen can be used. The former method yields equal-sized pieces, which are easier to handle. However, it is more time consuming.
2. Next, we need to thoroughly clean and degrease the slabs. This is best done by ultrasonically scrubbing them in acetone and then in Freon. A cotton swab may be used to gently remove any persistent surface contaminants. The required number of sample slabs depends on their thickness. Generally speaking, we need two pieces of sample slabs and two pieces of silicon.
3. We choose G1-epoxy to glue the slabs as shown in Fig. 2.1.1(b). There are three main advantages of this glue that make it particularly suitable for this application: it is very strong; it is very thin when properly applied ($\sim 2000 \text{ \AA}$), and it can be ion milled at about the same rate as silicon. Furthermore, it is impervious to the attack

of any solvent once it is set. The main drawback is that it needs to be thermoset under pressure. To accomplish this step, a small vise is used that can be heated on a hotplate (see Fig. 2.1.2). The two pieces of sample slabs having the thin films or interfaces of interest must be in the center and the polished faces of these two pieces thus face each other. Then, the sample is mounted onto the polisher, as shown in Fig. 2.1.1(c).

4. After specimen mounting, the polisher is placed on lapping films and the specimens are wet polished using progressively finer grit diamond lapping films (30, 9, 6, 3, 1, 0.5 and 0.1 μm , respectively) for coarse polishing. The thickness of the specimen are less than 1.5 mm after the first side polishing. The specimen will easily fall off from the polisher during the second side polishing. The wedge angle was set at about 0.4° . It is very important to remove any contamination or particles from the mounting surface.
5. The polished surface is attached to the polisher using a small amount of super glue. Sufficient super glue is used to surround the edges of the specimen to provide certain mechanical stability during processing and to protect the specimen from the risk of film delamination.
6. After curing the super glue, the specimens are wet polished to the desired thickness using the same diamond lapping films in the same order as described in the first side

polishing. The specimen is checked frequently to ensure that it is polished sufficiently thin during the last four polishing steps (3, 1, 0.5 and 0.1 μm). It is difficult to determine whether the specimen is sufficiently polished since the GaN/sapphire specimen is transparent. Consequently, the specimen is checked by observing the color of silicon in transmission using an optical microscope.

7. After polishing, the specimen is removed from the polisher by soaking in acetone and mounted onto a 2×1 mm slotted TEM grid using epoxy as shown in Fig. 2.1.1(d).

8. Then, we can have the specimen be milled by argon-ion gas for several minutes (see Fig. 2.1.1(e)).



2.2 Material Analysis

2.2.1 High-resolution Transmission Electron Microscopy (HRTEM)

Transmission electron microscopy (TEM) is probably the most important and widely used characterization tool to study the nano-structural characteristics of materials. The basic reason for utilizing the electron microscopy is its superior resolution, resulting from very small wavelengths as compared to other forms of radiation (light, X-rays, neutrons). The resolution is given by the Rayleigh formula, which is derived by

considering the maximum angle of electron scattering, α , which can pass through the objective lens. This formula is

$$R=0.61\lambda/\alpha \quad (2.1)$$

Where R is the size of the resolved object, λ is the wavelength, and α is identical to the effective aperture of the objective lens. Equation (2.1) is the classic Rayleigh criterion for resolution in light optics.

A cutaway diagram of the TEM is shown in Fig. 2.2.1. In a conventional TEM, a thin specimen is irradiated with an electron beam of uniform current density; the electron energy is in the range 60-150 keV (usually around 100 keV) or 200 keV-300 MeV in the case of intermediate or high-voltage electron microscopy. Electrons are emitted in the electron gun by thermionic emission from tungsten hairpin cathodes or LaB₆ rods or by field emission from pointed tungsten filaments. The latter is used when high gun brightness is needed. A two-stage condenser-lens system permits variation of the illumination aperture and the area of the specimen illuminated. The electron intensity distribution behind the specimen is imaged with a three- or four-stage lens system, onto a fluorescent screen. The image can be recorded by direct exposure of a photographic emulsion inside the vacuum or digitally by CCD or TV cameras.

Figure 2.2.2 illustrates the principal results of electron scattering by a sample and, as a result, the principal sources of information that can be obtained. The operating

modes are as follows: transmission electron microscopy (TEM), scanning electron microscopy (SEM), scanning transmission electron microscopy (STEM), and microanalysis (by X-ray and/or energy loss analysis or Auger analysis of surfaces).

The imaging system of a TEM consists of at least three lenses (Fig. 2.2.3): the objective lens, the intermediate lens and the projector lens. The intermediate lens can magnify the first intermediate image, which is formed just in front of this lens (Fig. 2.2.3(a)). An image is made with only those electrons that have been diffracted by a specific angle by positioning an objective aperture at a specific location in the back focal plane. This defines two imaging modes.

- When the objective aperture is positioned to pass only the transmitted (undiffracted) electrons, a bright-field (BF) image is formed.
- When the objective aperture is positioned to pass only some diffracted electrons, a dark-field (DF) image is formed. (The particular diffraction should be specified.)

The intermediate lens can also magnify the first diffraction pattern, which is formed in the focal plane of the objective lens (Fig. 2.2.3(b)). In many microscopes, an additional diffraction lens is inserted between the objective and intermediate lenses to image the diffraction pattern and to enable the magnification to be varied in the range 10^2 to 10^6 .

The transmission electron microscopes used in this study are JEOL 100CX II and Philips Tecnai F30 field-emission electron microscope. The JEOL 100CX II is equipped

with a tungsten electron source and operates at 100kV accelerating voltage. The magnification range is from 500x to 300,000x and the lattice resolution is 0.2 nm (point resolution 0.45nm). The Philips Tecnai F30 field-emission electron microscope is equipped with a field emission gun (FEG) and operates at 300kV accelerating voltage. The magnification range is from 60x to 1,000,000x and the lattice resolution is 0.10nm (point resolution 0.20nm).

Bright-field and dark-field techniques cannot be used to form high resolution TEM images of columns of atoms in Fig. 2.2.4. The diffracted wave, in this case an electron wavefunction, is the Fourier transform of the scattering factor distribution in the material, $\rho(r)$. The shape of $\rho(r)$ tracks the atom distribution in the material. High resolution images are best understood in terms of Fourier transforms. We use the notation, $F(\rho(r))$, to represent the Fourier transform of the distribution of atoms in the specimen, $\rho(r)$:

$$F(\rho(r)) = \frac{1}{\sqrt{2\pi}} \int_{-\infty}^{+\infty} \rho(r) e^{-i\Delta k \cdot r} d^3 r \quad (2.2)$$

The Fourier transform is a function of Δk , a diffraction vector. With dimensions of inverse length, the vector Δk can account for periodicities in the specimen. Recall that a smooth function, $\rho(r)$, which has a large extent in r , has a Fourier transform that is nonzero only for small values of Δk . On the other hand, a function $\rho(r)$ that has short periodicities has a Fourier transform containing some large Δk vectors. Fig. 2.2.5 shows

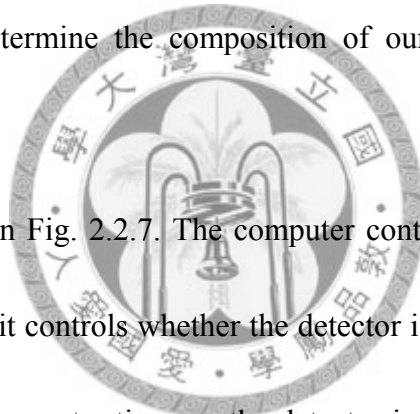
how Fourier transforms of the diffracted electron waves correspond to the specimen, the back focal plane of the objective lens, and the image plane. An objective aperture in the back focal plane of the objective lens will truncate the Fourier transform of the specimen. An image formed with a small range of k-vectors can include only long-range spatial features. For an objective aperture that selects a range, δk , the smallest spatial features in the image are approximately Δx , where:

$$\Delta x = 2\pi/\delta k \quad (2.3)$$

To resolve atomic periodicities, we need an aperture that incorporates a range, $\delta k \doteq 2\pi/d$, where d is the atomic separation. This, however, is the typical separation of the first diffraction spot from the transmitted beam. A much smaller aperture is used in bright-field and dark-field imaging to collect electrons that have all beam diffracted by the same angle. The consequent truncation in k-space means that the conventional bright-field and dark-field modes of TEM imaging cannot produce high resolution images. In fact, making a high resolution image requires that we use an objective aperture large enough to include both the transmitted beam and at least one diffracted beam. The transmitted (“forward-scattered”) beam is required to provide a reference phase of the electron wavefront. High resolution images are in fact interference patterns formed from the phase relationships of diffracted beams.

2.2.2 Energy Dispersive X-ray Spectrum (EDX)

Sample composition was examined by EDX. Fig. 2.2.6 shows the interaction of a beam electron with an inner-shell resulting in an excited state with a vacancy in the electron shell. An electron transition will come up from an outer shell to fill this vacancy. The transition involves a change in energy, and the energy releases from the atom. While the energy of the emitted x-ray is related to the difference in energy between the levels of the atom, it can be ascribed as a characteristic x-ray. As in the TEM measurements, we can determine the composition of our samples according to the detected x-ray.



An EDX system is in Fig. 2.2.7. The computer controls three parts to carry out any data processing. First, it controls whether the detector is on or off. Ideally, we want to process one incoming x-ray at a time, so the detector is switched off while an x-ray signal is detected. Second, the computer governs the processing electronics, setting the time required to analyze the x-ray signal and assigning the signal to the correct channel in the display screen. Third, the computer software manages both the calibration of the spectrum readout on the screen and all the alpha-numeric, which tells us the conditions under which the spectrum was acquired.

2.2.3 Strain-state Analysis (SSA)

Composition fluctuations in InGaN were recognized a number of years ago to significantly determine the properties of devices fabricated on the basis of InGaN/GaN heterostructures. It is therefore of considerable interest to study quantitatively the In distribution of InGaN and the spatial dimension of compositional fluctuations. For this reason, a strain-state analysis (SSA) technique has been developed, which was used to evaluate the composition of InGaN.

Strain-state analysis (SSA) is a technique based on HRTEM lattice fringe images. Lattice fringe images are taken under two-beam conditions by only exciting the (0000) and (0002) beams, which is possible with a minimum number of other excited beams by tilting the sample about 5° out of the [1-100]-zone axis along the [11-20] direction. The images are taken with an objective aperture containing the transmitted and the (0002) beams. Instead of using a zone-axis HRTEM image, where typically at least nine beams are used to form an image along the [11-20]- or [1-100]-zone axes, two-beam conditions simplify considerably the image formation process. The interference of only two beams leads to a fringe image. The apparent loss of resolution along the (0002) fringes compared to a conventional zone-axis image does not present a problem because only the distances between the (0002) fringes need to be measured. This can be achieved by carrying out closely spaced line scans.

An example for a lattice fringe image is displayed in Fig. 2.2.8(a) where a thin InGaN QW is embedded in GaN. The distances between the (0002) planes d_{0002} are measured by detecting the intensity maximum positions of the bright fringes by line scans along the [0001] direction (white lines in Fig. 2.2.8(b)).

The composition evaluation is based on a rather simple principle by assuming that the lattice parameter of a ternary compound, e.g. InGaN with a lattice parameter d_{InGaN} , is linearly dependent on the In concentration x_{In} .

$$\text{Vegard's law: } d_{\text{InGaN}} = d_{\text{GaN}} + x_{\text{In}}(d_{\text{InN}} - d_{\text{GaN}}) \quad (2.4)$$

InGaN is a system that is well suited for composition analysis on the basis of Eq. (2.4) because the lattice parameter mismatch between InN and GaN is 10%. The local In concentration is deduced from Vegard's law by Eq. (2.5) taking into account the strain state of the InGaN layer,

$$x_m = \frac{1}{f_{0,c}} \frac{1}{1+K} (d_n - 1) \quad (2.5)$$

$$f_{0,c} = \frac{d_m - d_{\text{GaN}}}{d_{\text{GaN}}} = 0.098$$

$$d_n = \frac{d_j}{d_r}$$

The values for d_{GaN} and d_{InN} are $d_{\text{GaN}} = 0.5186\text{nm}$ and $d_{\text{InN}}=0.5693\text{nm}$. A reference (0002) distance d_r can be measured in an area of known lattice parameter, e.g. in the relaxed GaN buffer layer. The unknown (0002)-plane distances d_j in the InGaN are normalized with d_r yielding $d_n=d_j/d_r$. The factor K results from the tetragonal distortion

of the InGaN lattice in strained layers. Two cases for the tetragonal distortion have to be distinguished for TEM cross-section samples whose thickness for HRTEM imaging can be as low as a few nanometers. A complete tetragonal distortion occurs for thick samples (“thick foil approximation”). In contrast, the tetragonal distortion can be completely relaxed along the electron beam direction for very thin samples (“thin foil approximation”). The factors K , which depend on the elastic constants c_{ij} and on the surface normal of the cross-section sample (in this case close to the [1-100] direction) are given by Eqs. (2.6) and (2.7),

$$K^{thick} = 2 \frac{c_{13}}{c_{33}} \quad (2.6)$$

$$K^{thin} = \frac{c_{13}}{c_{33}} \left(1 - \frac{c_{12}c_{33} - c_{13}^2}{c_{11}c_{33} - c_{13}^2} \right) \quad (2.7)$$

The values $K^{thick}=0.55\pm0.0667$ and $K^{thin}=0.19\pm0.035$ are almost independent of the In concentration [1]. Figure 2.2.9 shows the influence of the relaxation state on the normalized lattice parameters d_n , i.e. the ratio between the InGaN and the GaN c-lattice parameters, plotted as a function of the In concentration.

In conclusion, we can use SSA technique to analyze InGaN/GaN (0002) lattice fringe image to get the distances between the (0002) planes d_{0002} . Then, we consider the sample thickness and the elastic relaxation. Finally, we can get In composition of InGaN QW. For a more detailed procedure for SSA, see Ref. [2] [3].

2.2.4 X-Ray Diffraction (XRD)

X-ray diffraction is a nondestructive technique for determining structural defects.

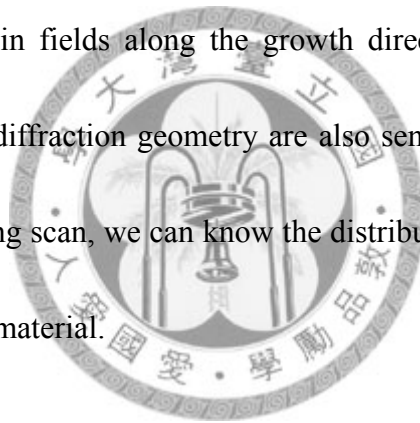
In a diffraction experiment, the incident waves must have wavelengths comparable to the spacing between atoms. Consider a perfect crystal arranged to diffract monochromatic X-rays of wavelength λ from lattice planes spaced d and the X-rays are incident on the sample at an angle θ (see Fig. 2.2.10). The primary beam is absorbed by or transmitted through the sample and only the diffracted beam can be detected by the detector. The diffracted beam emerges at twice the Bragg angle θ_B defined by

$$\theta_B = \sin^{-1}\left(\frac{\lambda}{2d}\right) \quad (2.8)$$

Eq. (2.8) no longer applies simultaneously to the perfect and the distorted regions if the lattice spacing or lattice plane orientation vary locally due to structural defect.

In a diffraction experiment, we use a known λ and a measurement θ to obtain values of d/n for the sample. The slow rotation of the sample about its axis virtually ensures. The X-ray diffraction experimental setup is shown in Fig. 2.2.11. In this experiment, XRD measurements are carried out using Cu $K_{\alpha 1}$ (0.1542 nm) radiation, monochromated by the (111) reflection of a Ge single crystal. The sample and the X-ray detector are separated by 770 nm to eliminate any parasitic scattering of photons. The coherence length and strain are measured by the traditional 2θ - θ scan.

As for the θ -rocking scan (see Fig. 2.2.12), the X-ray beam intensity scattered from the sample is recorded while the sample is scanned through a reciprocal lattice point (rotation around a Bragg angle). The experimental rocking curves show several features that are related to the particular structural properties of the sample. One can characterize the strain fields completely and determine all the strain tensor elements of the distorted unit cell of the material by recording rocking curves in the vicinity of different reciprocal lattice points. Measurements carried out in symmetrical diffraction geometry monitor the strain fields along the growth direction, while rocking curves recorded in asymmetrical diffraction geometry are also sensitive to the in-plane strain. Using the result of θ -rocking scan, we can know the distribution of crystal direction and the scattered degree in the material.



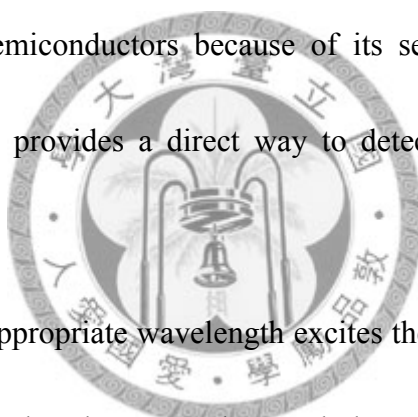
2.2.5 Scanning Electron Microscopy (SEM)

Scanning electron microscope (SEM) techniques provide measurements with a micron scale resolution. Therefore, we can determine defect microstructures, threading dislocations, plane-view, cross-section images and local values of physical properties. The term micro-characterization has come into use to emphasize this dual characteristic of SEM. SEM is powerful and versatile because (a) it has six modes of operation, which provide information about many different groups of properties of solid objects and (b)

the information is obtained essentially as electrical signals suitable for electronic data processing to provide quantitative values of many different properties as well as for presentation in various types of micrographs. The SEM is composed of two sub-systems, shown in Fig. 2.2.13.

2.3 Optical Analysis - Photoluminescence (PL)

Photoluminescence (PL) measurement is a very powerful tool in the assessment of optical properties of semiconductors because of its sensitivity, convenience, and non-destructive process. It provides a direct way to detect and identify energy-state distribution in materials.



A laser beam of an appropriate wavelength excites the electrons from the valence band to the conduction band and creates electron-hole pairs. When the electron-hole pairs recombine, the energy is released. There are two forms of released energy including nonradiative recombination and radiative recombination. Only radiative recombination can be detected. In our study, we performed temperature-dependent PL measurements to investigate the recombination mechanisms, which originates from spinodal decomposition and indium aggregated structures in InGaN well regions.

The standard PL experimental set up is shown in Fig. 2.3.1. The 325 nm-line of a 35 mW He-Cd laser is used for excitation. The samples to be measured were placed in a

cryostat for constant-temperature measurements at 300 K. PL photons from samples were collected with a lens and guided into a monochromator through a fiber bundle. The PL signals were monitored with a lock-in amplifier.



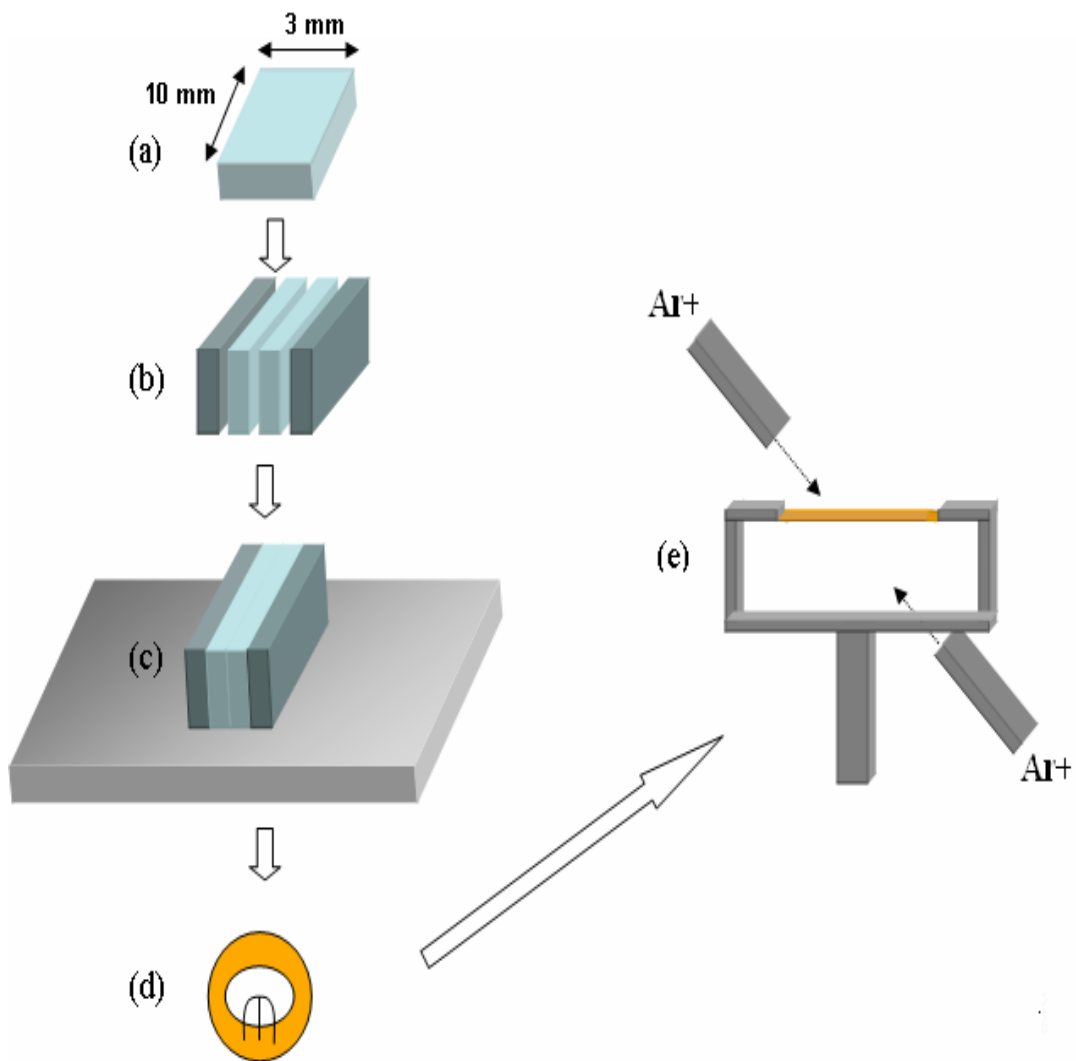


Fig. 2.1.1 Flow path of sample preparation.

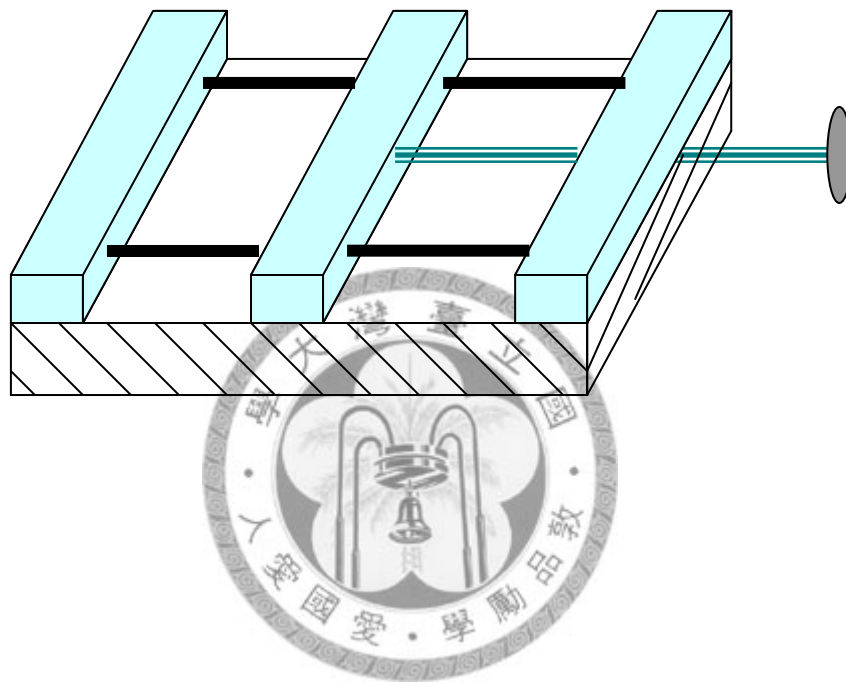


Fig. 2.1.2 Schematic drawing of the small vise.

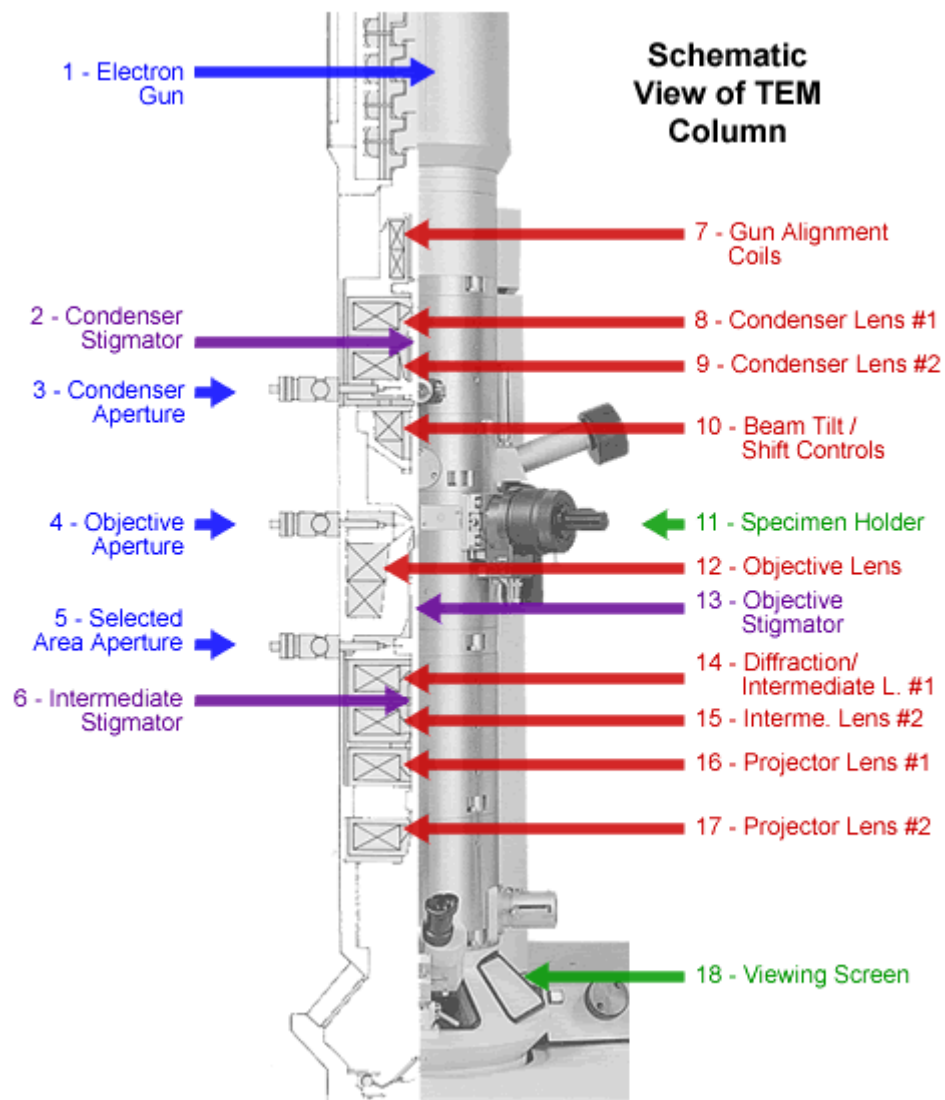


Fig. 2.2.1 A cutaway diagram of the transmission electron microscopy.

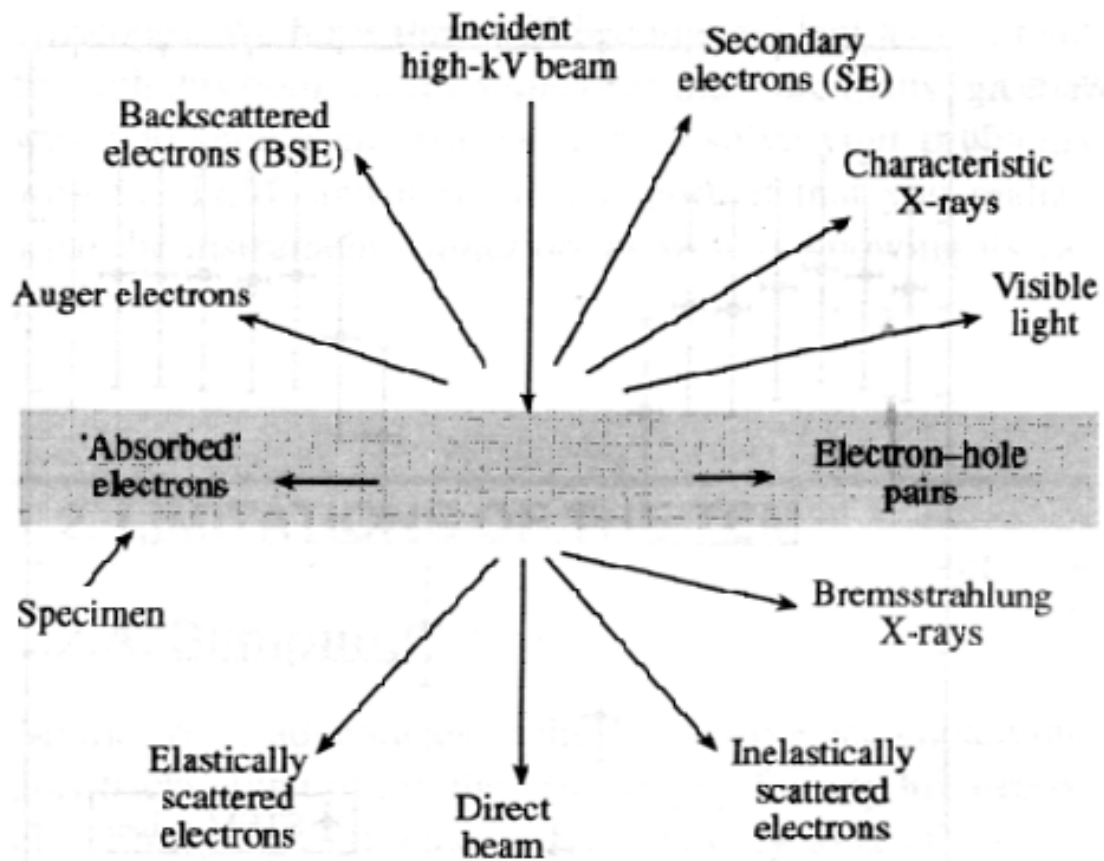


Fig. 2.2.2 Signal generated when a high-energy beam of electrons interacts with a thin specimen. Most of these signals can be detected in different types of TEM. The directions shown for each signal do not always represent the physical direction of the signal but indicate, in a relative manner, where the signal is strongest or where it is detected.

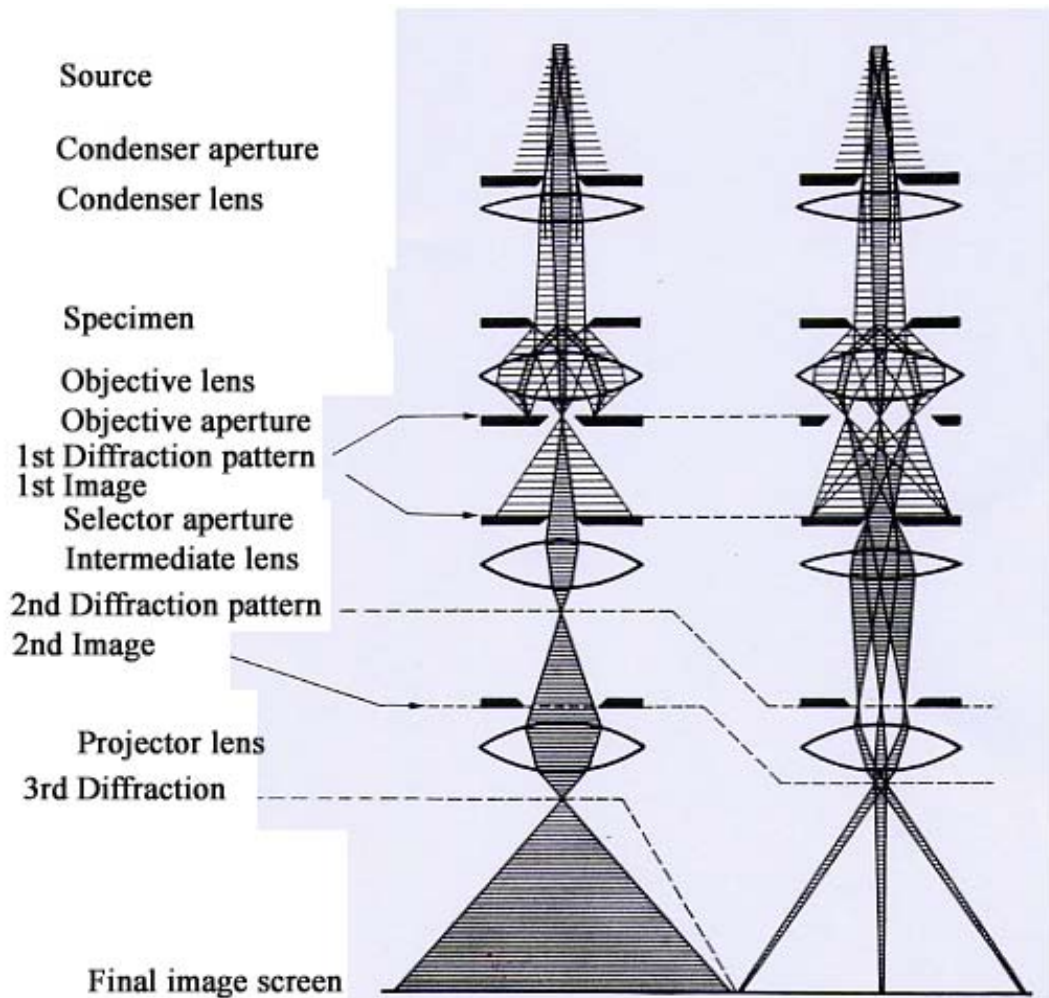


Fig. 2.2.3 Ray diagram for a transmission electron microscope in (a) the bright-field mode and (b) selected-area electron diffraction (SAED) mode.

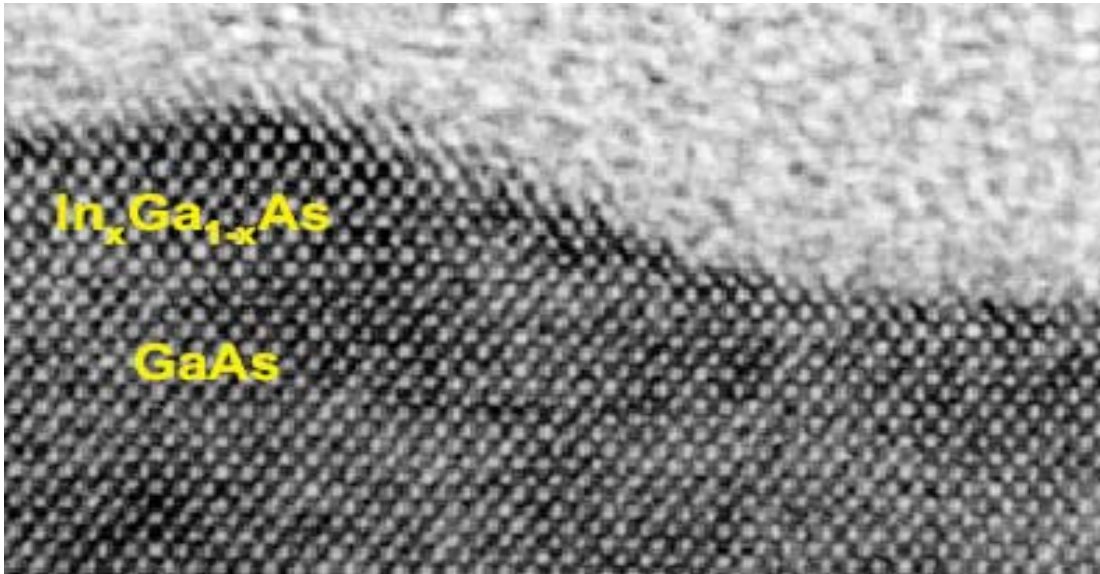


Fig. 2.2.4 HRTEM-image of a $In_{0.6}Ga_{0.4}As/GaAs$ Stranski-Krastanow island viewed along a $\langle 110 \rangle$ direction.

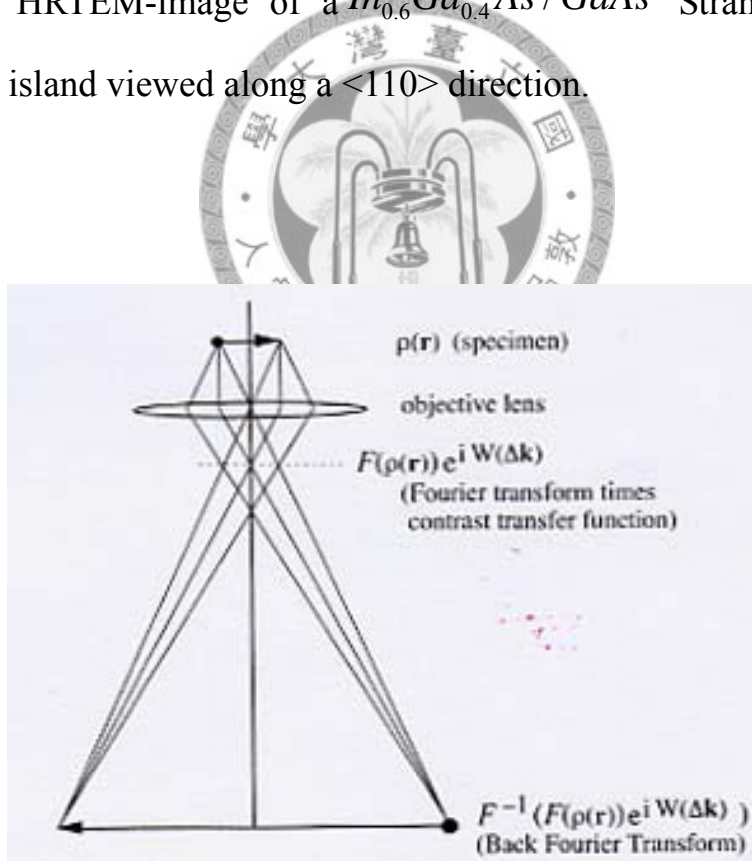


Fig. 2.2.5 Fourier transforms and planes of a ray diagram. The function $e^{iW(\Delta k)}$ accounts for the characteristics in the objective lens.

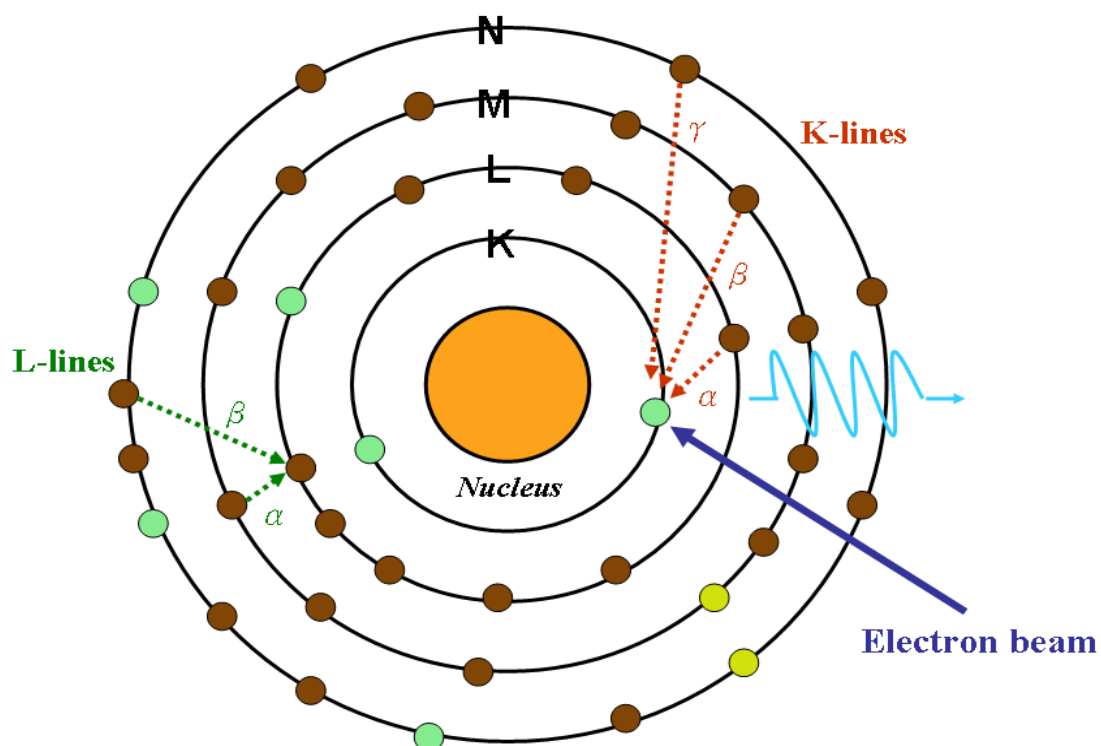


Fig. 2.2.6 The diagram of X-ray (K-lines and L-lines).

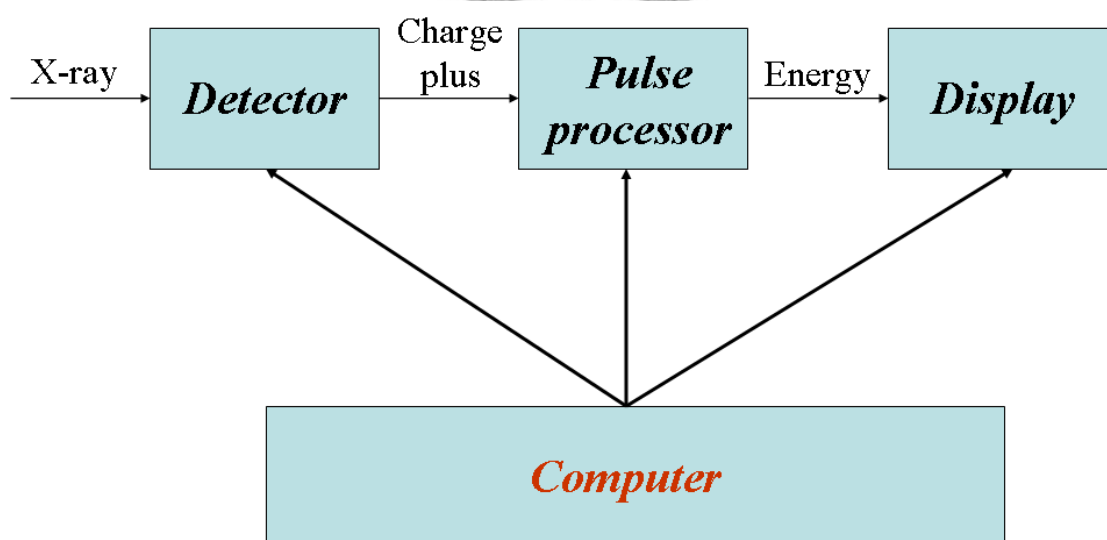


Fig. 2.2.7 Schematic process for the energy dispersive X-ray spectrum (EDX).

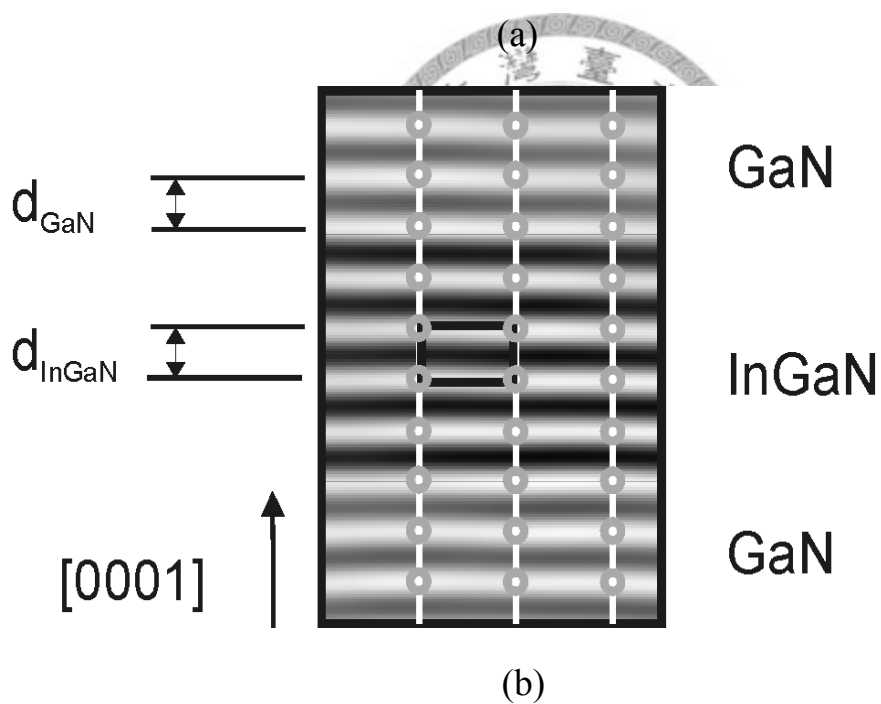
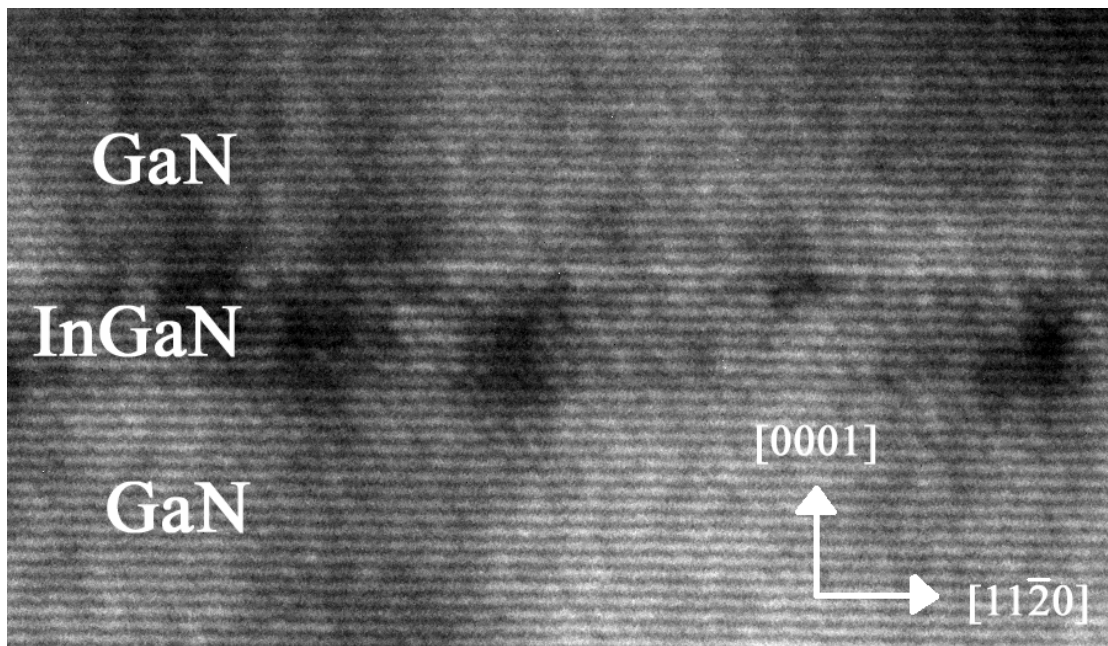


Fig. 2.2.8(a) (0002) lattice fringe image of a GaN/InGaN/GaN QW.

structure;

(b) Line scans are used to determine the intensity maximum positions of the fringes. The size of an image unit cell is indicated by the black rectangle.

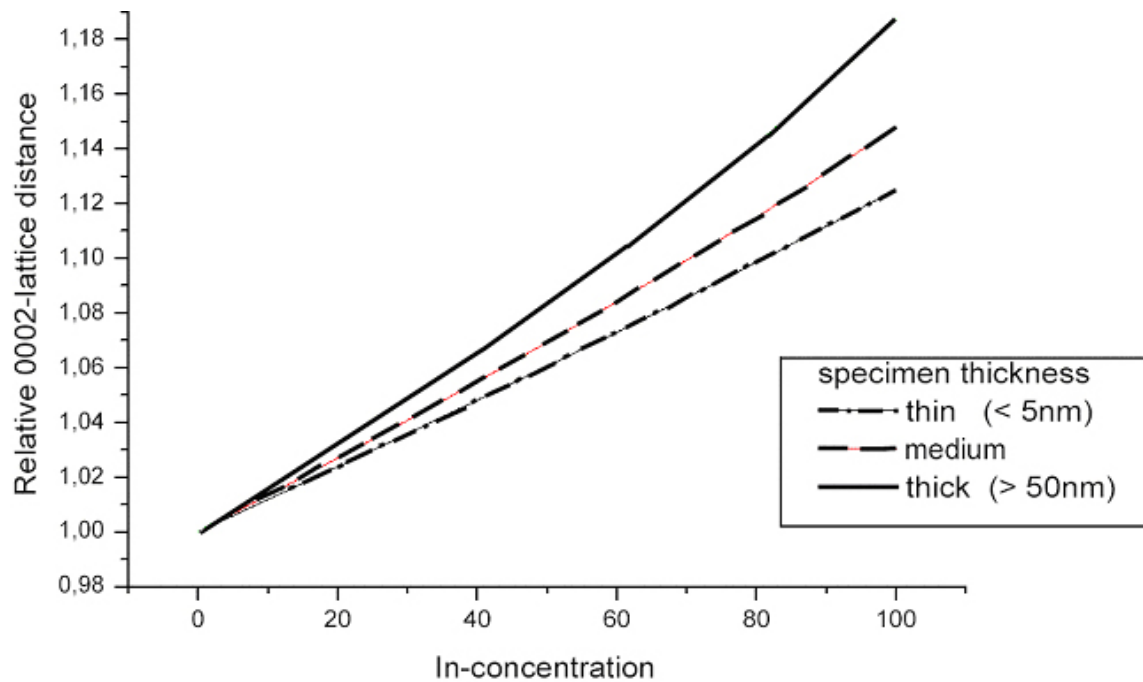


Fig. 2.2.9 Influence of the relaxation state on the normalized lattice parameters d_n plotted as a function of the In concentration. Biaxial strain state for a “thick” sample (solid line) and monoaxial strain state for a “thin” sample (dashed line).

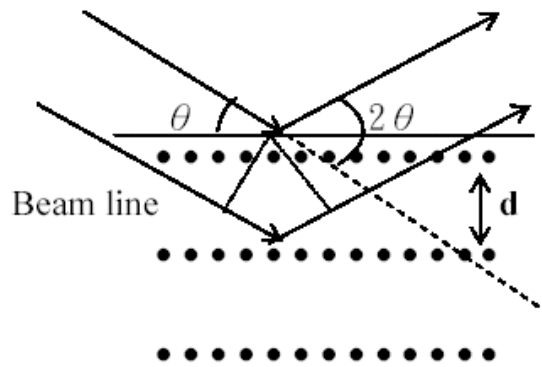


Fig. 2.2.10 Illustration of the Bragg condition.

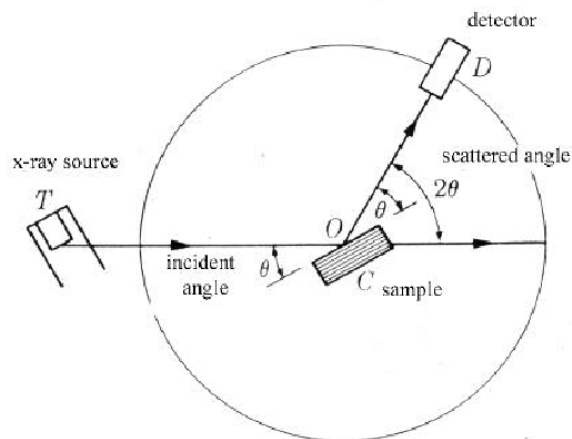


Fig. 2.2.11 X-ray diffraction setup (2θ - θ).

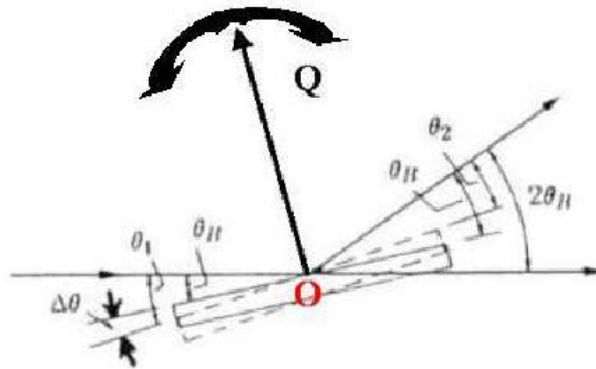


Fig. 2.2.12 θ -rocking setup.

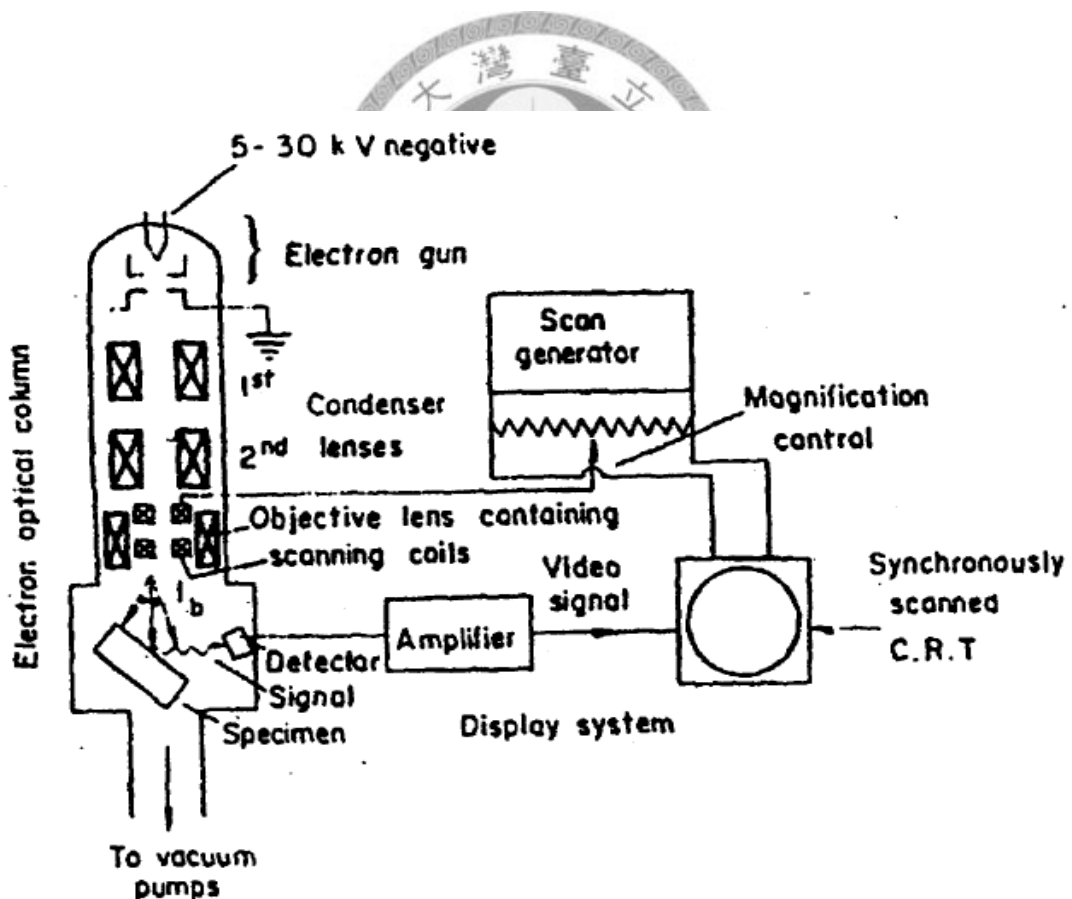


Fig. 2.2.13 SEM system, consisting of an electron optical column and a detection-amplification-display system.

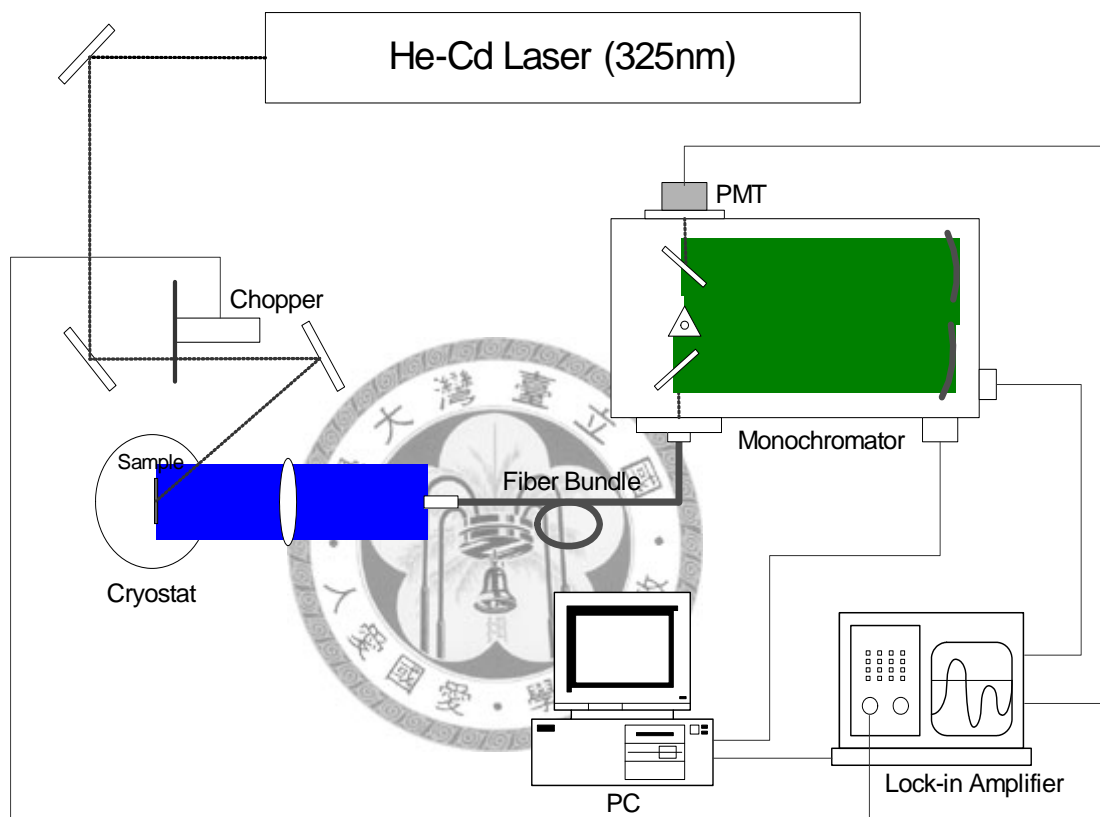
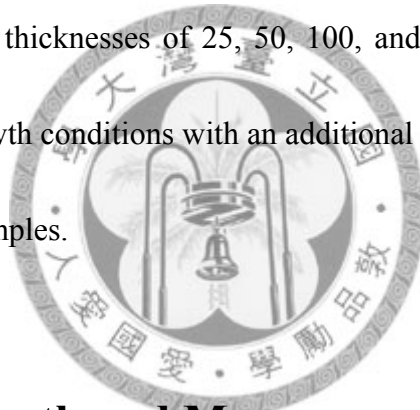


Fig. 2.3.1 The experiment setup for PL measurement.

Chapter 3

InGaN/GaN Single-heterostructures (SH) and Double-heterostructures (DH) With Various InGaN Thicknesses

In this chapter, we will compare the nanostructures and optical properties of two series of sample including single-heterostructures (SH) and double-heterostructures (DH) with various InGaN thicknesses of 25, 50, 100, and 200 nm. All samples were grown under the same growth conditions with an additional GaN caplayer grown at high temperature for the DH samples.



3.1 Sample Growth and Measurement Conditions

All samples were grown by metalorganic chemical vapor deposition (MOCVD). The InGaN/GaN SH samples were prepared in the following manner. First, a 2~3 μm undoped-GaN layer was grown on (0001) *c*-plane sapphire substrate at 1080 °C. Then, an InGaN layer was grown at a growth temperature of 700 °C. Various InGaN layer thicknesses were implemented at 25, 50, 100, and 200 nm. The DH samples were grown under the same conditions as those of the SH samples with an additional final GaN layer of 120 nm thickness grown at 920 °C. The detailed structures of these two series sample

are shown in Figs. 3.1.1.

X-ray diffraction (XRD) was used to measure reciprocal space mapping (RSM) in order to understand the strain condition in a sample. Indium content distribution can be calibrated based on the strain information. Omega-2theta ($\omega-2\theta$) scans were performed to understand the composition in a sample. Indium droplets can be detected based on the corresponding peak position in the $\omega-2\theta$ diagram. Scanning electron microscope (SEM) measurements were performed to compare the roughness of the SH and DH samples of different thicknesses. Energy dispersive X-ray spectrum (EDX) was measured to obtain the elemental distribution in a sample. The calibrated indium contents were confirmed by photoluminescence (PL) measurements by exciting from the top and bottom sides of the sample. Transmission electron microscopy (TEM) measurements were then performed to observe the indium droplets within the InGaN films of the DH samples.

3.2 Strain Conditions of SH and DH Samples

An example of RSM results is shown in Fig. 3.2.1. Figure 3.2.1(a) shows the RSM plot of an SH sample with the InGaN layer thickness at 200 nm and growth temperature of 700 °C. The bright spot at the upper-left corner represents GaN in the sample. A spot directly below the GaN spot is a fully strained material. A deviation from

the perpendicular demonstrates the amount of strain or relaxation in the material. The horizontally extended spot in the lower half portion stands for InGaN of a certain strain and indium distribution. A point (labeled by S) corresponds to a fully strained InGaN composition. A second point (labeled by R) corresponds to a fully relaxed InGaN composition. The trace from point S to R corresponds to the growth process of the InGaN layer from the fully strained condition (within the critical thickness) to a fully relaxed condition. In the early growth stage during the strained condition, the indium incorporation is low such that only 19 % indium composition is achieved. Indium content is increased to 27 % as strain is gradually relaxed. The RSM plot of a DH sample corresponding to the structure and growth condition of the sample is shown in Fig. 3.2.1(b). Here, one can see that almost the whole InGaN layer is fully strained. This is so because the InGaN layer is compressively strained by GaN from its top and bottom.

3.3 InGaN/GaN Single-heterostructures

3.3.1 XRD and HRTEM Results

Figure 3.3.1 shows XRD (ω - 2θ scans) of SH samples with different thicknesses, including 25, 50, 100, and 200 nm. Here, only the GaN and InGaN peaks are seen (labeled in Fig. 3.3.1). No phase separation is seen near the InGaN peak.

HRTEM images of the four SH samples are shown in Fig. 3.3.2. Here, we can see the general structures of the four samples. Figure 3.3.2(a) shows the cross-section HRTEM image of SH 25nm. The arrow indicates the direction of (0001) from the substrate. The G1 glue and InGaN thin film can be seen. The different atomic masses, indium (49) is higher than that of gallium (31), causing the contrast in an HRTEM image. The heavier atom results in a darker color in an image. Figures 3.3.2(b), (c), and (d) show the cross-section HRTEM images of samples SH 50, 100, and 200 nm, respectively. Then, we compare the roughness of the above-mentioned four SH samples. We find that the InGaN layer roughness increases with an increase of InGaN thickness. SEM results will show clearer evidence.



3.3.2 SEM Results

SEM studies were performed to more clearly demonstrate the surface roughness of these four SH samples of different thicknesses. The plane-view SEM images of samples SH 25, 50, 100, and 200 nm are shown in Figs. 3.3.3(a), (b), (c), and (d), respectively. We can observe the surface roughness on the plane-view SEM image. They are quite different. The 200nm sample clearly shows valleys and peaks over the surface. The images show that the surface becomes smoother as the sample thickness decreases. As we discussed in section 3.2, RSM plot (Fig. 3.2.1 (a)) of sample SH 200 nm showed

the growth process of an InGaN layer from a fully strained condition (within the critical thickness) to a fully relaxed condition. So, when the strain starts to relax, surface roughness will rise. We have directly confirmed that when the thickness of InGaN layer increases, the roughness also rises.

3.3.3 PL Measurements and EDX Results

PL measurements were excited from the top (the film side) and bottom (the polished backside) of the samples from 10 through 210 K, as shown in Figs. 3.3.4(a) and (b). Figure 3.3.4(a) and (b) show the PL measurement results of the most upper and lower portions of the InGaN layers, respectively, because the penetration depth of the excitation UV laser (390 nm) in InGaN is only around 100 nm. From Figs. 3.3.4(a) and (b), one can see that the upper (lower) InGaN layer mainly emits green (blue) light around 520 (460) nm even though a small shoulder can be seen in the blue (green) range. These PL measurements are consistent with the RSM results above, i.e., the upper (lower) InGaN layer has higher (lower) indium content.

EDX was used to estimate indium content for matching the above PL measurements. Here, we can only obtain the relative indium content because of the uncertain incident angle of the electron beam. Figure 3.3.5(a) shows the direction (red arrow) of the eight points measured by EDX in SH 200 nm. The white arrow indicates

the direction of (0001) from the substrate. Then, the data at the eight points were used to draw a diagram for the relative indium content versus points (as shown in Fig. 3.3.5(b)). Here, we find that indium content increases with height. However, the indium contents of the last three points decrease. This result might be due to indium escape under the thermal treatment of the SH samples after growth. The thermal treatment of SH samples means that right after closing the MO sources, the samples are still in an environment of hydride gases and high temperature for a few more minutes. This may lead to InGaN decomposition from the upper most surface. Generally, the EDX data are consistent with the above PL measurements.

3.4 InGaN/GaN Double-heterostructures

3.4.1 XRD, HRTEM, and SEM Results

In this section, we compare the different properties between SH and DH samples. XRD (ω - 2θ scan) of DH samples of different thicknesses, including 25, 50, 100, and 200 nm are shown in Fig. 3.4.1. Here, we can see additional peaks besides GaN and main InGaN peak showing the occurrence of phase separation in the InGaN layer (labeled in Fig. 3.4.1). Hartono *et al* [1] attempted to grow InN directly on GaN, which resulted in indium droplet formation. They showed that XRD and the peak for indium droplets were consistent with our data. It is possible that indium droplets have been

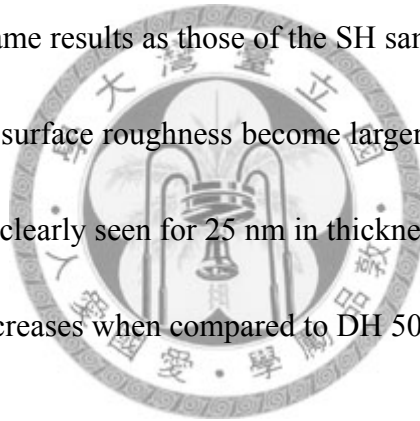
formed in the InGaN layer.

Then, we performed HRTEM experiments on the DH samples to understand the formation of indium droplets. The cross-section HRTEM images of DH 200 nm and the TEM images of higher magnification of the indium droplet in DH 200nm are shown in Fig. 3.4.2. One can observe holes in these images, which might be due to the removal of indium droplets during TEM sample preparation. EDX was used to analyze the other indium droplet images without holes. The cross-section HRTEM images of DH 50 nm is shown in Fig. 3.4.3. We used EDX for four points (labeled 1~4). The EDX results are shown in Table 3.4.1. Point 1 can be regarded as a indium-rich area in the InGaN layer. We find almost no indium signal in points 3 and 4 of the InGaN layer. Because of that we have to thin the sample down to less than 1 μ m and then milled by argon-ion gas for several minutes. So, we guess that the indium droplet has fallen off during sample preparation. The lighter regions in the HRTEM image of DH 50 nm (as shown in Fig. 3.4.3) can be regarded as the original indium droplets.

Next, we try to understand the distribution of indium droplets of the DH samples of the four different InGaN thicknesses. Figures 3.4.4(a), (b), (c), and (d) show the low-magnification cross-section HRTEM images of the DH samples 25, 50, 100, and 200 nm, respectively. We compare the distributions of indium droplets of the four DH samples. We find that the density of indium droplet decreases when the thickness of the

InGaN layer decreases. The higher magnification cross-section HRTEM images of the DH 25 nm sample is shown in Fig. 3.4.5. One can see that there is almost no indium droplet in this image. The TEM result of DH 25 nm is consistent with the XRD result above (see Fig. 3.4.1).

Figures 3.4.6(a), (b), (c), and (d) show the plane-view SEM images of the DH samples 25, 50, 100, and 200 nm, respectively. We can observe that the DH surface roughnesses are similar to what was seen in the plane-view SEM images for the SH samples. We also see the same results as those of the SH samples: when the thickness of InGaN layer increases, the surface roughness become larger. This is not clearly seen for 50, 100, and 200 nm but is clearly seen for 25 nm in thickness. The surface roughness of DH 25 nm dramatically decreases when compared to DH 50 nm.

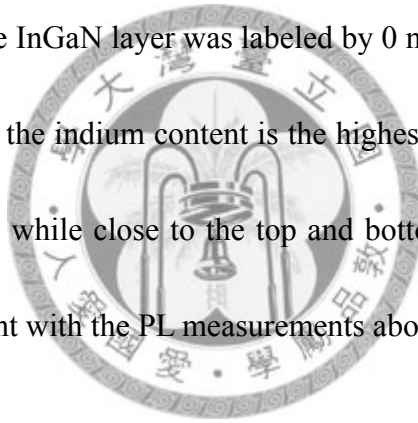


3.4.2 PL Measurements and EDX Results

Low-temperature PL spectra of the above DH samples when the samples are excited from the top and bottom are shown in Figs. 3.4.7(a) and (b), respectively. Here, one can see that the major PL peaks are always in the blue range even though there is a minor peak in the green range in the case of top excitation. These PL results are also consistent with what was observed from RSM. We can conclude that in a DH sample, except a middle thin layer of InGaN that is strain relaxed, most portions of the InGaN

layer in the top and bottom are fully strained such that the indium contents are only 19 % and the emissions are in the blue range.

EDX was used to estimate indium content for matching the above PL measurement. The direction (the red arrow) of the nine points that were measured with EDX in DH 200 nm is shown in Fig. 3.4.8(a). The white arrow indicates the direction of (0001) from the substrate. Then, we use the nine points to draw a diagram for the relative indium content variation with height (as shown in Fig. 3.4.8(b)). The lowest point along the c-axis of the InGaN layer was labeled by 0 nm in height. Here, we check the EDX data and find that the indium content is the highest in the middle region of the InGaN layer and decreases while close to the top and bottom of the InGaN layer. The EDX data are also consistent with the PL measurements above.



3.5 Discussions

We have demonstrated the variations of strain and indium composition of an InGaN layer in InGaN/GaN single-heterostructures and double-heterostructures based on the RSM and PL measurements. In the SH samples, InGaN with low (bottom) and high (top) indium contents can be identified. On the other hand, only a thin layer of strain relaxed InGaN in the middle in a DH sample can be observed. In the SEM results, we observe that when strain starts to relax, the surface roughness increases. The quality

of epitaxy decreases. In the DH samples, formation of indium droplets has been observed and confirmed based on HRTEM study. Indium droplet formation due to phase separation will lead to poor electric property. In another HRTEM result of DH samples, we find that as the thickness of the InGaN layer decreases, the density of indium droplet is also decreased. Therefore, it is necessary to grow thinner InGaN layers to avoid the formation of indium droplet. However, one layer may not be enough for sufficient absorption for solar cell applications. In the next chapter, we will demonstrate our measurements of multi-InGaN-layer structures. Such indium composition distribution can be used for fabricating multi-thin film solar cells.



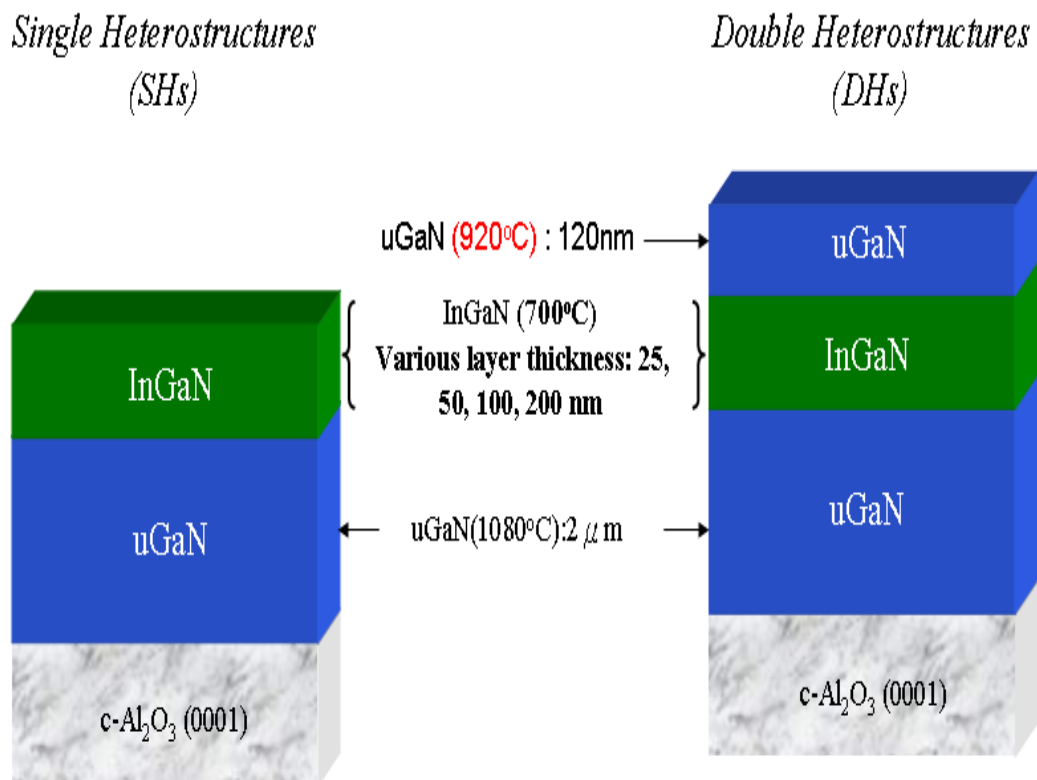


Fig. 3.1.1 Structures of SH and DH samples.

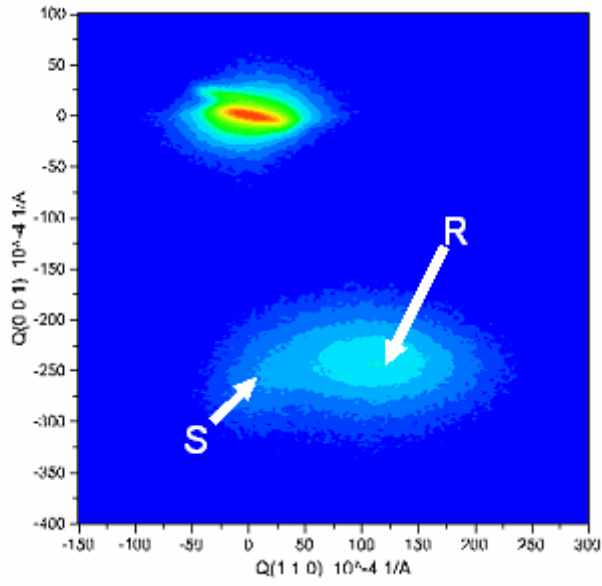


Fig. 3.2.1(a) RSM plot of a SH sample with 200-nm InGaN grown at 700 °C.

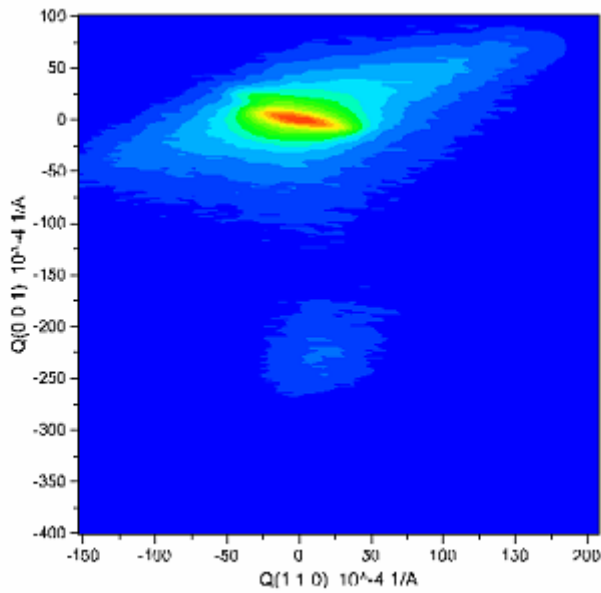


Fig. 3.2.1(b) RSM plot of a DH sample with 200-nm InGaN grown at 700 °C.

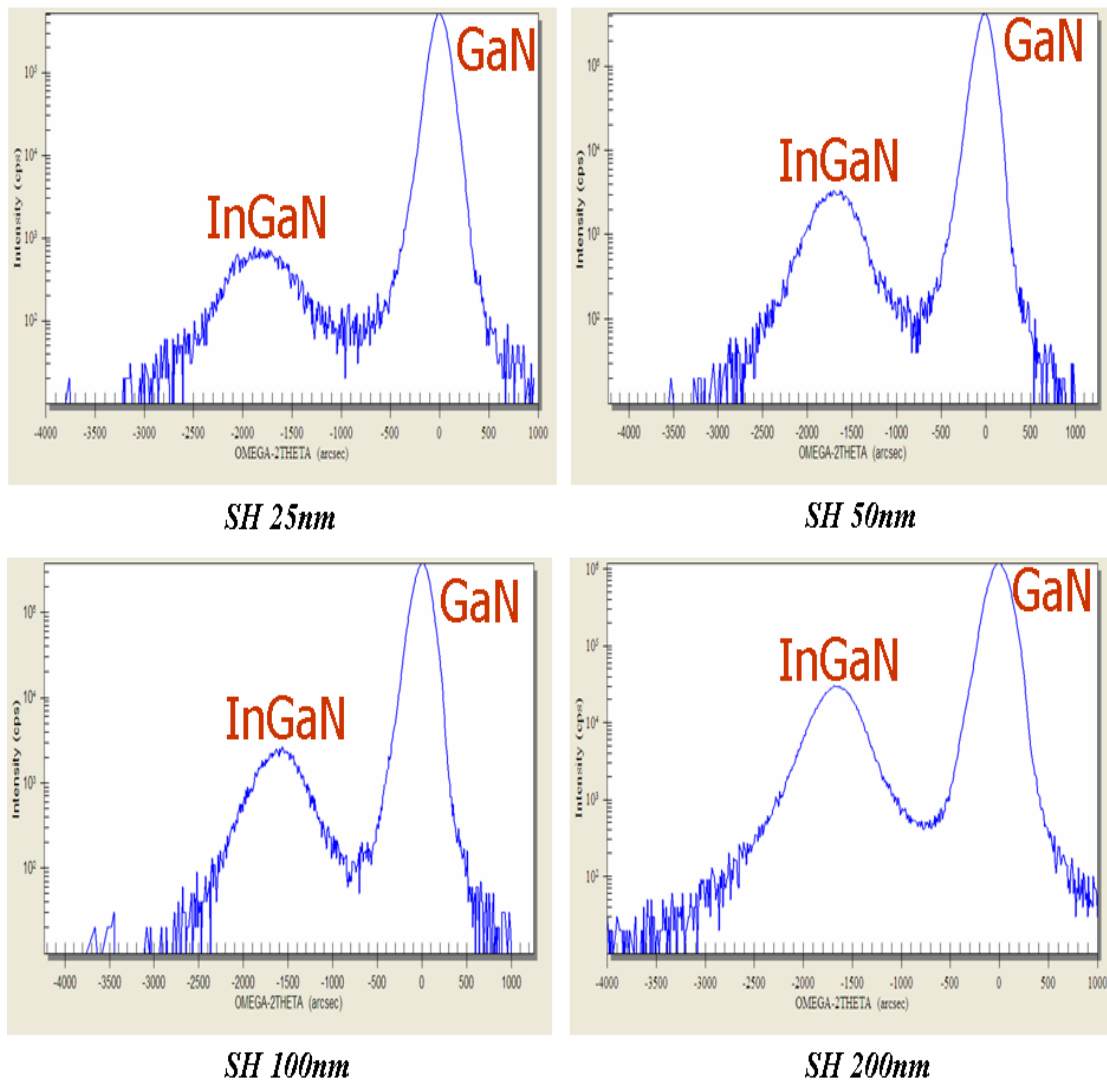


Fig. 3.3.1 X-ray diffraction pattern (ω - 2θ scan curves) of SH samples with four different thicknesses.

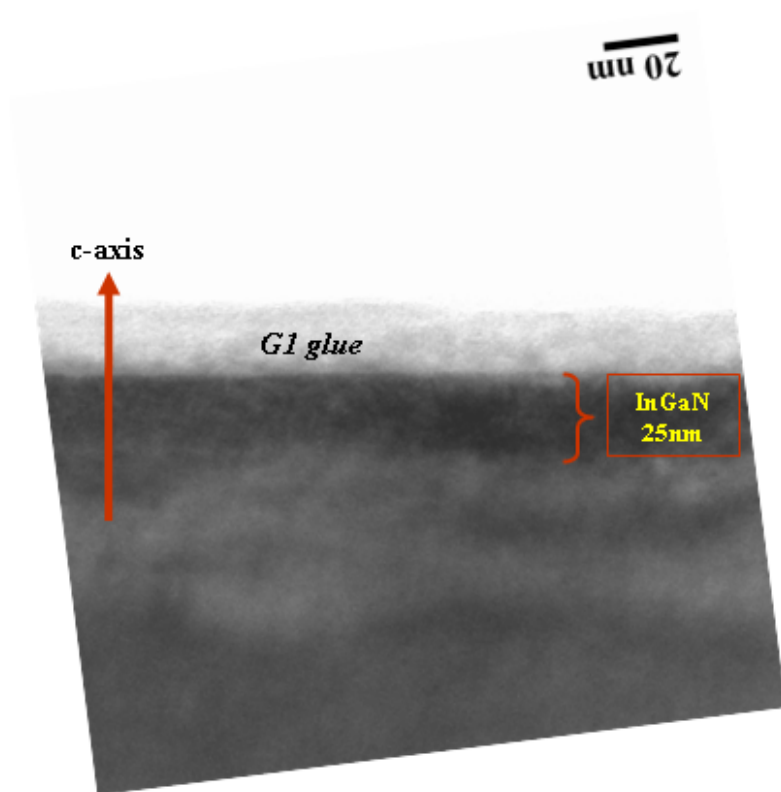


Fig. 3.3.2(a) Cross-section HRTEM images of SH 25nm.

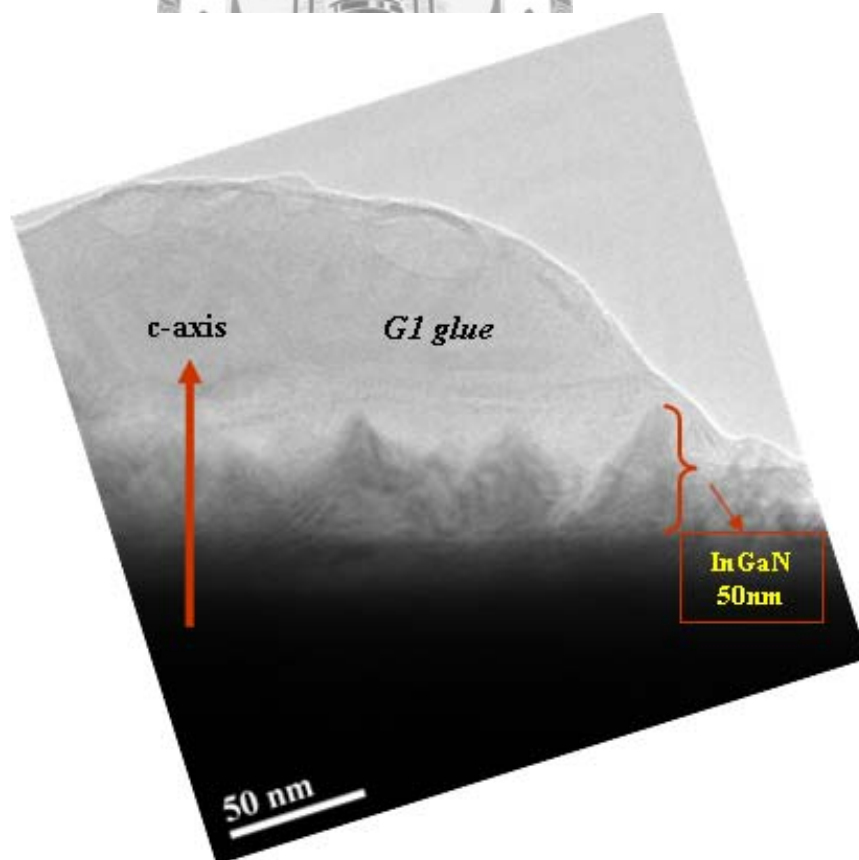


Fig. 3.3.2(b) Cross-section HRTEM images of SH 50nm.

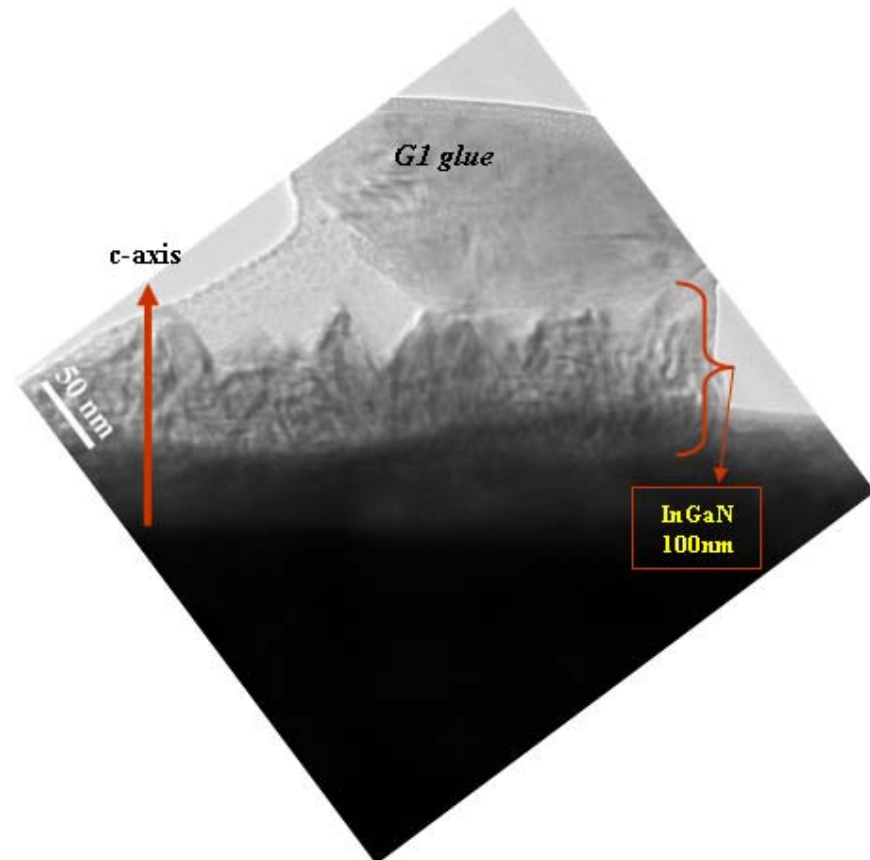


Fig. 3.3.2(c) Cross-section HRTEM images of SH 100nm.

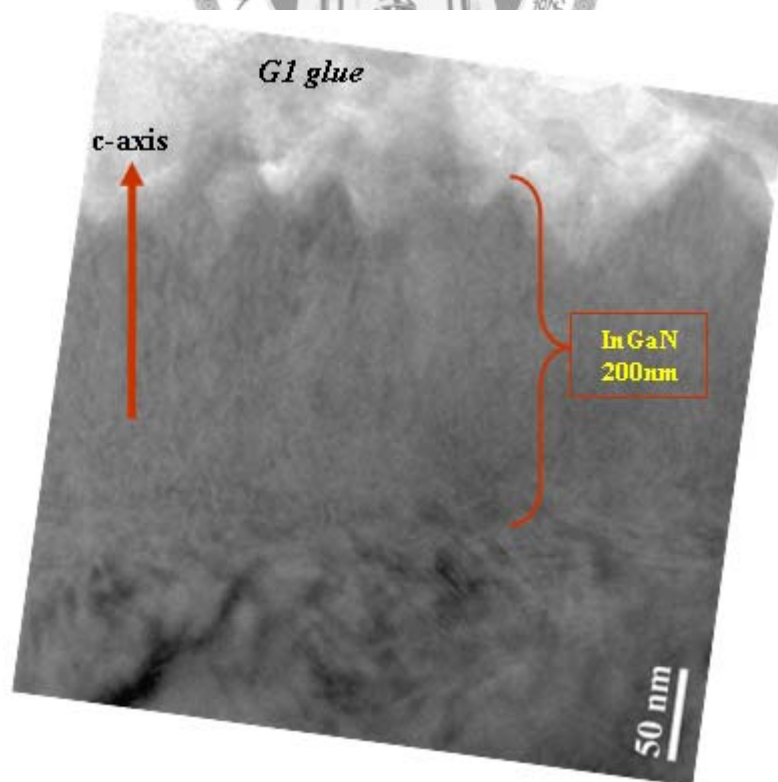


Fig. 3.3.2(d) Cross-section HRTEM images of SH 200nm.

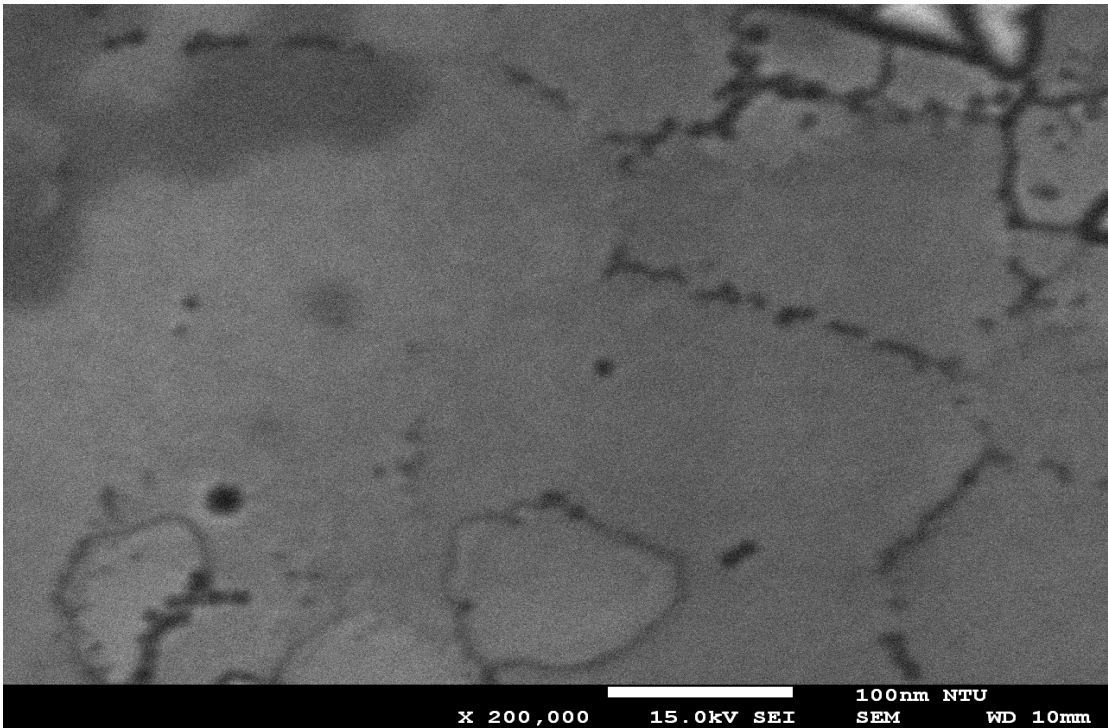


Fig. 3.3.3(a) Plane-view SEM image of SH 25 nm.

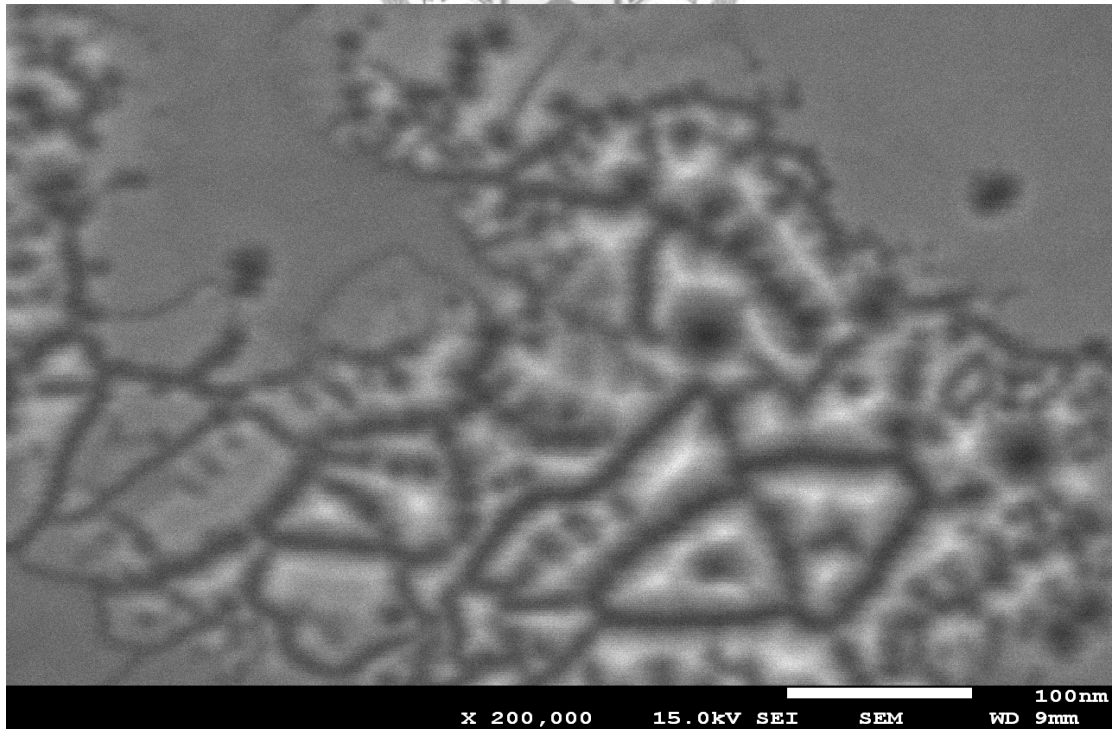


Fig. 3.3.3(b) Plane-view SEM image of SH 50 nm.

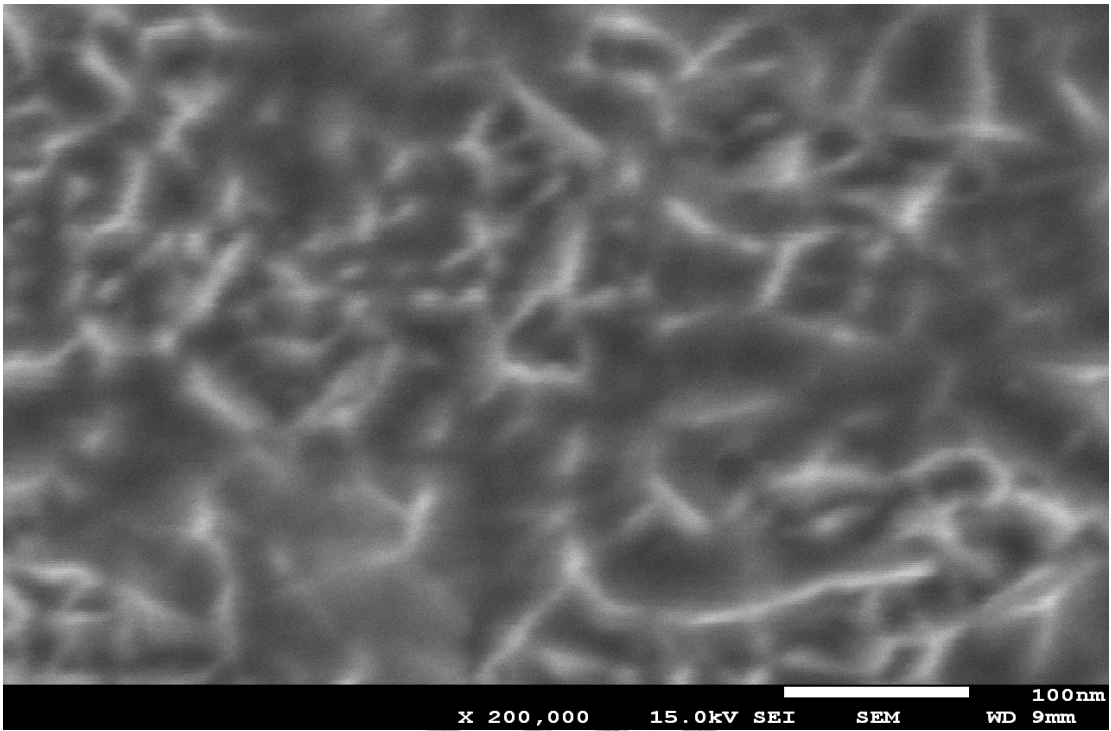


Fig. 3.3.3(c) Plane-view SEM image of SH 100 nm.

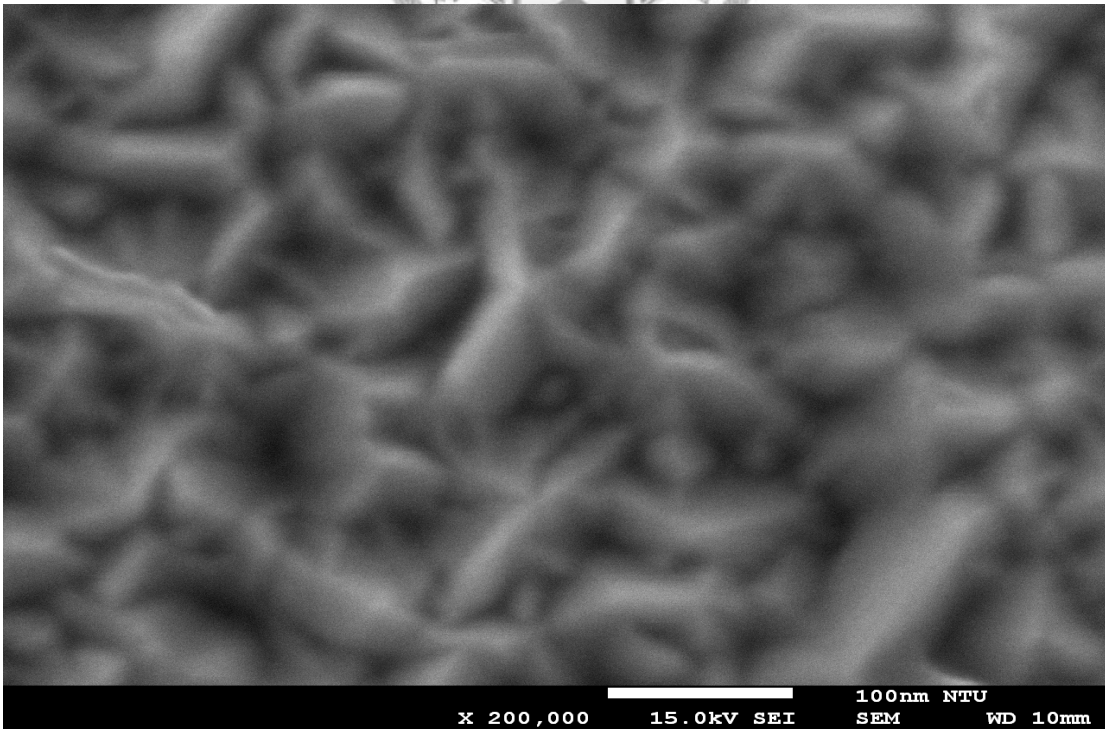


Fig. 3.3.3(d) Plane-view SEM image of SH 200 nm.

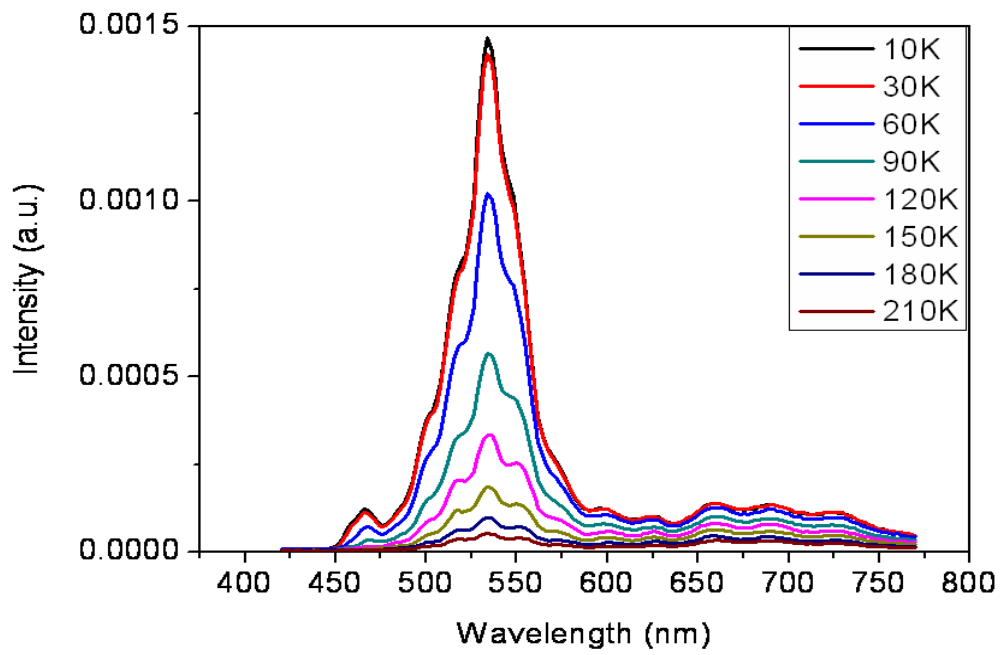


Fig. 3.3.4(a) PL spectra of sample SH 200 nm with excitation from the top.

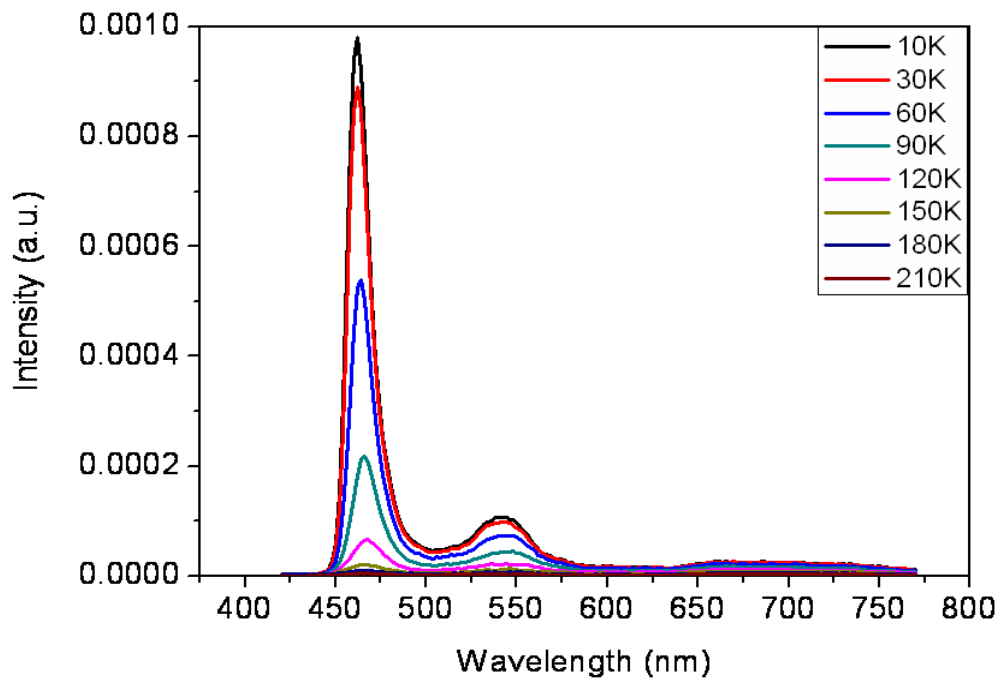


Fig. 3.3.4(b) PL spectra of sample SH 200 nm with excitation from the bottom.

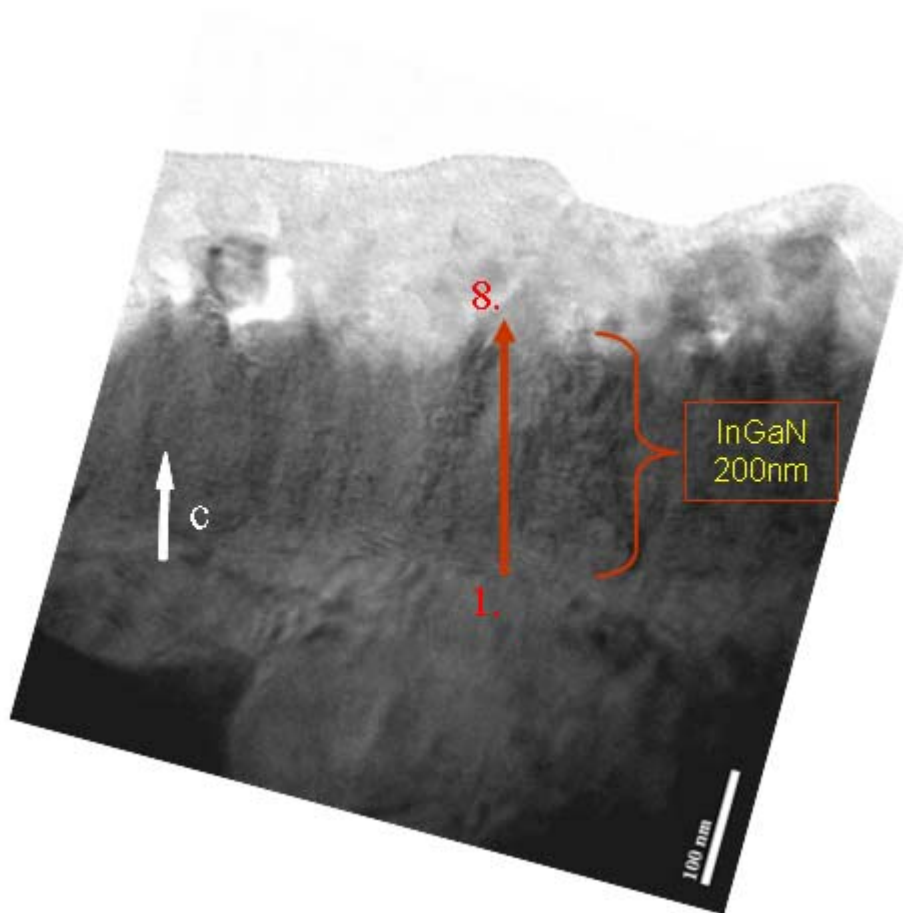


Fig. 3.3.5(a) The direction (red arrow) of the eight points that were measured by EDX in SH 200 nm.

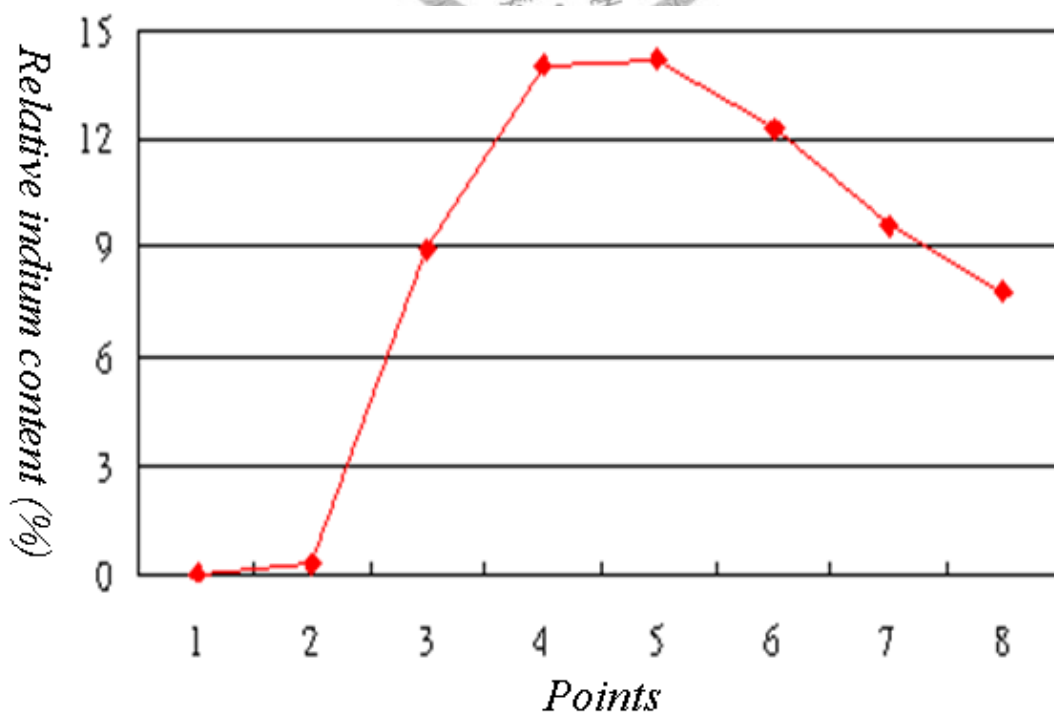


Fig. 3.3.5(b) The trend of the relative indium content of SH 200 nm.

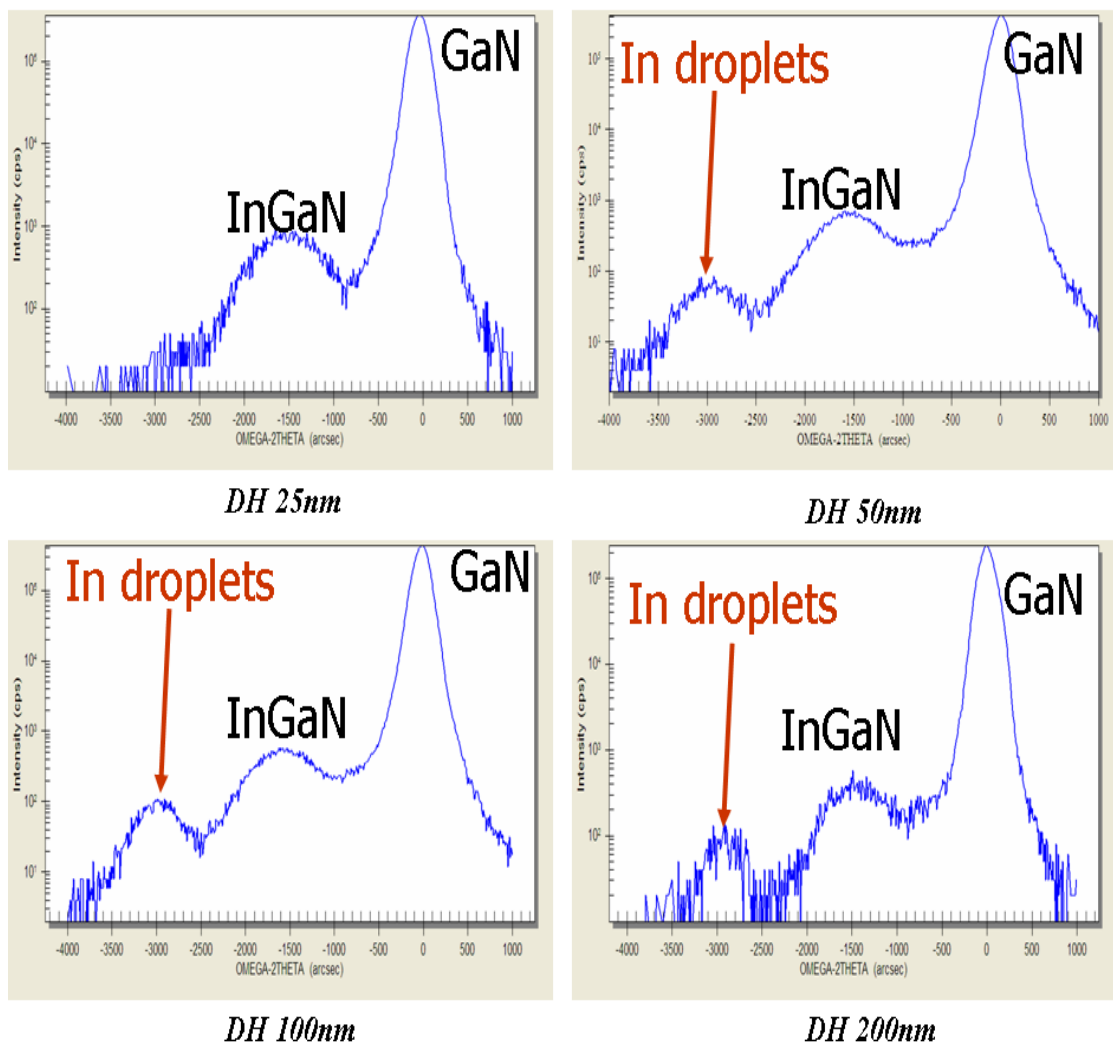


Fig. 3.4.1 X-ray diffraction pattern (ω - 2θ scan curves) of DH samples with four different thicknesses.

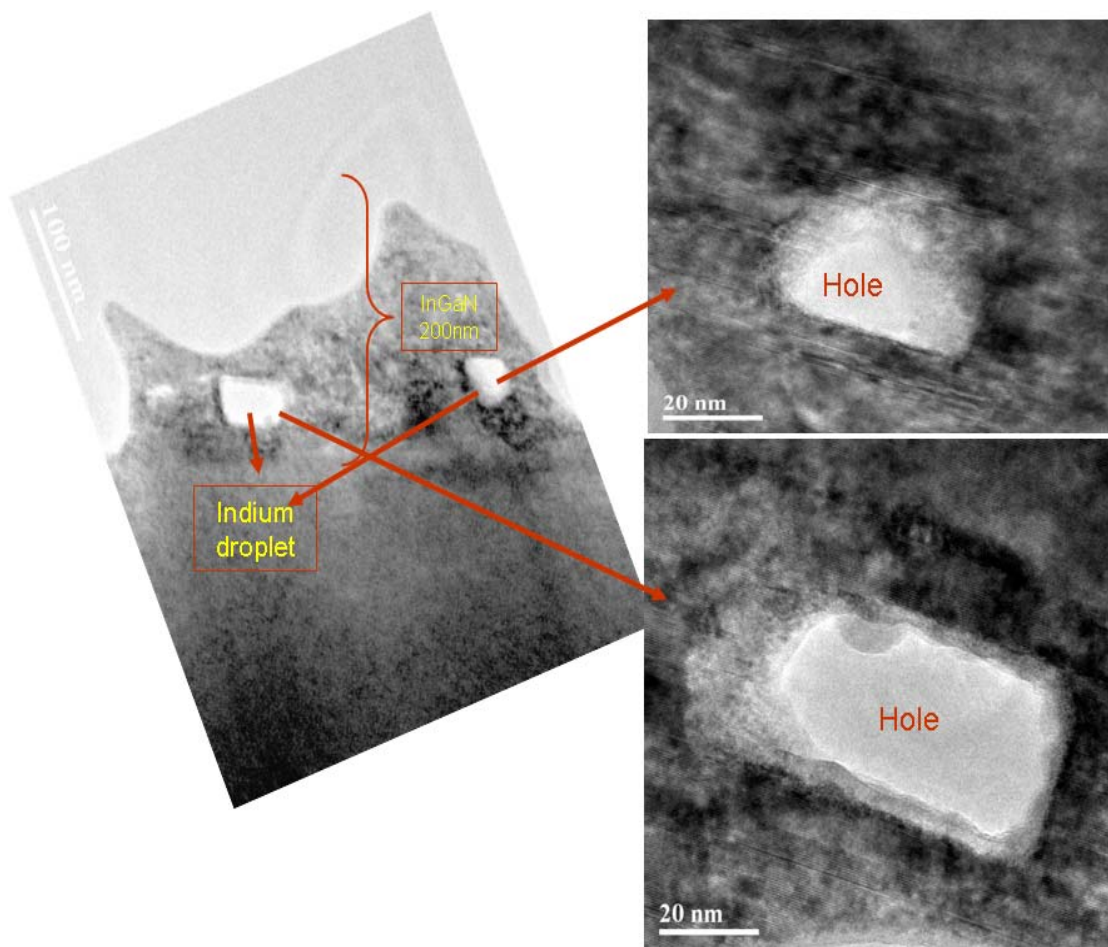


Fig. 3.4.2 Cross-section HRTEM images of DH 200 nm and indium droplets.

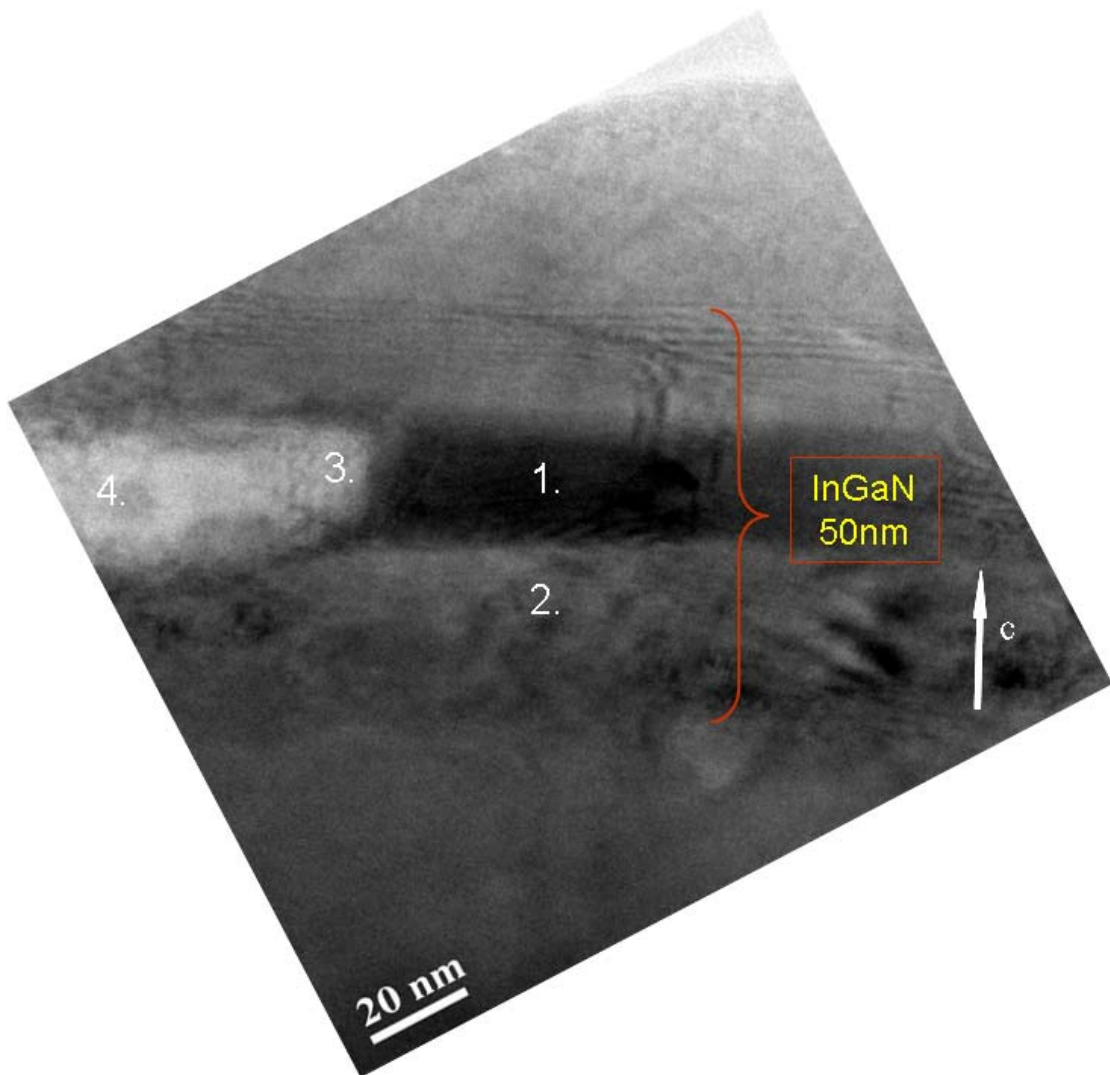
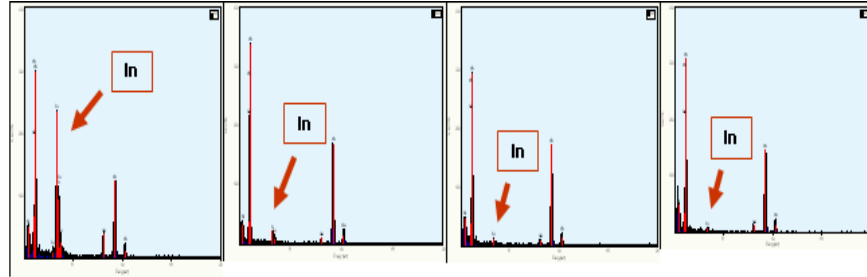


Fig. 3.4.3 The four points (labeled by 1~4) for EDX measurement in DH 50 nm.

Table 3.4.1 Relative indium contents of the four points in Fig. 3.4.3 from EDX measurement.



<i>Point</i>	1.	2.	3.	4.
<i>Relative indium content(%)</i>				
<i>Element</i>				
N(K)	44.64	44.46	59.80	56.41
Ga(K)	26.41	51.10	38.78	43.29
In(L)	28.93	4.42	1.41	0.29

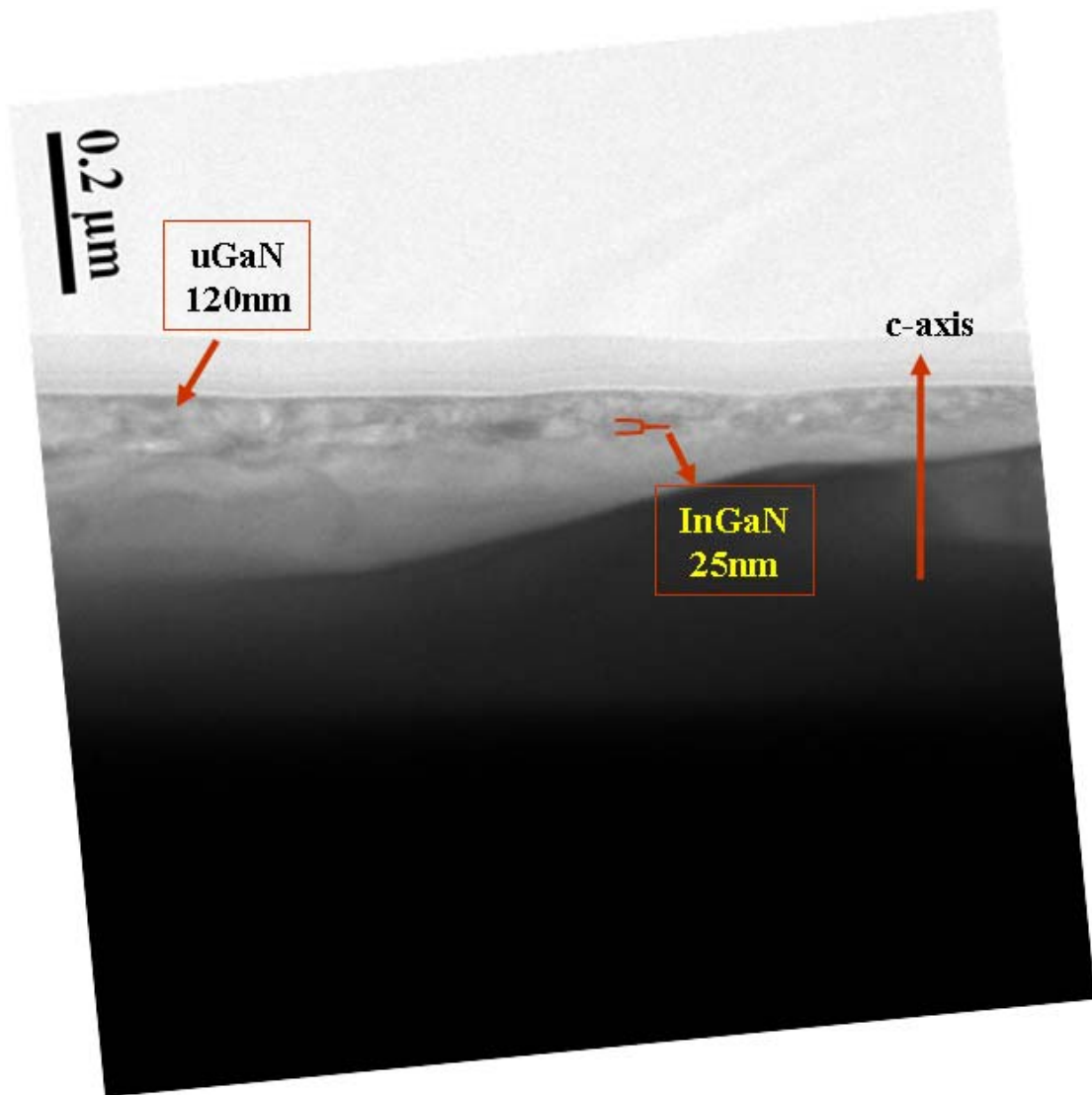


Fig. 3.4.4(a) Low-magnification cross-section HRTEM images of DH 25 nm.

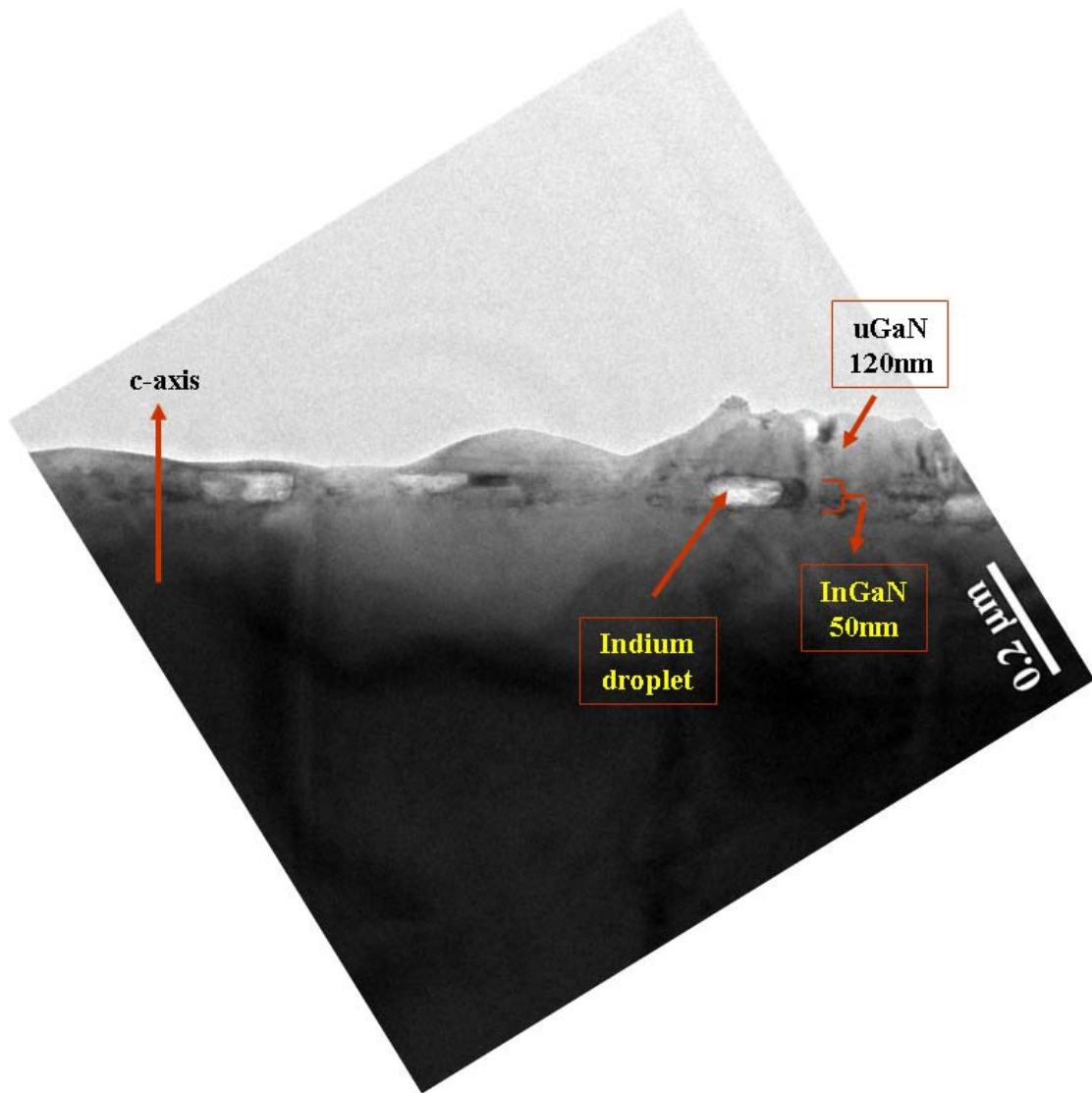


Fig. 3.4.4(b) Low-magnification cross-section HRTEM images of DH 50 nm.

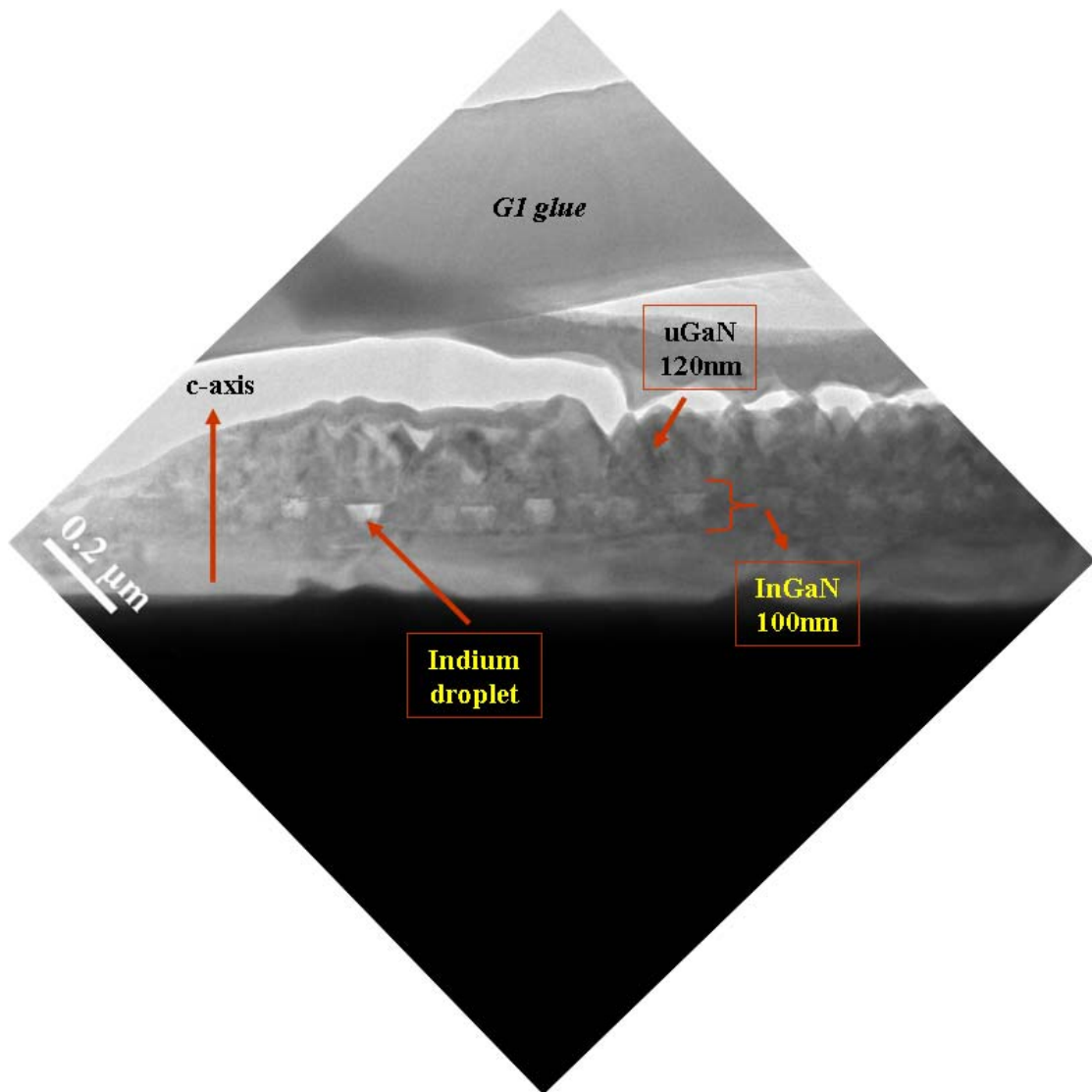


Fig. 3.4.4(c) Low-magnification cross-section HRTEM images of DH 100 nm.

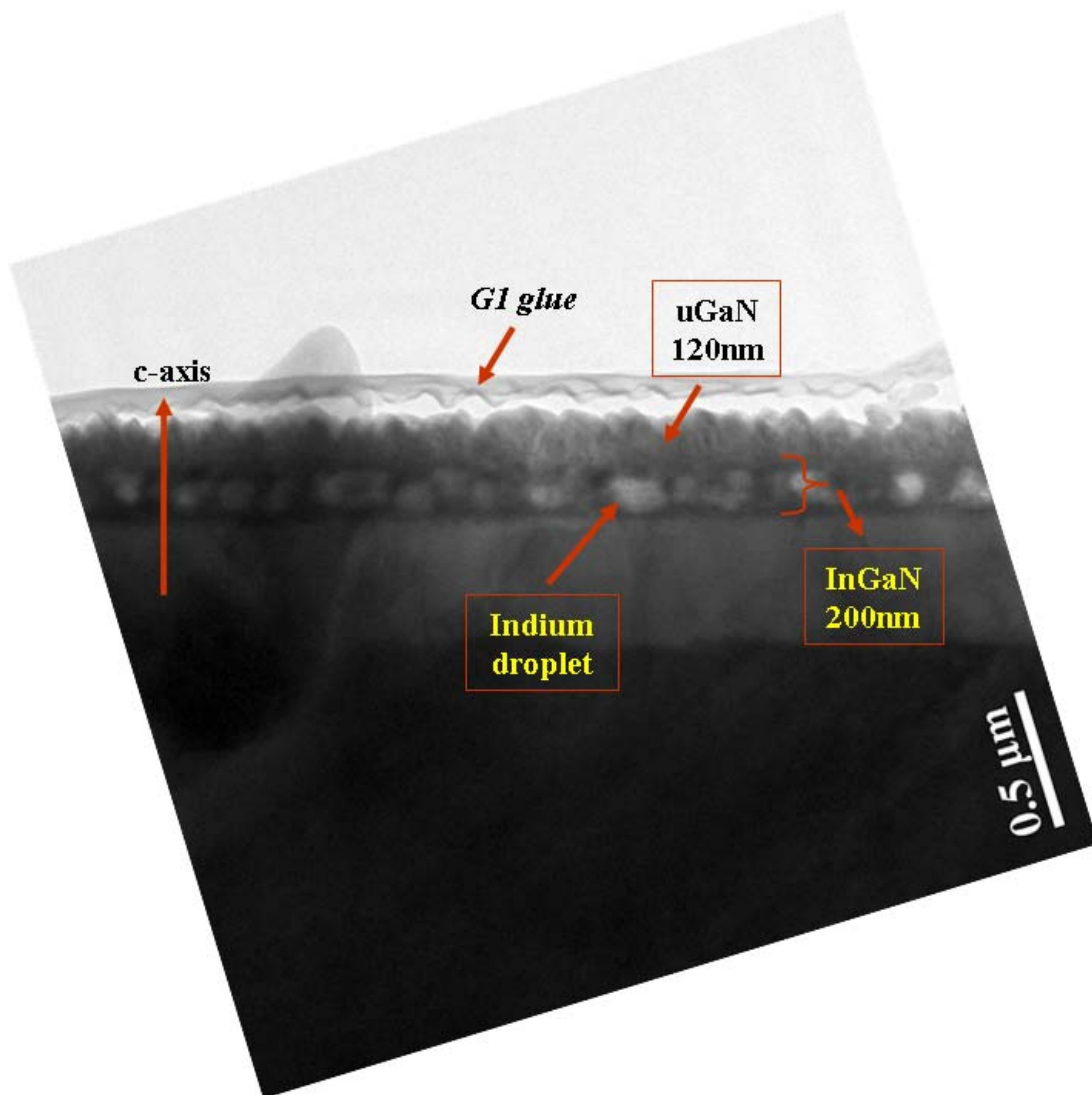


Fig. 3.4.4(d) Low-magnification cross-section HRTEM images of DH 200 nm.

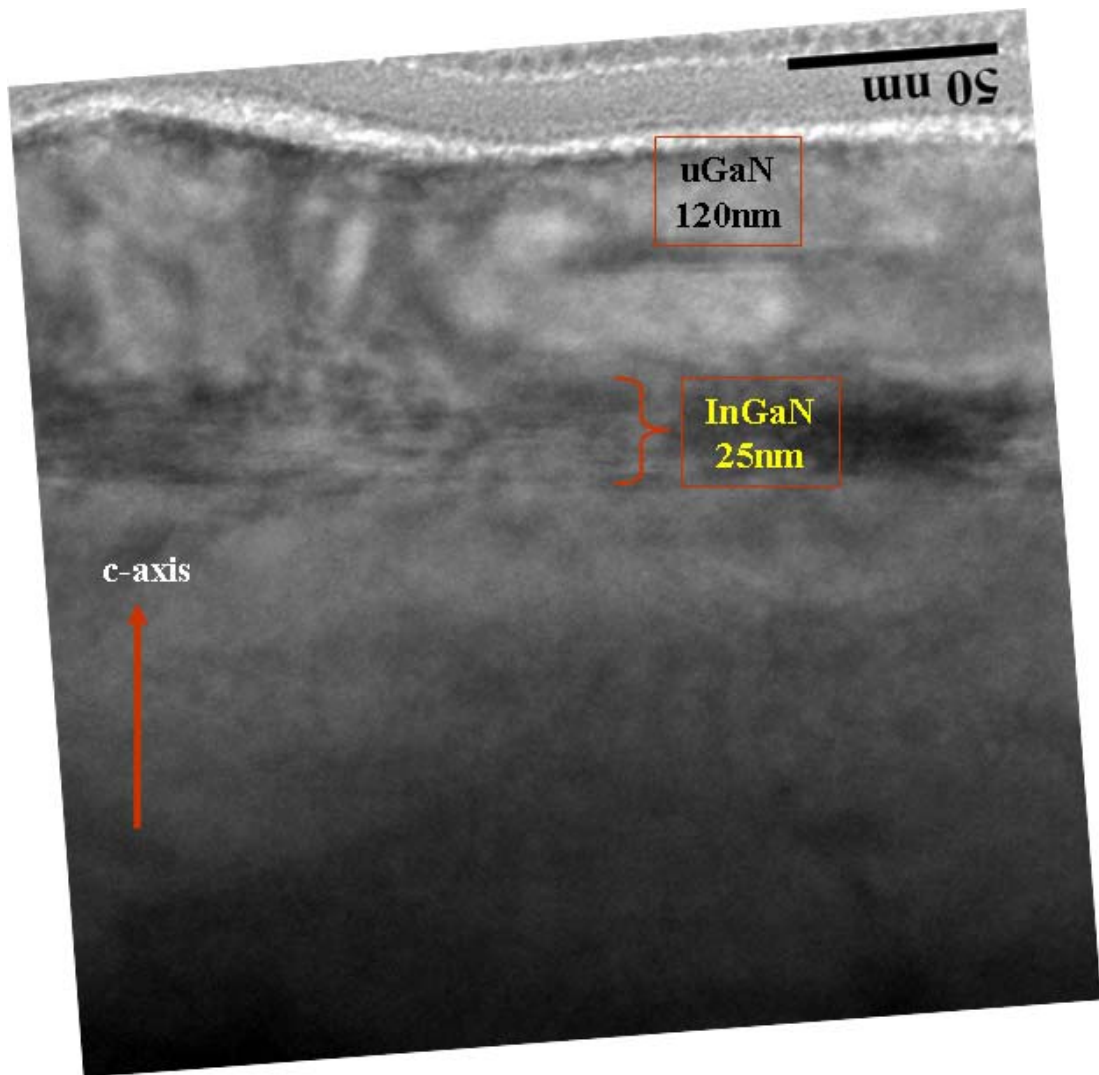


Fig. 3.4.5 Higher-magnification cross-section HRTEM images of DH 25nm.

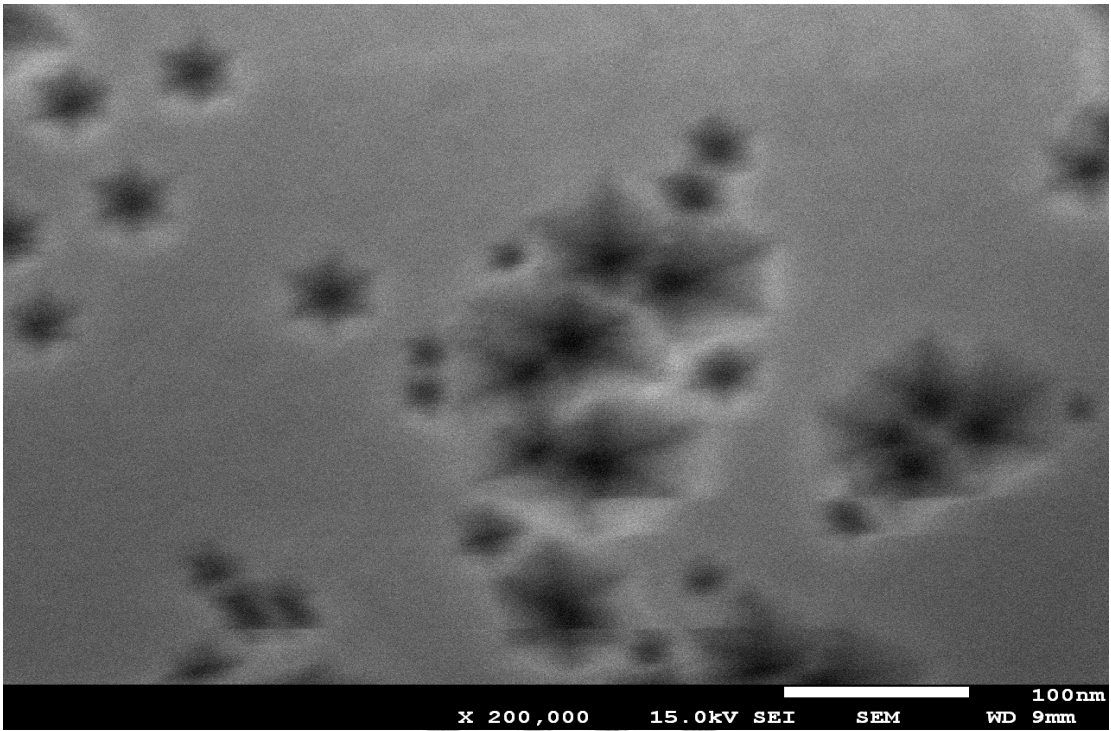


Fig. 3.4.6(a) Plane-view SEM image of DH 25 nm.

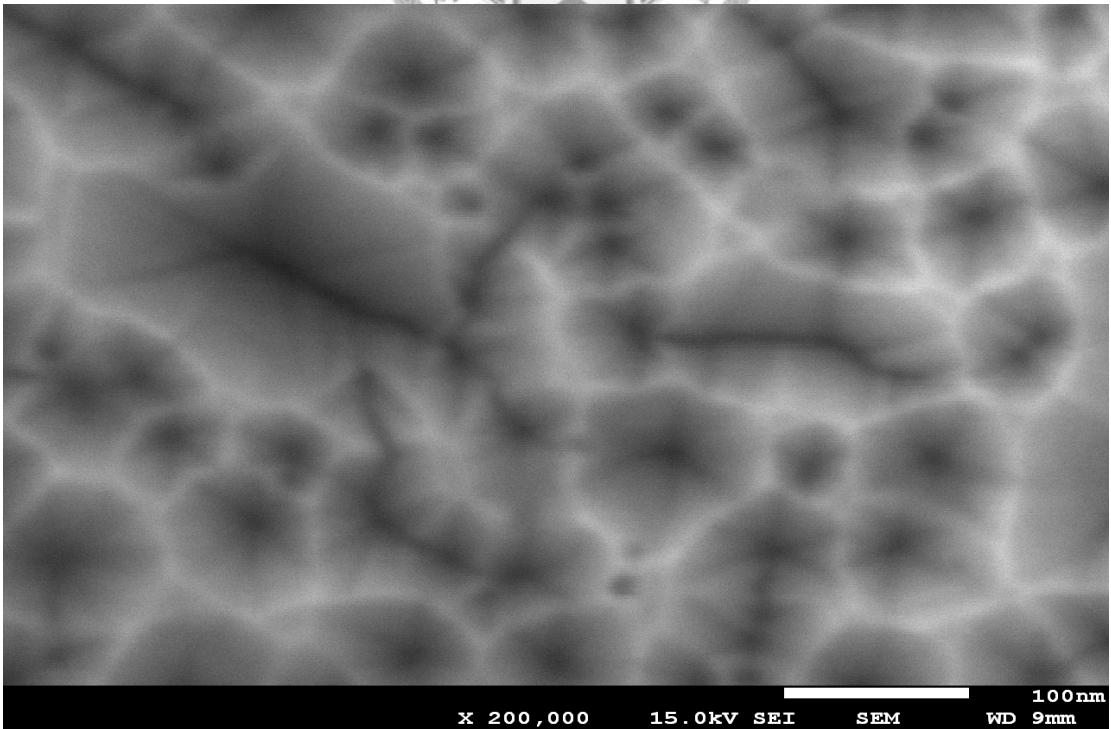


Fig. 3.4.6(b) Plane-view SEM image of DH 50 nm.

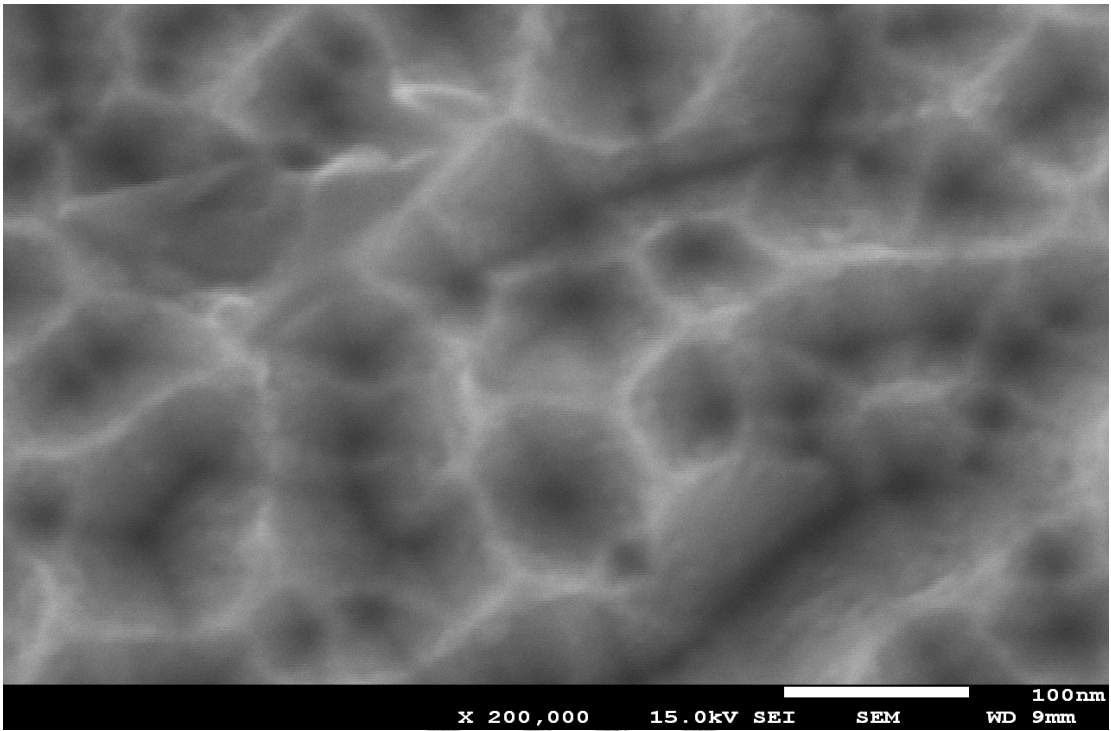


Fig. 3.4.6(c) Plane-view SEM image of DH 100 nm.

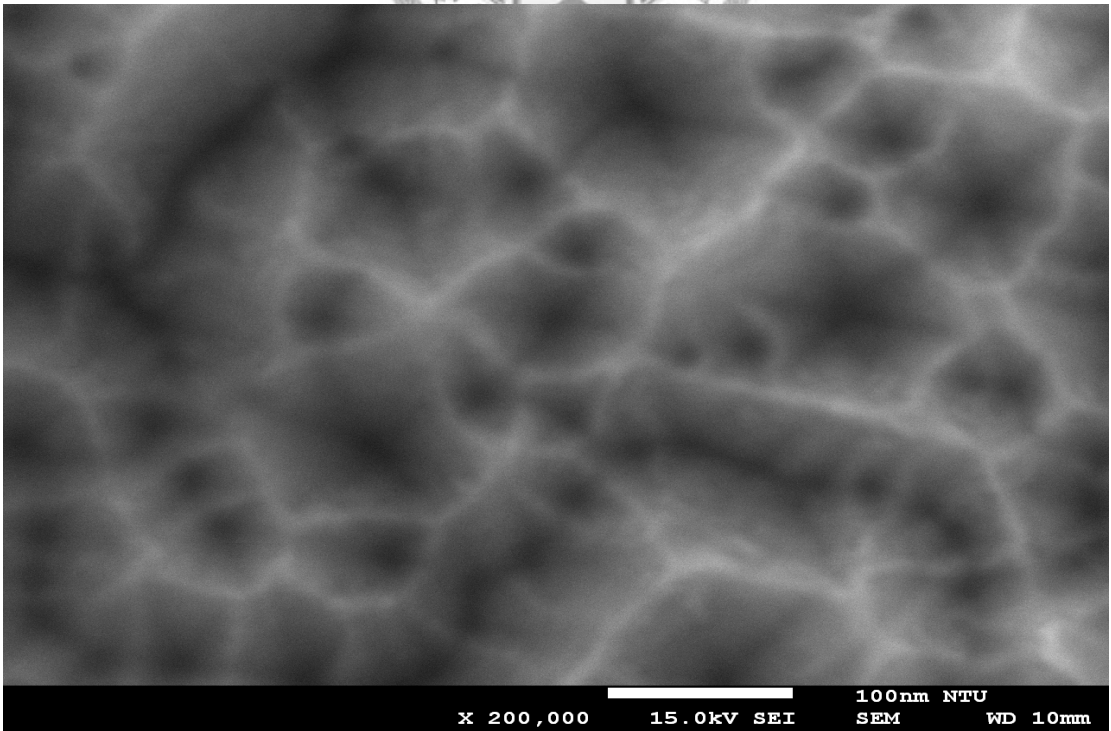


Fig. 3.4.6(d) Plane-view SEM image of DH 200 nm.

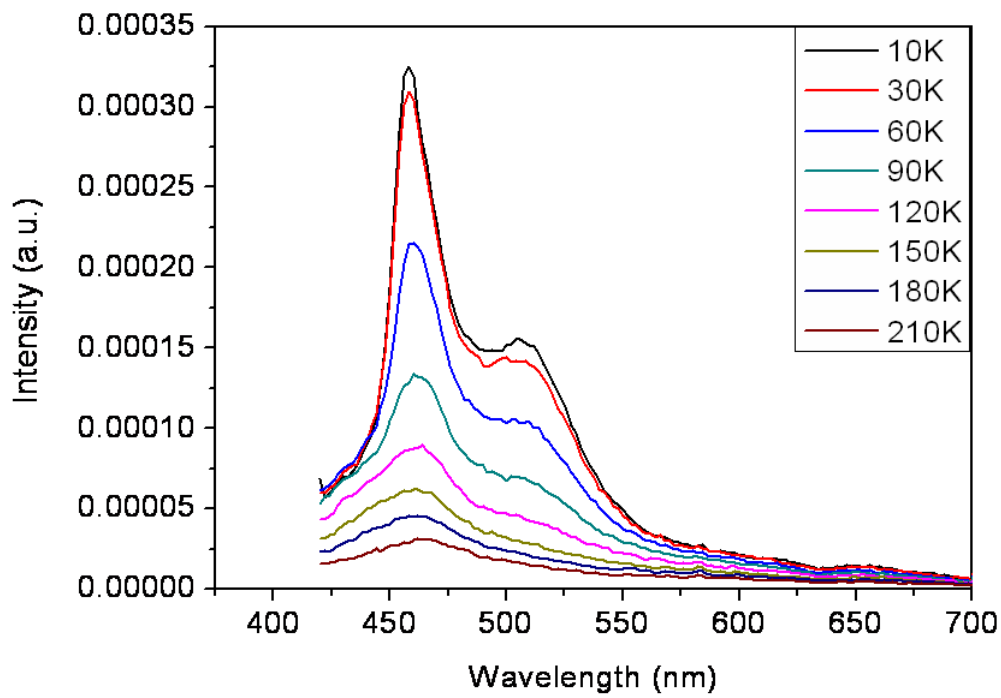


Fig. 3.4.7(a) PL spectra of sample DH 200 nm with excitation from the top.

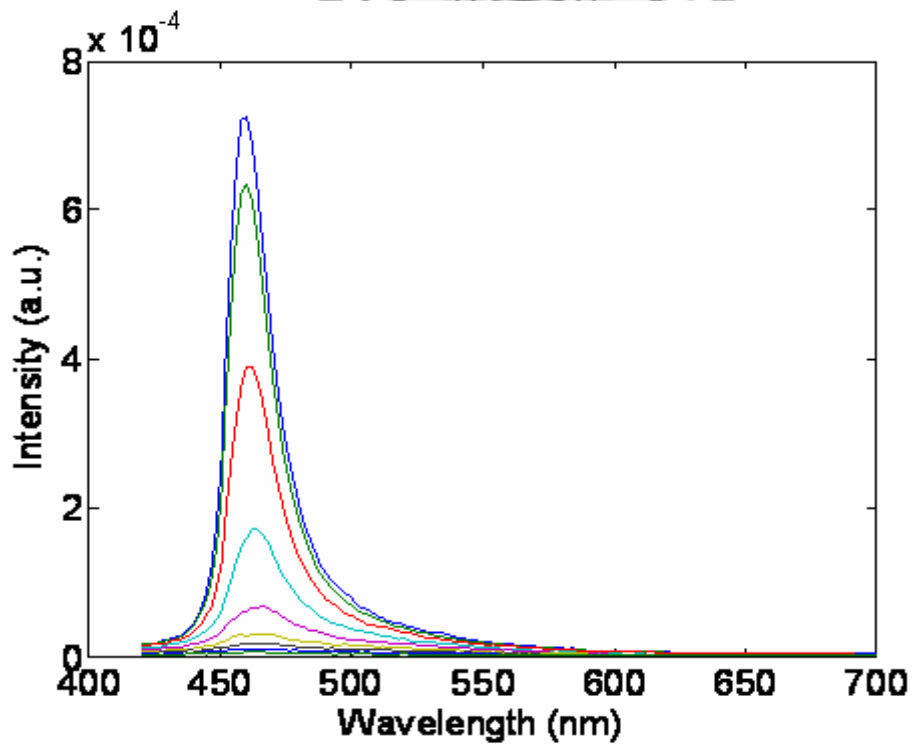


Fig. 3.4.7(b) PL spectra of sample DH 200 nm with excitation from the bottom.

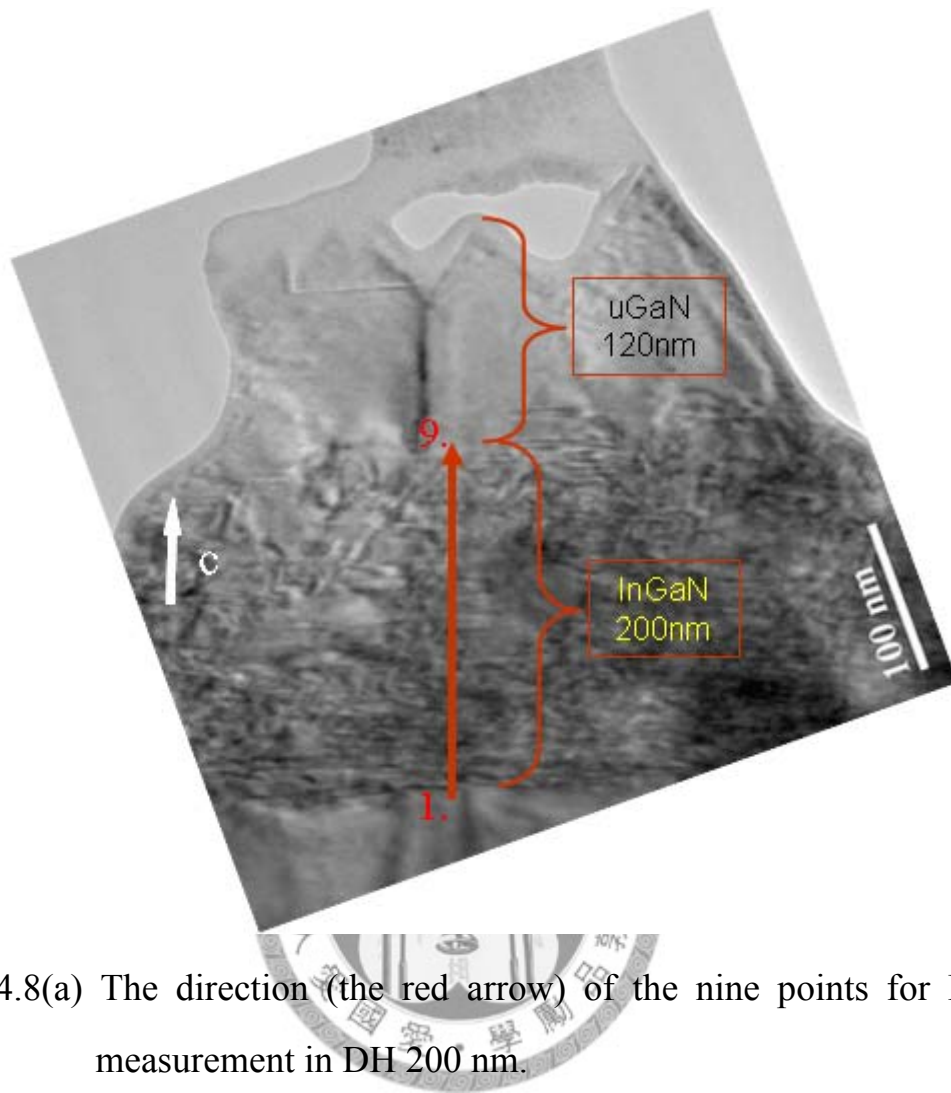


Fig. 3.4.8(a) The direction (the red arrow) of the nine points for EDX measurement in DH 200 nm.

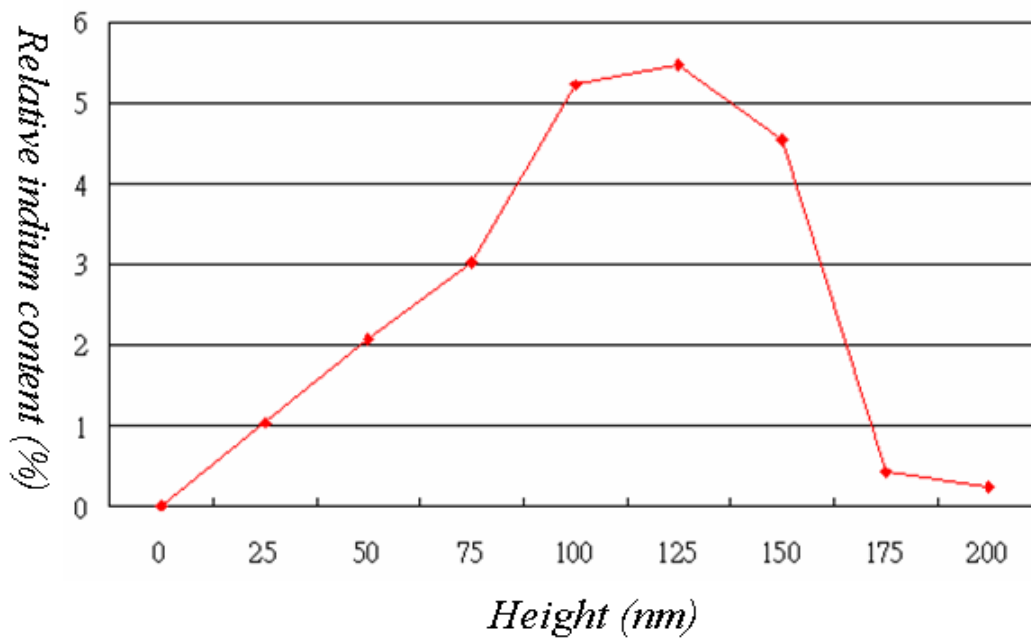


Fig. 3.4.8(b) The trend of the relative indium content of DH 200 nm.

Chapter 4

Comparison between InGaN/GaN Multi-layer Samples under Different Growth Conditions

In this chapter, we will compare the nanostructures and optical properties of two InGaN/GaN multi-layer samples of different growth conditions (named as 10nm-5P and 8nm-6P hereafter). The main differences in structure between the two samples are the thicknesses of the InGaN layer and GaN barrier and the number of periods.

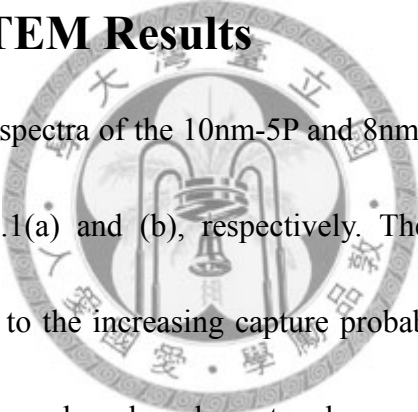
4.1 Sample Growth and Measurement Conditions

Both samples were grown by metalorganic chemical vapor deposition (MOCVD). The 10nm-5P (10nm wells, 5 periods) and 8nm-6P (8nm wells, 6 periods) samples were prepared in the following manner. First, a 2~3 μm undoped-GaN layer was grown on a (0001) *c*-plane sapphire substrate at 1080 °C. Then, the multi-layer wells were grown. The InGaN wells of the 10nm-5P (8nm-6P) samples were grown at 675 °C. The growth temperature was then ramped to 800 °C for depositing GaN barriers of 15 nm (20 nm) in thickness. A 15 nm (20 nm) GaN caplayer was deposited at 800 °C after the multi-layer wells. The detailed structures of these two samples are shown in Fig. 4.1.1.

Temperature-dependent PL measurements for the effective band gaps of these two

samples by using a 35mW He-Cd (325 nm) laser for excitation were performed. HRTEM measurements under two-beam condition were performed to observe the indium distribution within the InGaN wells of these two samples. EDX was measured to obtain the elemental distribution in the horizontal and vertical direction in each InGaN layer. Strain state analysis (SSA) results provide more local information about a well, such as average indium content and indium composition fluctuation.

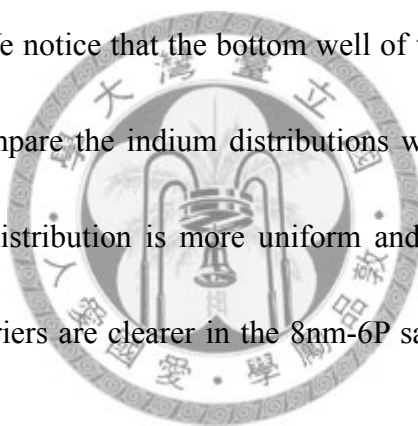
4.2 PL and HRTEM Results



Low-temperature PL spectra of the 10nm-5P and 8nm-6P samples from 13 to 300 K are shown in Figs. 4.2.1(a) and (b), respectively. The PL intensities drop with increasing temperature due to the increasing capture probability of carriers by defects. The 10nm-5P sample shows a broad peak centered around 535 nm with no distinct individual peaks within. One can clearly observe two spectral peaks in the 8nm-6P sample. The long-wavelength spectral peak location of the 8nm-6P sample was also centered around 535 nm. The short-wavelength spectral peak red-shifts from 442 nm to 458 nm as the temperature rises from 30 to 300K for the 8nm-6P sample.

HRTEM images are needed for understanding the indium distributions among the InGaN well layers to see the nano-structure differences leading to the variations in the PL spectras. Low-magnification cross-section HRTEM images of the 10nm-5P and

8nm-6P samples are shown in Fig. 4.2.2. Here, we can see the general structures of the two samples, including the InGaN well and GaN barrier. The white arrow indicates the direction of (0001) from the substrate. The G1 glue can be seen at the very top. In general, the variations of the contrast in the HRTEM images represent the indium composition fluctuations. HRTEM images of higher magnification of the first through fifth wells from the bottom of the 8nm-6P and 10nm-5P samples are shown in Figs. 4.2.3(a) and (b) through 4.2.7(a) and (b), respectively. One can observe nano-scale clusters in these images. We notice that the bottom well of the 8nm-6P sample have the best quality. Then, we compare the indium distributions within the five InGaN wells. We find that the indium distribution is more uniform and the interfaces between the InGaN wells and GaN barriers are clearer in the 8nm-6P sample, when compared with the 10nm-5P sample.



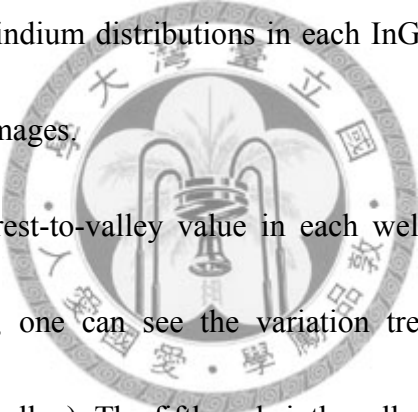
4.3 EDX and SSA Results

EDX is used to estimate indium distribution in the horizontal and vertical directions of each InGaN layer. The indium distribution of the horizontal (red arrow) and vertical directions (yellow arrow) measured by EDX in 10nm-5P and 8nm-6P samples are shown in Figs. 4.3.1(a) and (b), respectively. The white arrow indicates the direction of (0001) from the substrate. The data at these points are used to draw a

diagram for comparing the relative indium contents as functions of distance. The trend of the relative indium content along the horizontal direction in each InGaN layer of the 10nm-5P and 8nm-6P samples are shown in Figs. 4.3.2(a) and (b), respectively. The nearest left point along the arrow of the InGaN layer is labeled as 0 nm in distance. Then, we average the relative indium contents at these points along the horizontal direction of each layer to obtain the average indium content of each InGaN layer. The variation of the average indium content along the vertical direction of the 10nm-5P and 8nm-6P samples are shown in Figs. 4.3.3(a) and (b), respectively. We also calculate the standard deviation at these points in each point array (as shown in Figs. 4.3.2 and 4.3.3). In the horizontal direction, we find that the indium composition fluctuation is stronger in the 10nm-5P sample, when compared with the 8nm-6P sample. In the vertical direction, we find that the 8nm-6P sample has a more uniform indium composition in each layer, when compared with the 10nm-5P sample.

For more detail investigation, we used a package program called the DALI (Digital Analysis of Lattice Images) to analyze the two-beam images of the InGaN layers and obtain the SSA images for the composition mapping of the InGaN layers. SSA can exclude some uncertain factors, such as thickness, defocus, and strain relaxation. In such SSA images, the deep blue color represents GaN and the red color corresponds to a d value larger than 1.1 or indium content higher than 21 %. The five

InGaN layers of the 10nm-5P sample are shown in Figs. 4.3.4(a) through (e). The color coding for various d-factor values are shown below the image in Fig. 4.3.4(a). In this image, one can see that the layer shape can still be identified although a cluster exists and indium atoms out-diffuse into the upper barrier. The horizontal and vertical line-scan profiles show that the local indium composition inside the cluster can be as large as 23.1%. The six InGaN layers of the 8nm-6P sample are shown in Figs. 4.3.5(a) through 4.3.5(f). As indicated with the line-scan results, the relatively constant indium content and more uniform indium distributions in each InGaN well of the 8nm-6P can also be seen in these SSA images.



We calculate the crest-to-valley value in each well of samples 10nm-5P and 8nm-6P. From the results, one can see the variation trend of indium composition fluctuation range (crest-to-valley). The fifth and sixth wells from the bottom in samples 10nm-5P and 8nm-6P have the largest composition fluctuation ranges, respectively. Other variation trends were shown in Table 4.3.1. We also evaluate the average indium content of each well in samples 10nm-5P and 8nm-6P by integrating the indium composition distribution in an SSA image and dividing by the designated InGaN well area. We assume that all the indium atoms distributed around a well in an SSA image belong to the InGaN well. The results of the average indium contents of those wells are listed in Table 4.3.2. These results are consistent with the EDX data.

4.4 Discussions

We have demonstrated the effective band gaps and indium distributions of InGaN/GaN multi-layers with different structures based on PL and HRTEM measurements. In HRTEM results, we found that the indium distribution was more uniform and the interfaces between InGaN wells and GaN barriers were clearer in the sample 8nm-6P, when compared with sample 10nm-5P. This might be why PL result did not show clear peaks in the sample 10nm-5P. PL measurement clearly showed two spectral peaks in the sample 8nm-6P. Those results implied higher optical quality in the sample 8nm-6P than in the sample 10nm-5P. In the other measurements, EDX and SSA results both showed that the sample 10nm-5P had a larger indium composition fluctuation than the sample 8nm-6P.

Based on the data and discussions above, one can conclude that the structure of the sample 8nm-6P has a better crystal quality when compared with the sample 10nm-5P. The only growth difference was that sample 8nm-6P had a thinner InGaN layer and thicker GaN barrier.

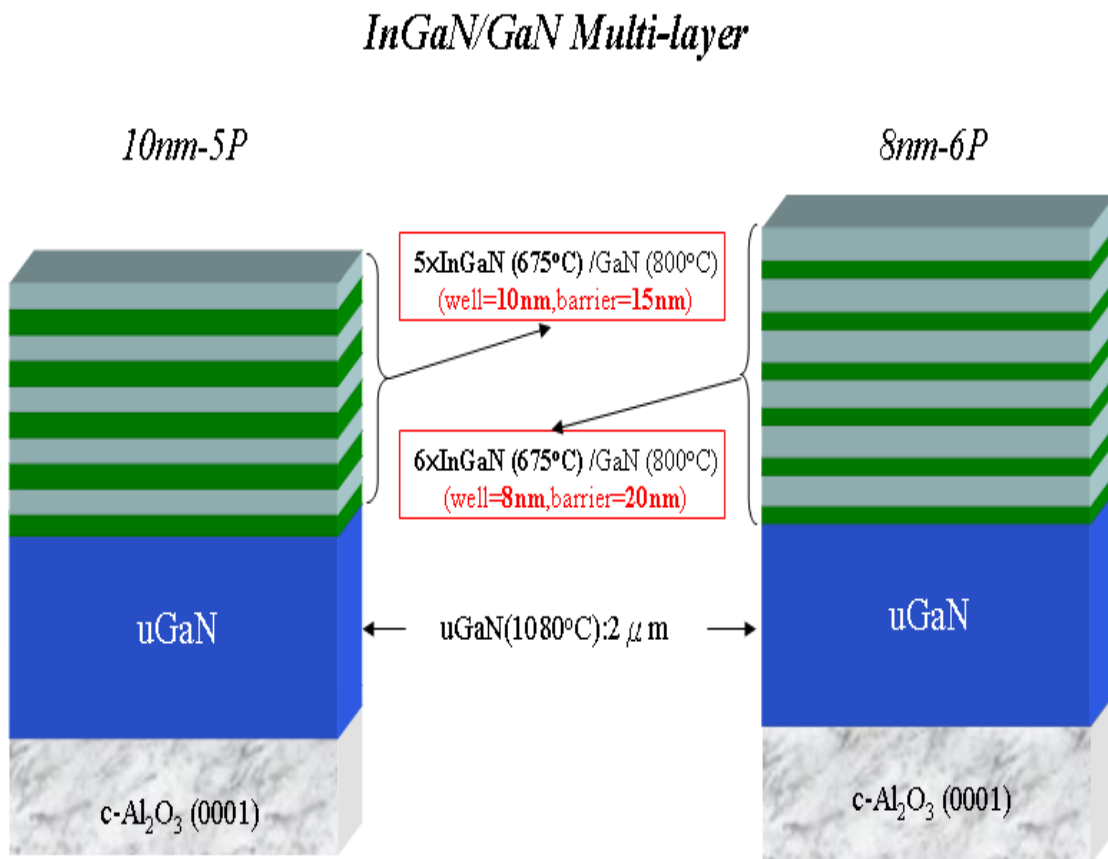


Fig. 4.1.1 Structures of InGaN/GaN multi-layer samples (10nm-5P and 8nm-6P).

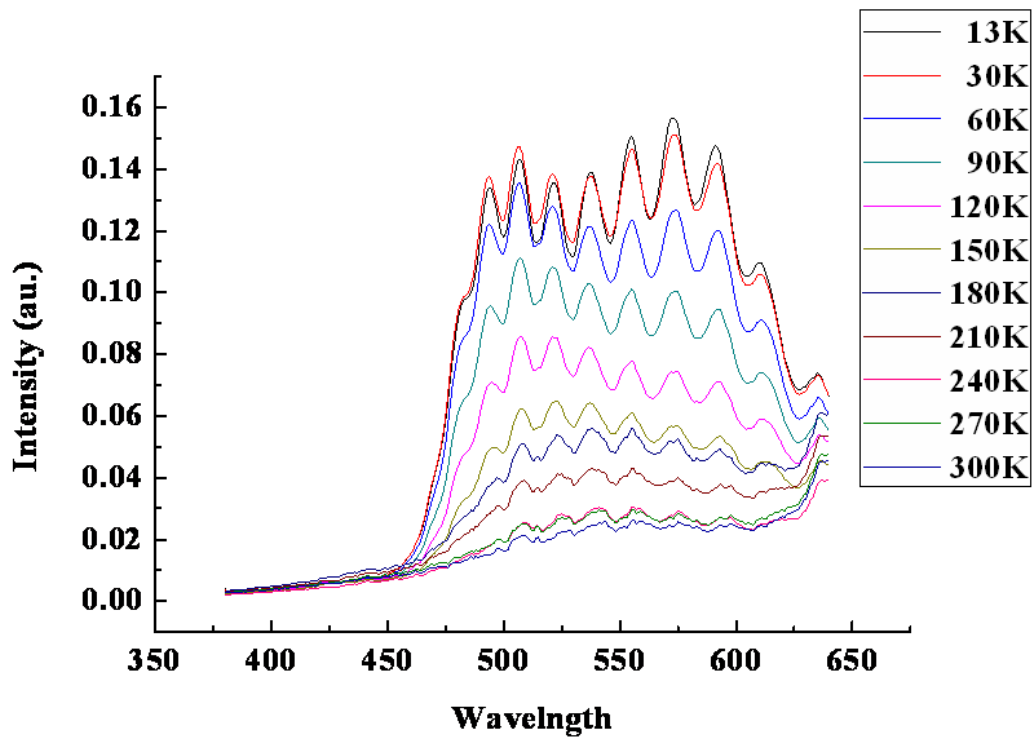


Fig. 4.2.1(a) PL spectra of sample 10nm-5P.

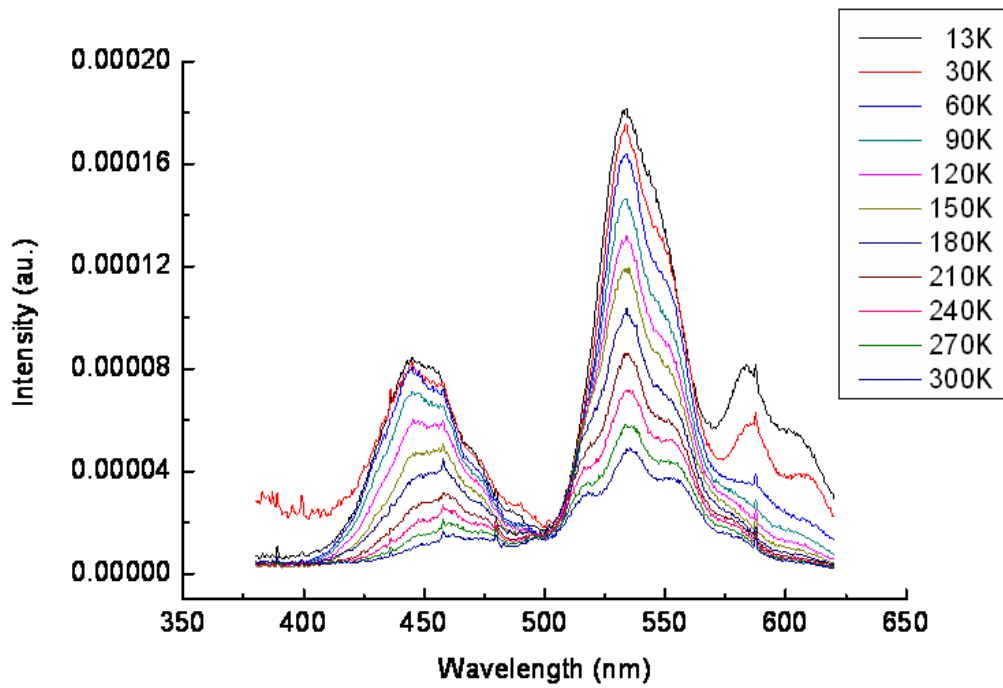


Fig. 4.2.1(b) PL spectra of sample 8nm-6P.

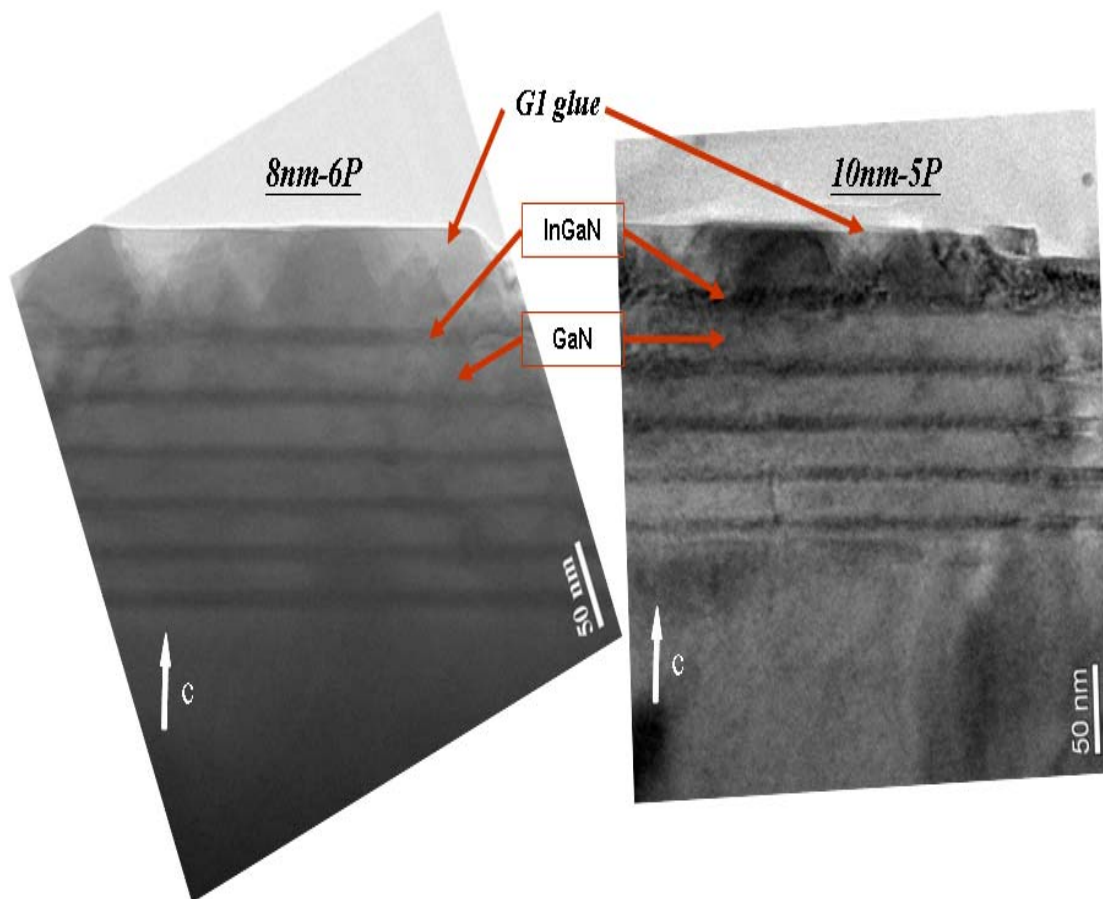
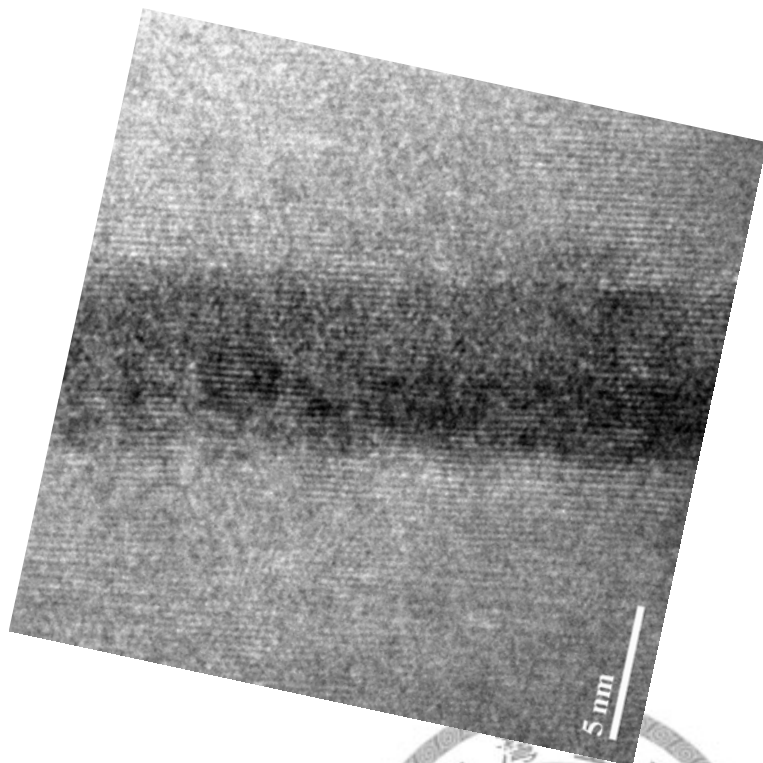
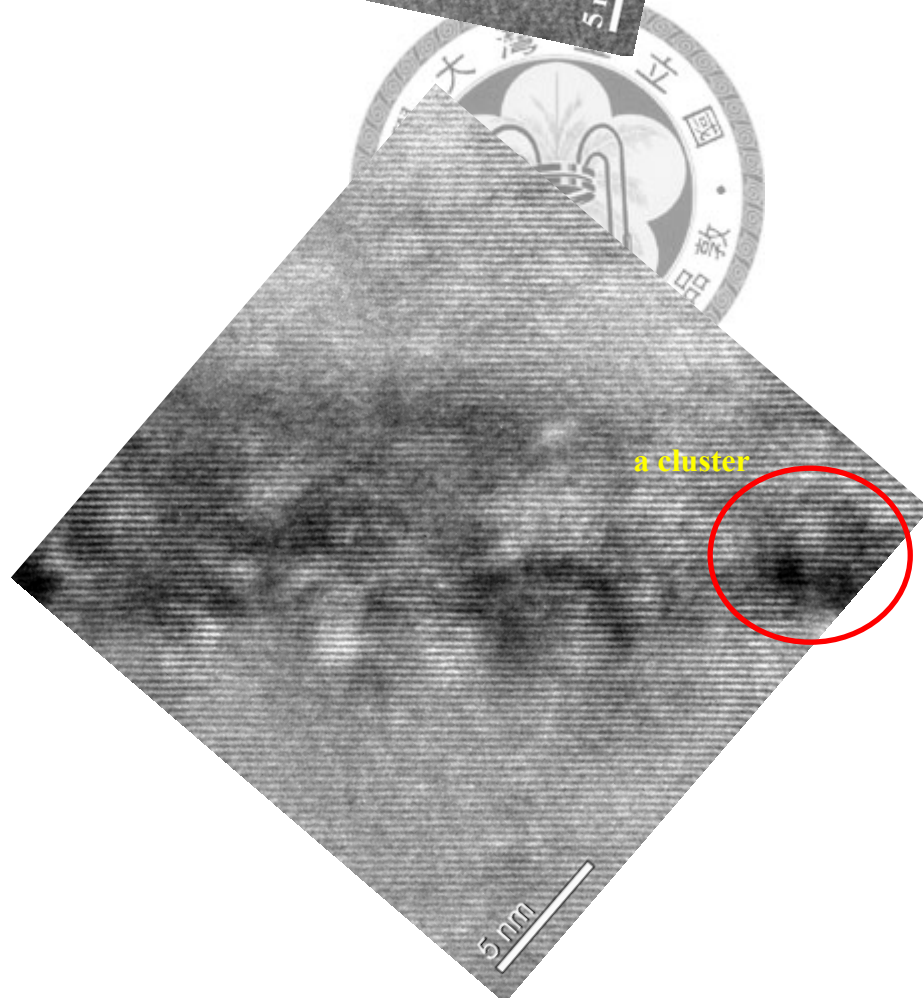


Fig. 4.2.2 Low-magnification cross-section HRTEM images of 10nm-5P and 8nm-6P.

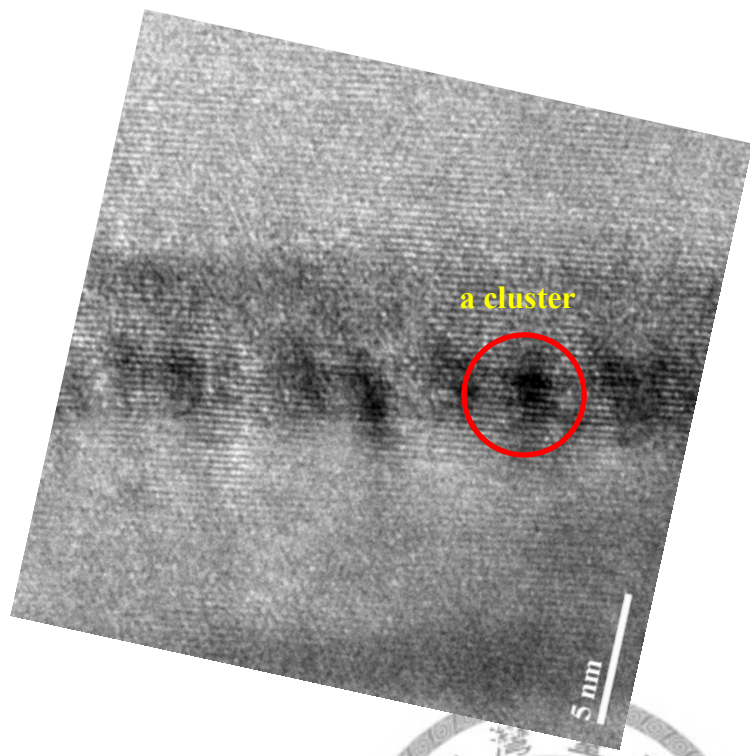


(a)

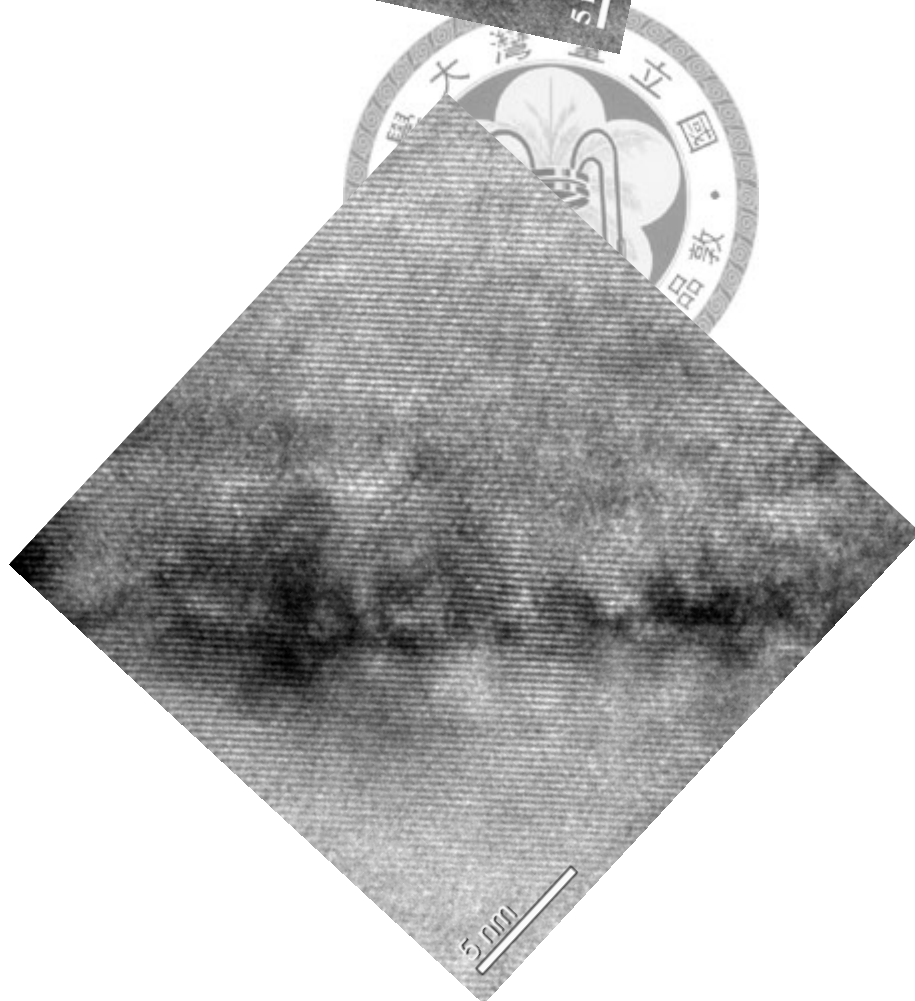


(b)

Fig. 4.2.3(a) and (b) HRTEM image of sample 8nm-6P and 10nm-5P, respectively (the first well from the bottom).

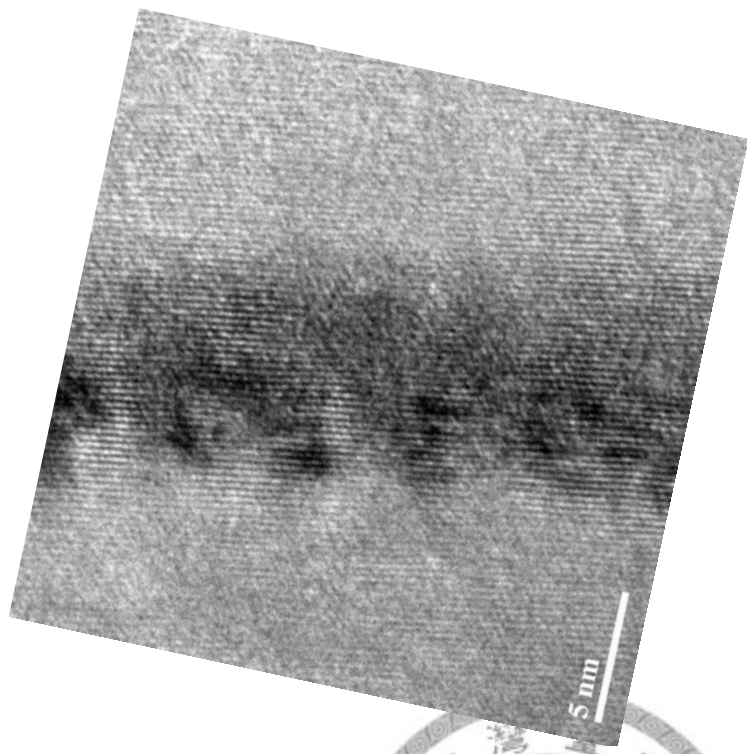


(a)

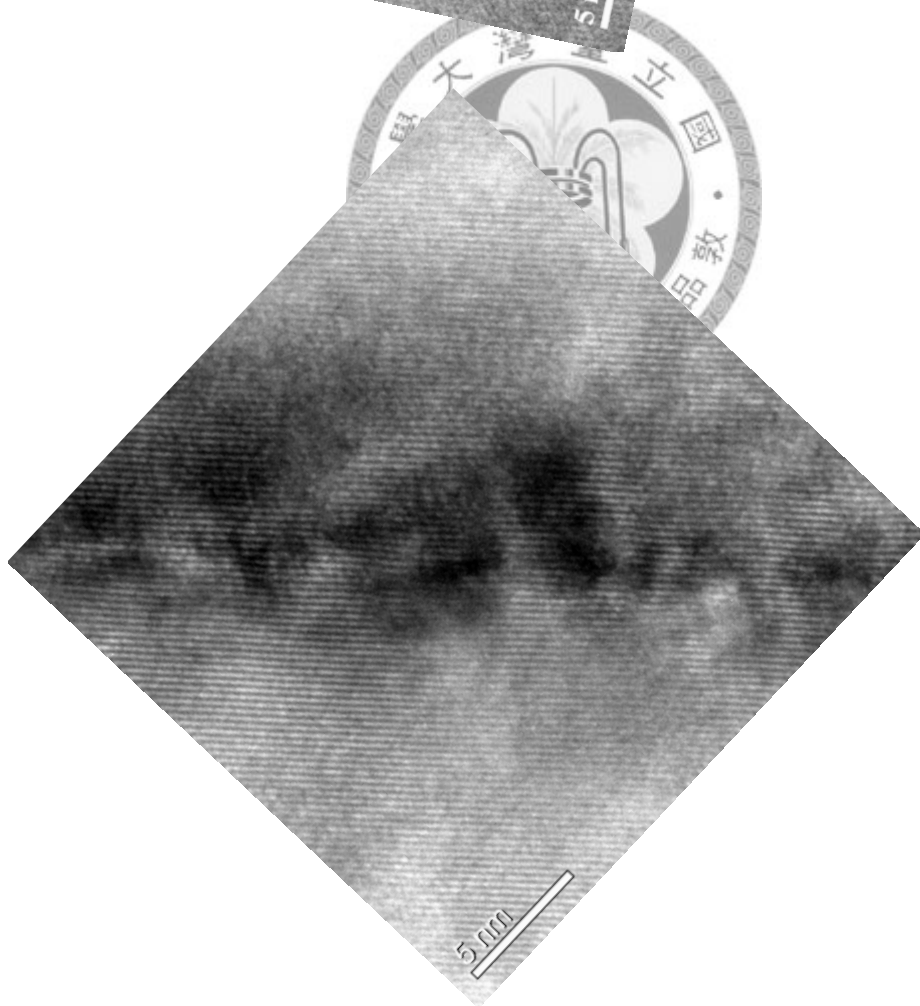


(b)

Fig. 4.2.4(a) and (b) HRTEM image of sample 8nm-6P and 10nm-5P, respectively (the second well from the bottom).

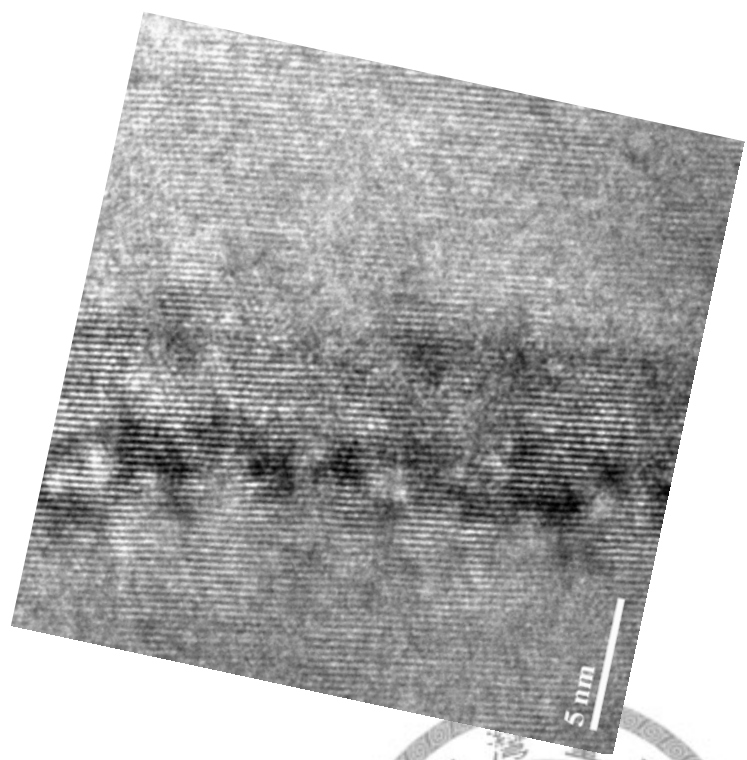


(a)

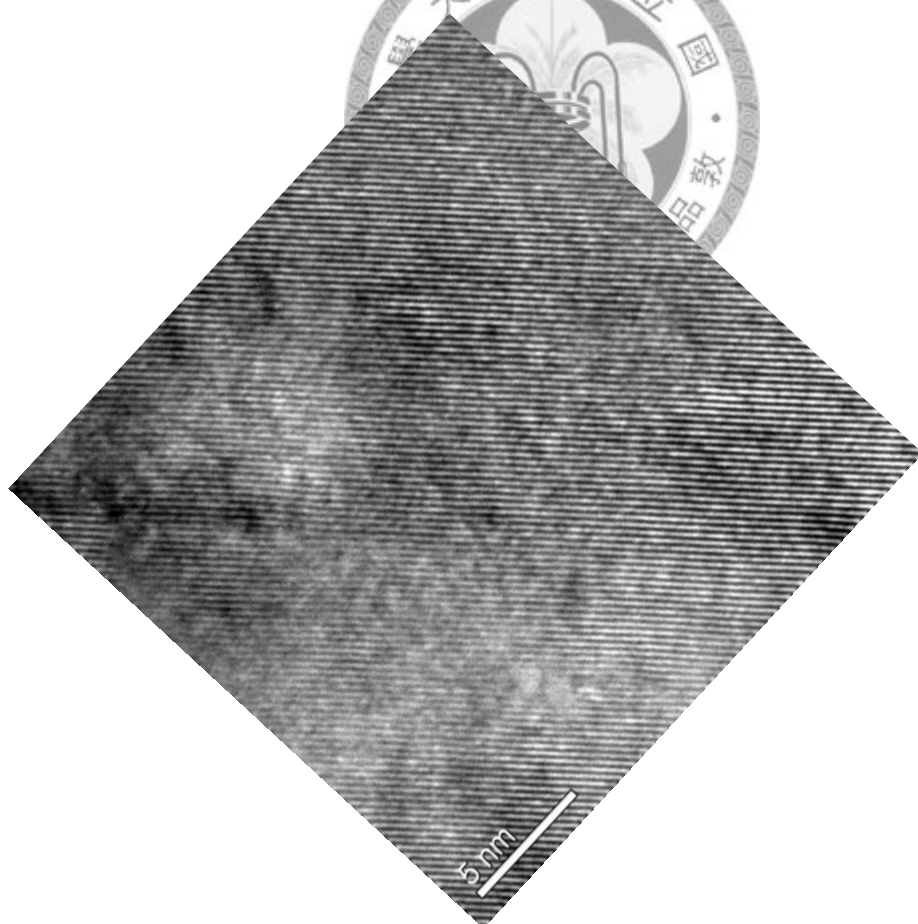


(b)

Fig. 4.2.5(a) and (b) HRTEM image of sample 8nm-6P and 10nm-5P, respectively (the third well from the bottom).

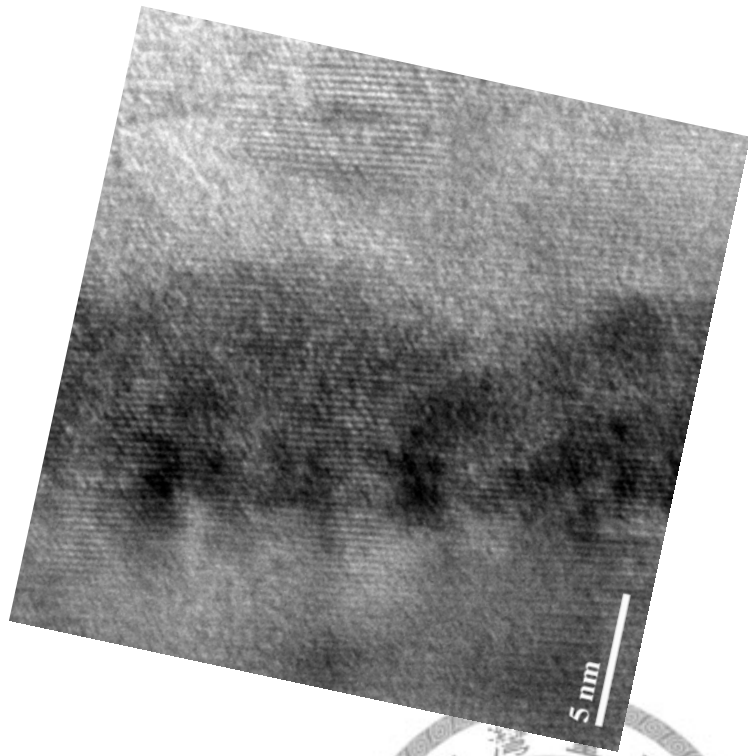


(a)

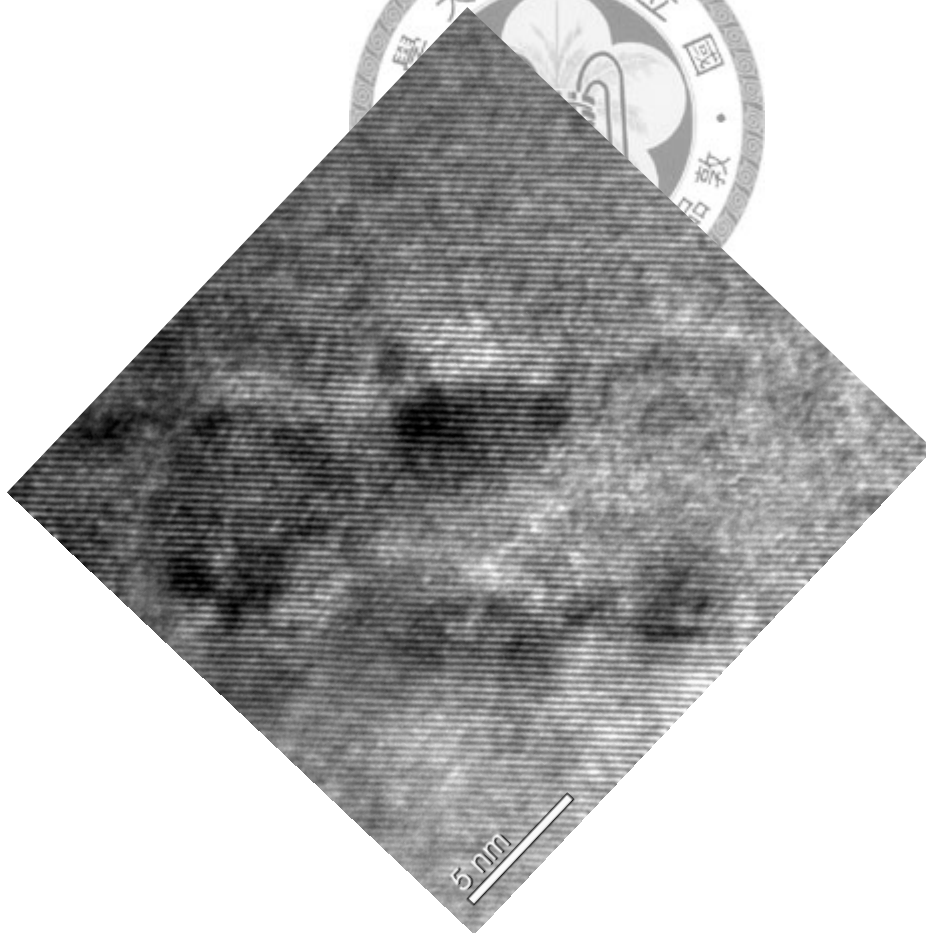


(b)

Fig. 4.2.6(a) and (b) HRTEM image of sample 8nm-6P and 10nm-5P, respectively (the fourth well from the bottom).



(a)



(b)

Fig. 4.2.7(a) and (b) HRTEM image of sample 8nm-6P and 10nm-5P, respectively (the fifth well from the bottom).

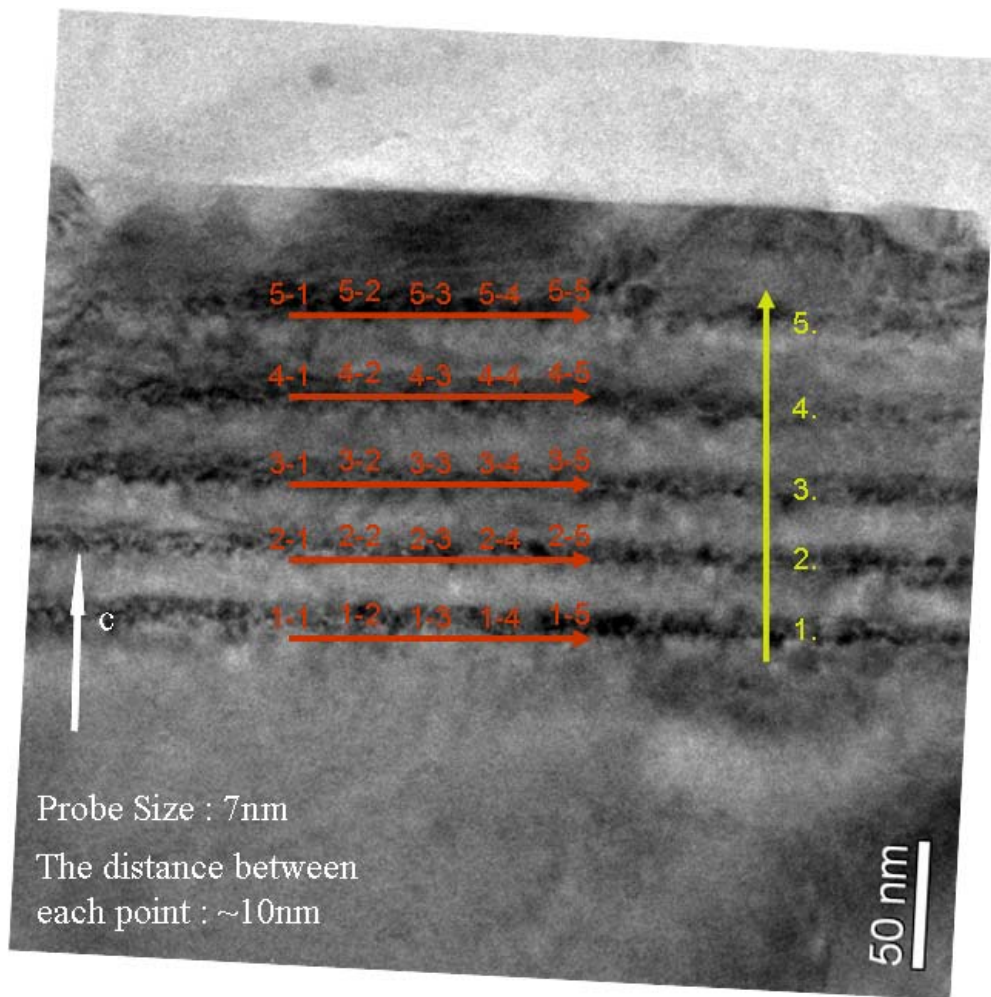


Fig. 4.3.1(a) The indium distribution of horizontal (red arrow) and vertical direction (yellow arrow) as measured by EDX in 10nm-5P.

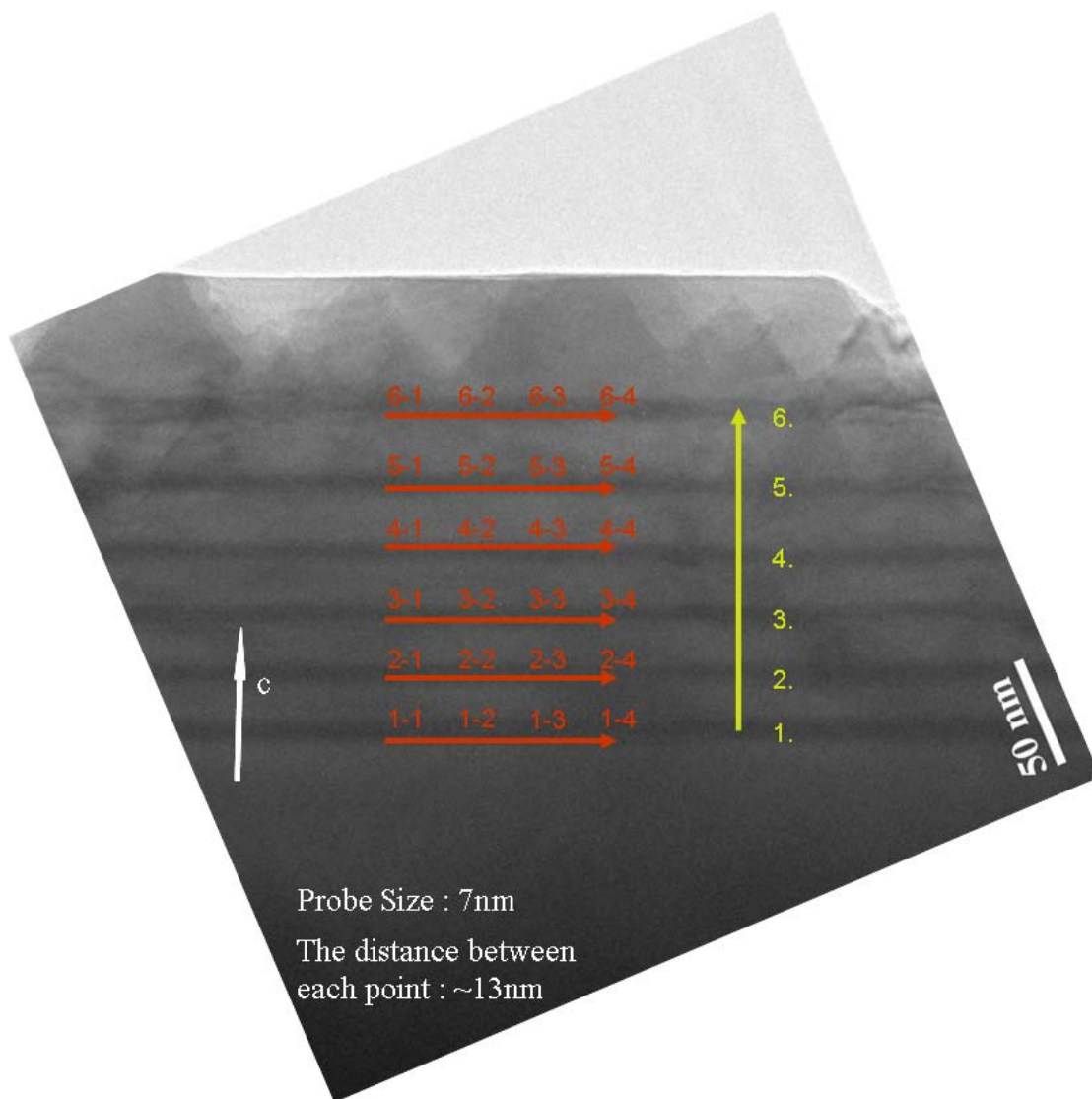


Fig. 4.3.1(b) The indium distribution of horizontal (red arrow) and vertical direction (yellow arrow) as measured by EDX in 8nm-6P.

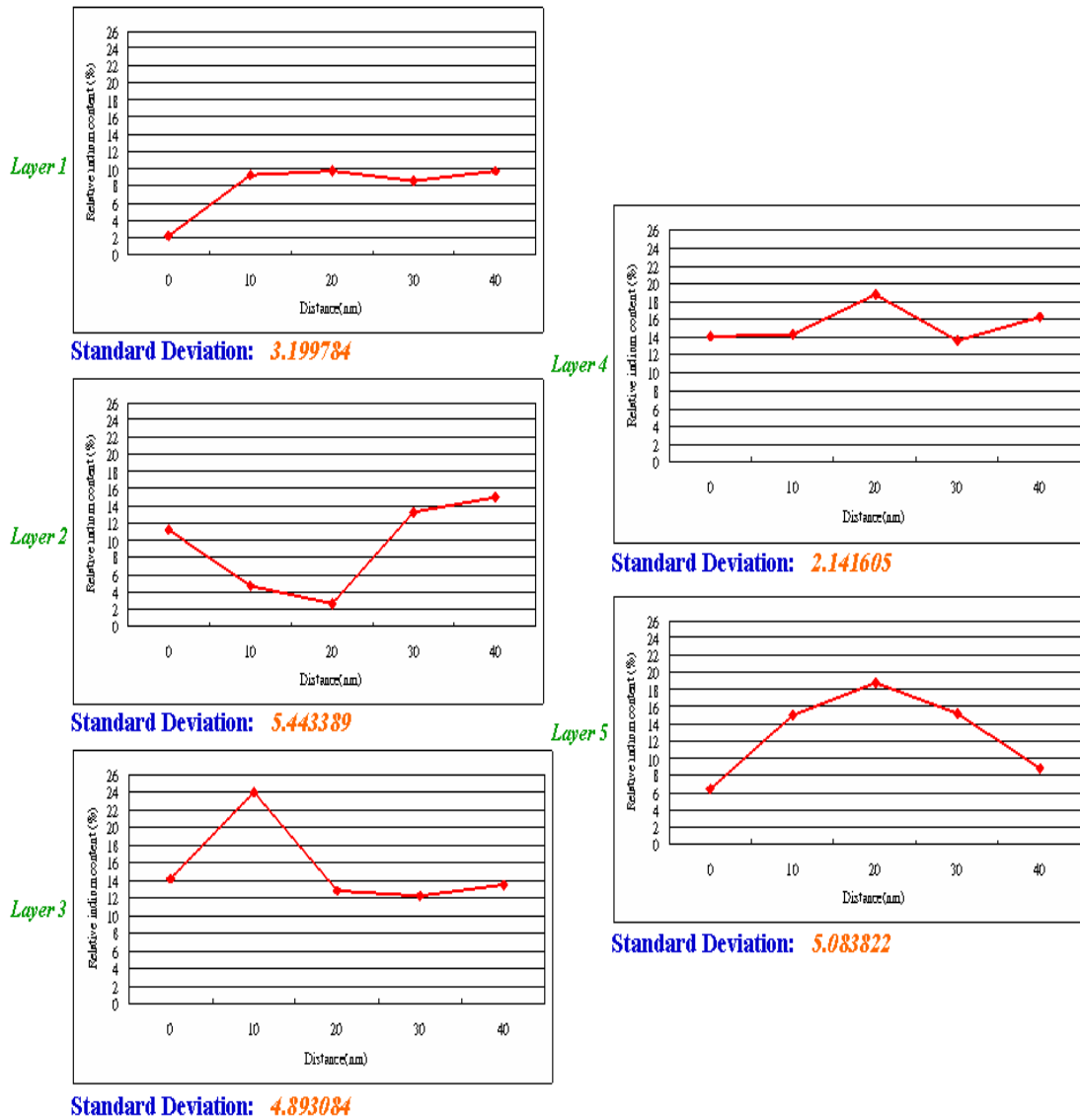


Fig. 4.3.2(a) Trend of the relative indium content along the horizontal direction in each InGaN layer of 10nm-5P.

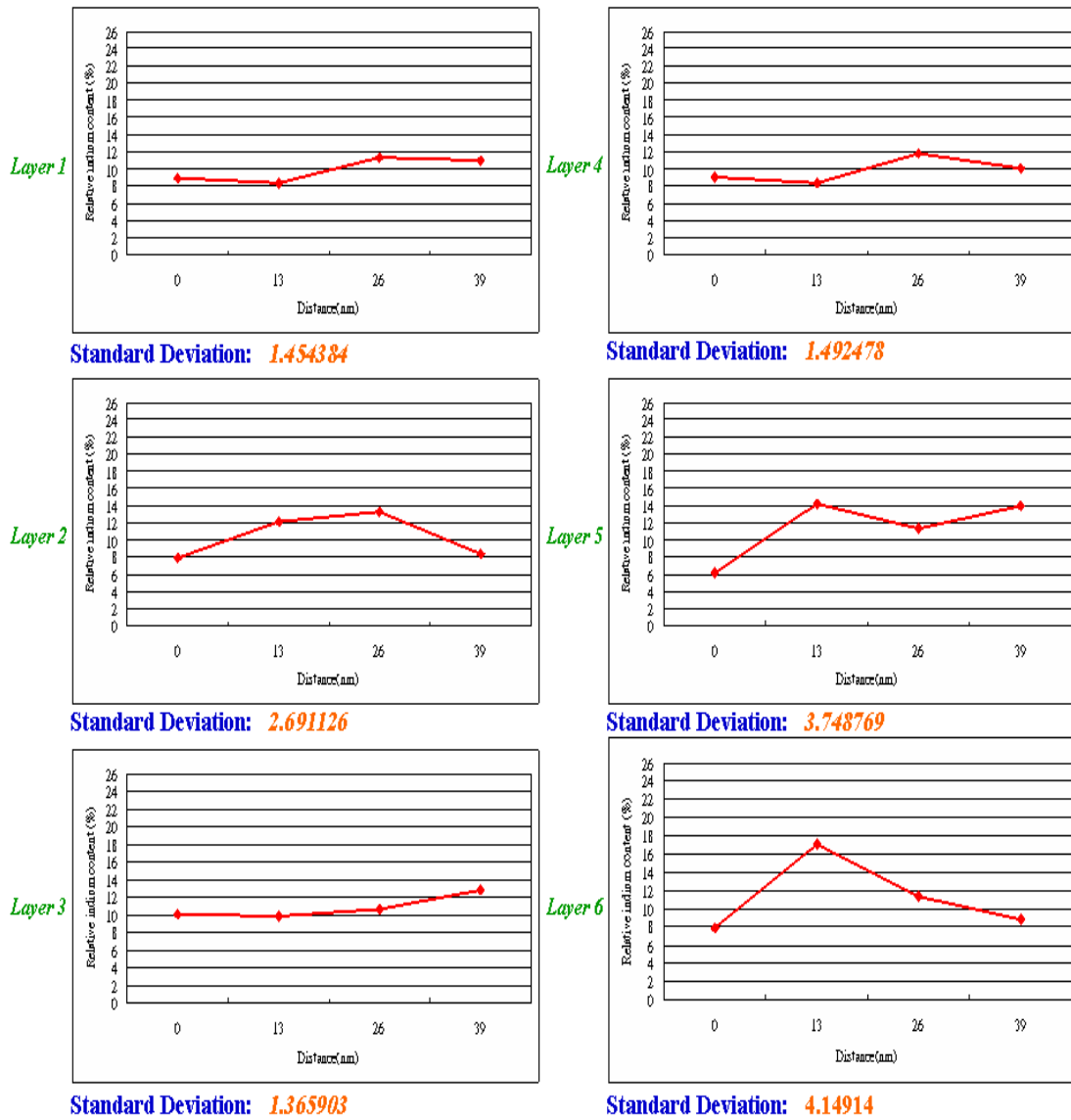


Fig. 4.3.2(b) Trend of the relative indium content along the horizontal direction in each InGaN layer of 8nm-6P.

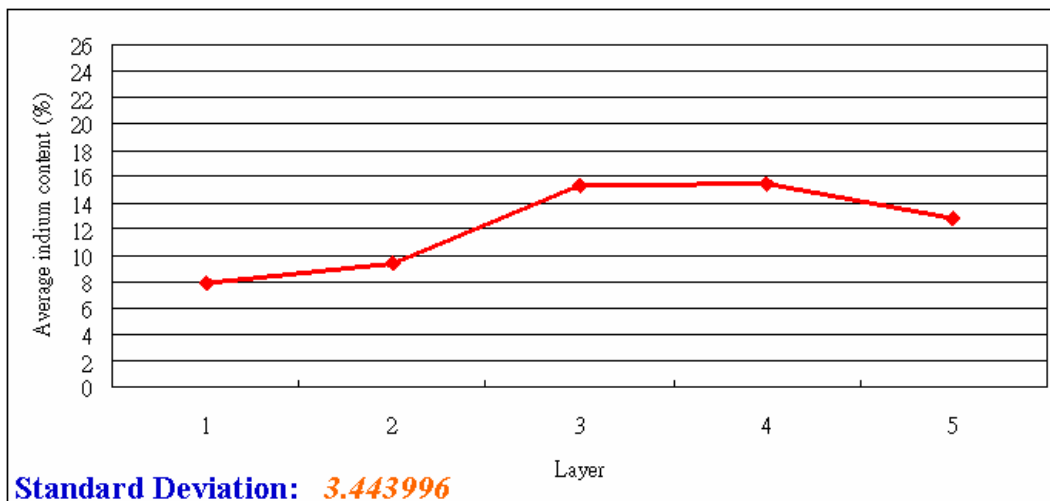


Fig. 4.3.3(a) Trend of the average indium content along the vertical direction of 10nm-5P.

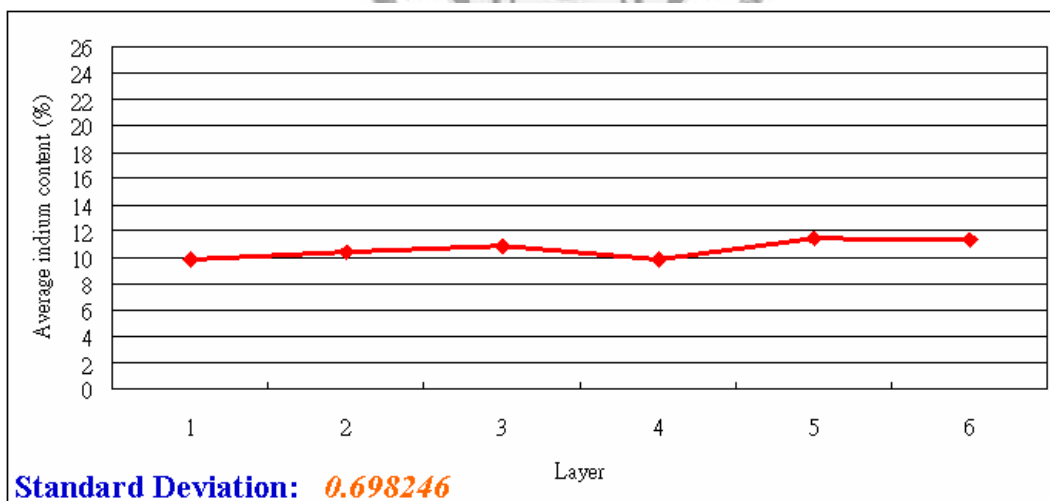
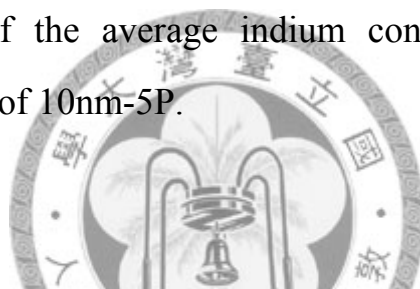


Fig. 4.3.3(b) Trend of the average indium content along the vertical direction of 8nm-6P.

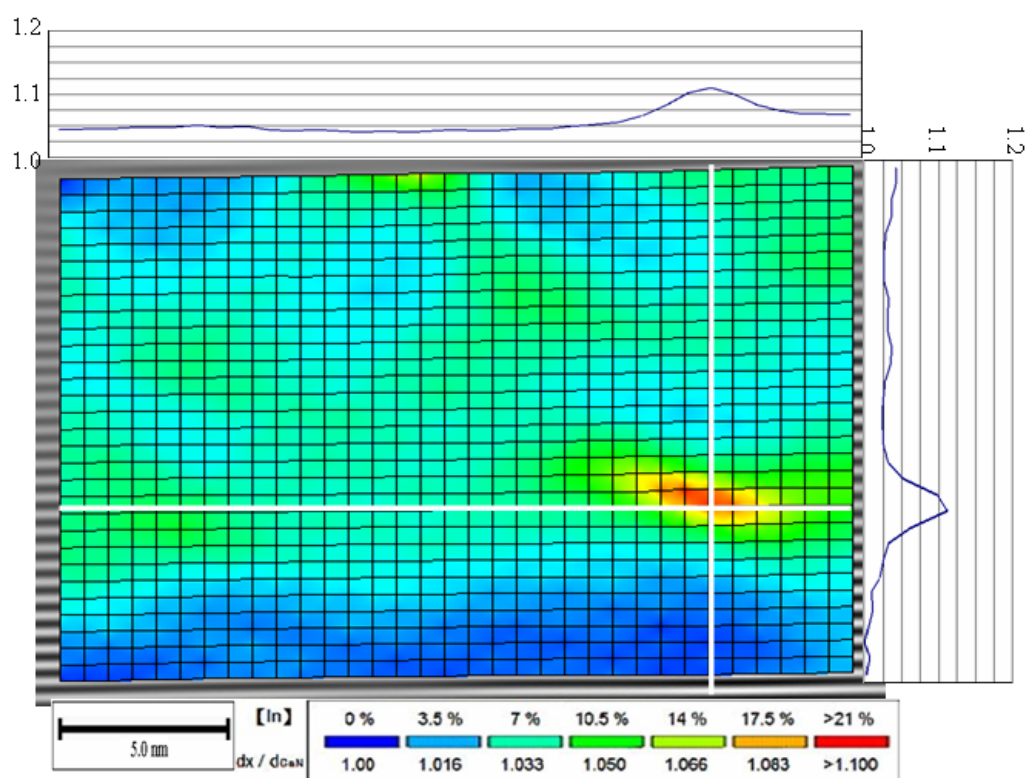


Fig. 4.3.4(a) An SSA image of 10nm-5P (the first well from the bottom).

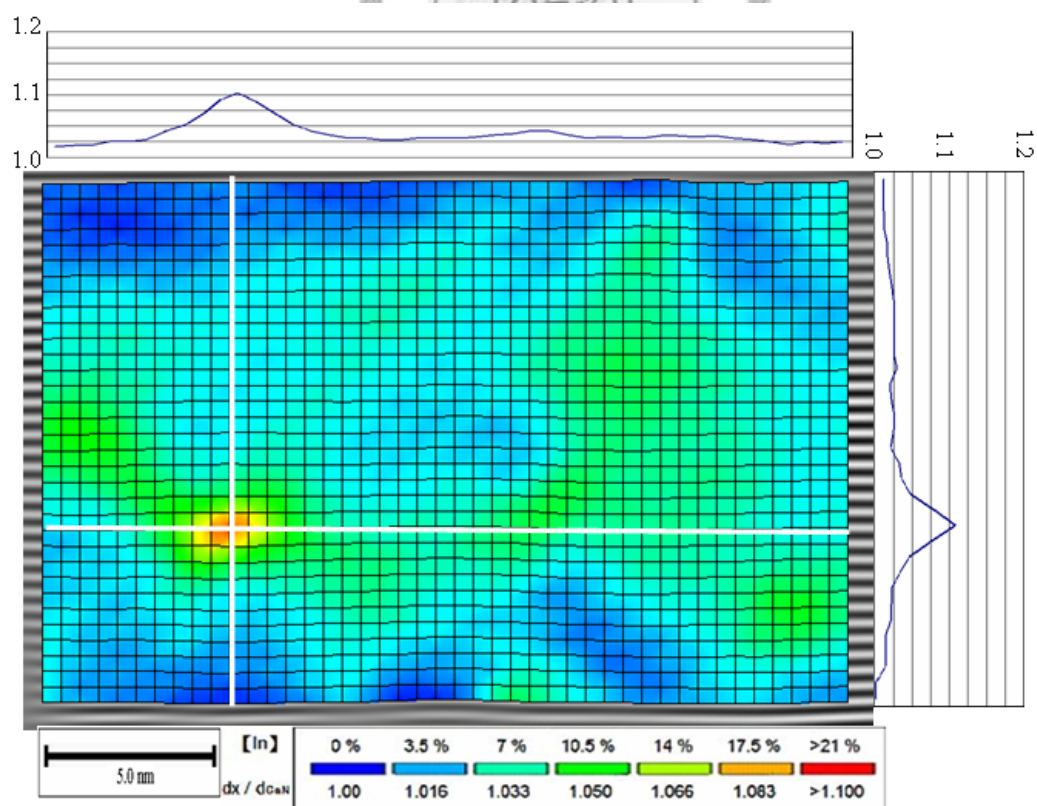


Fig. 4.3.4(b) An SSA image of 10nm-5P (the second well from the bottom).

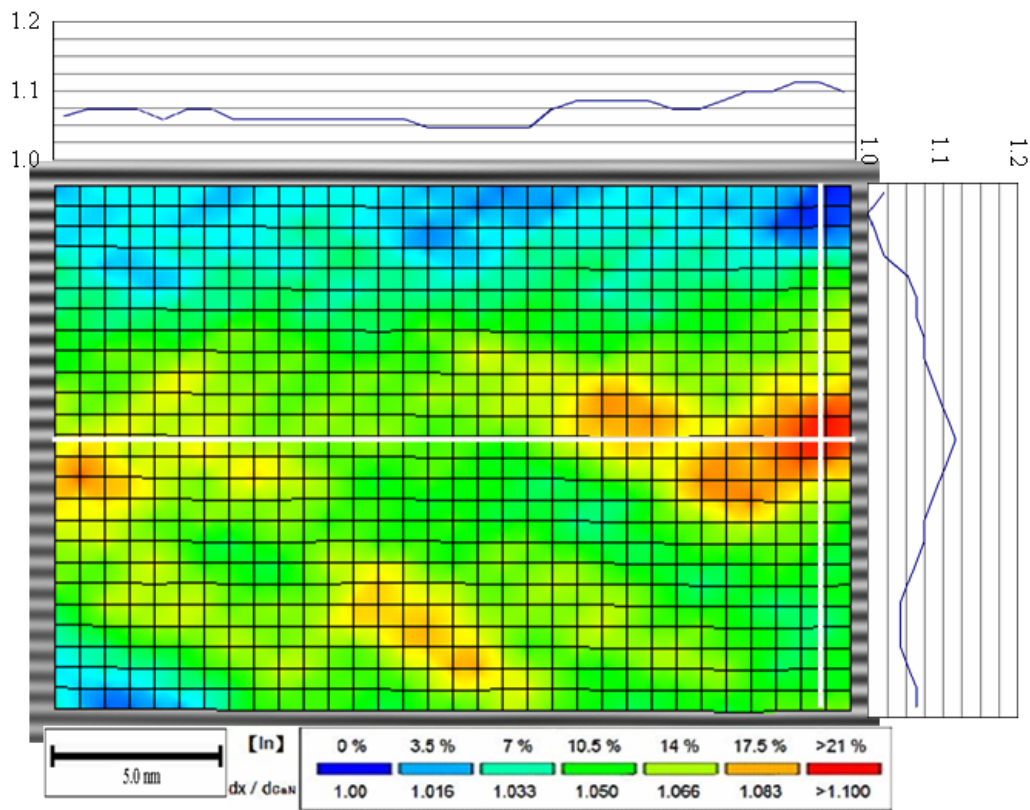


Fig. 4.3.4(c) An SSA image of 10nm-5P (the third well from the bottom).

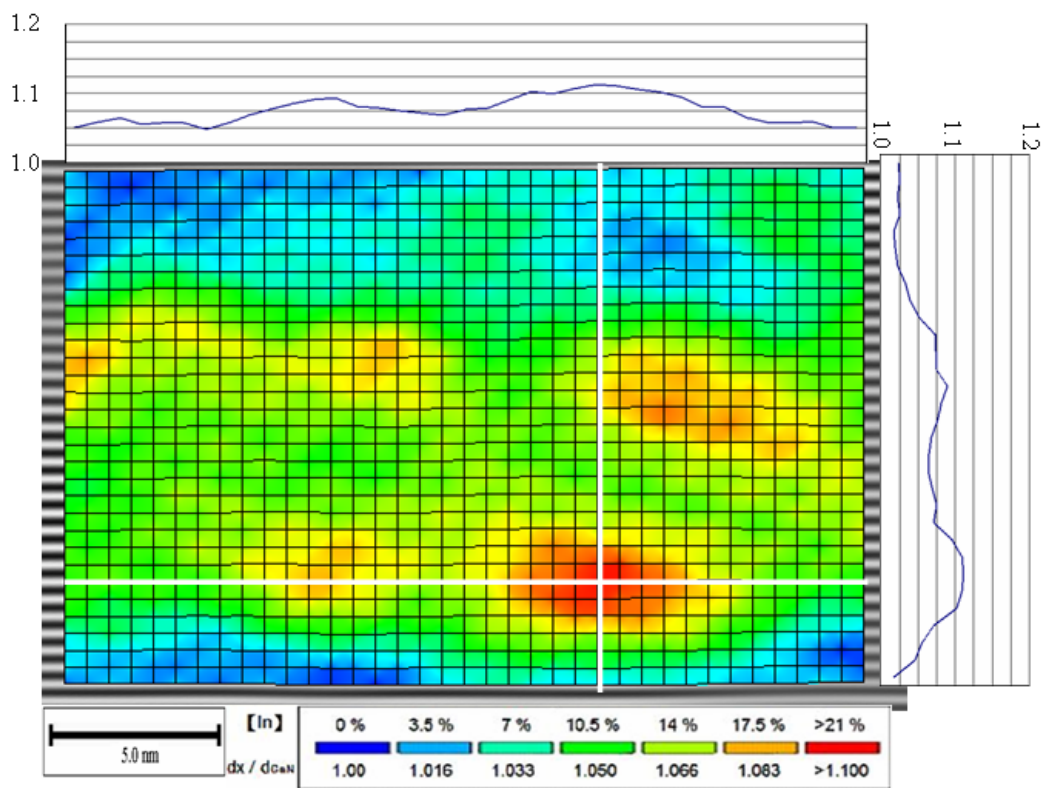


Fig. 4.3.4(d) An SSA image of 10nm-5P (the fourth well from the bottom).

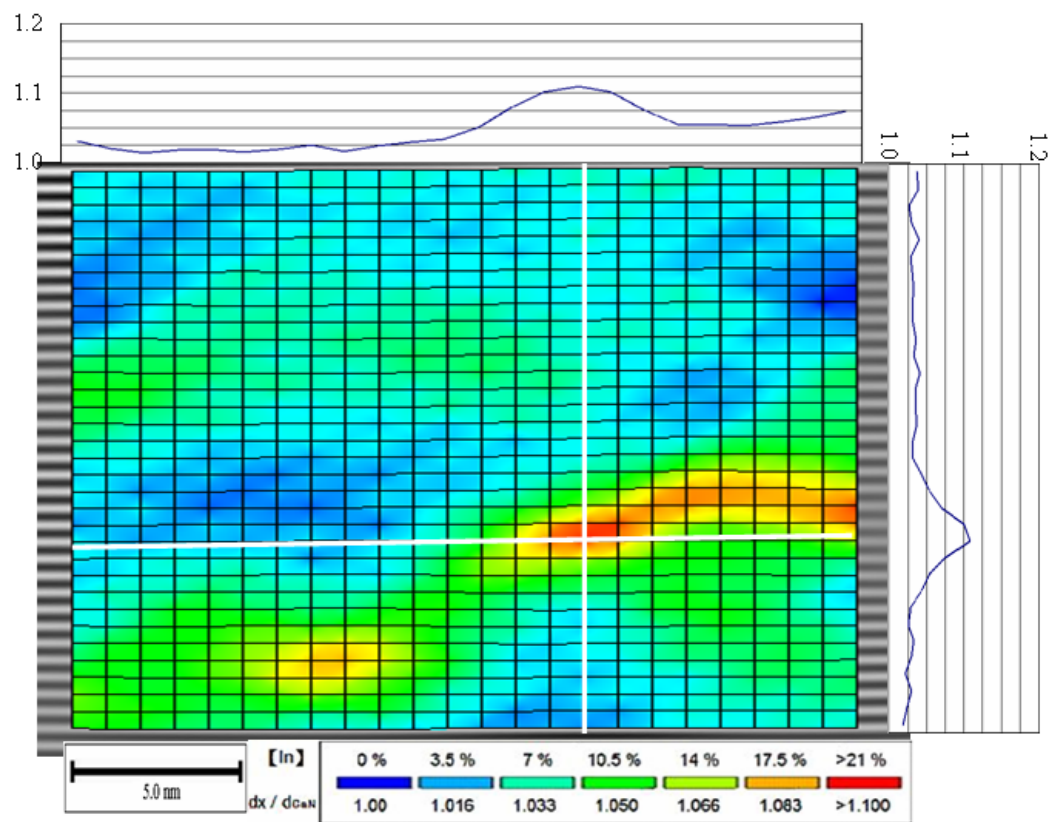


Fig. 4.3.4(e) An SSA image of 10nm-5P (the fifth well from the bottom).

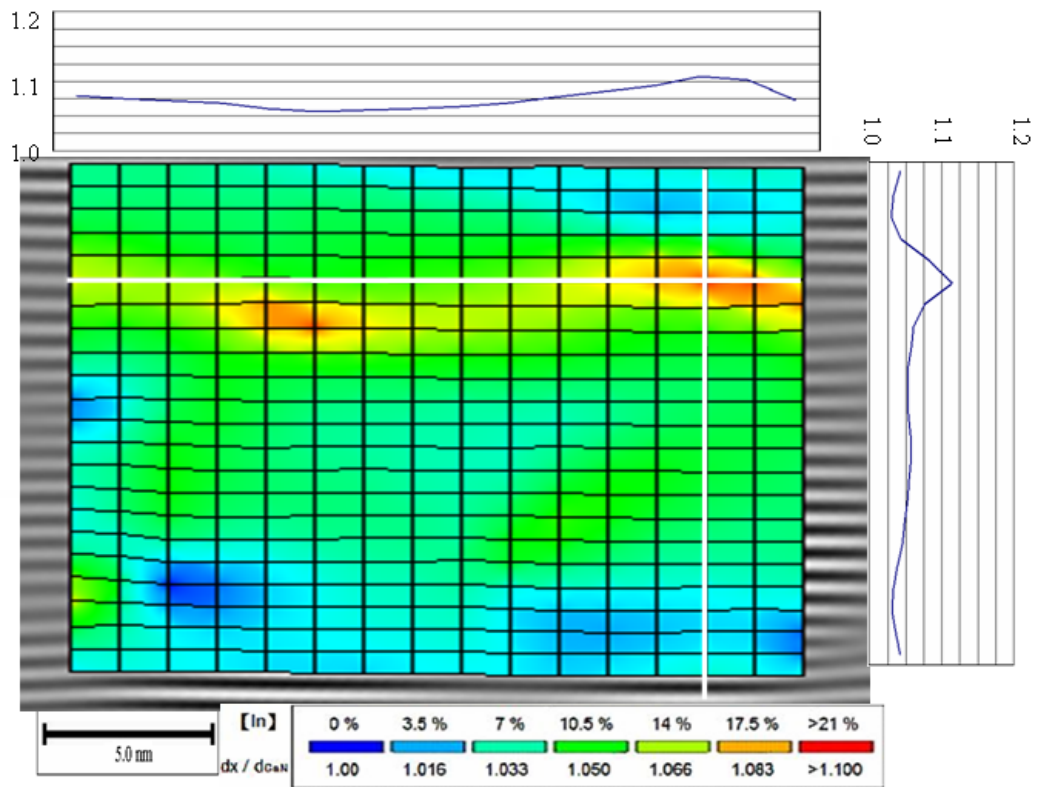


Fig. 4.3.5(a) An SSA image of 8nm-6P (the first well from the bottom).

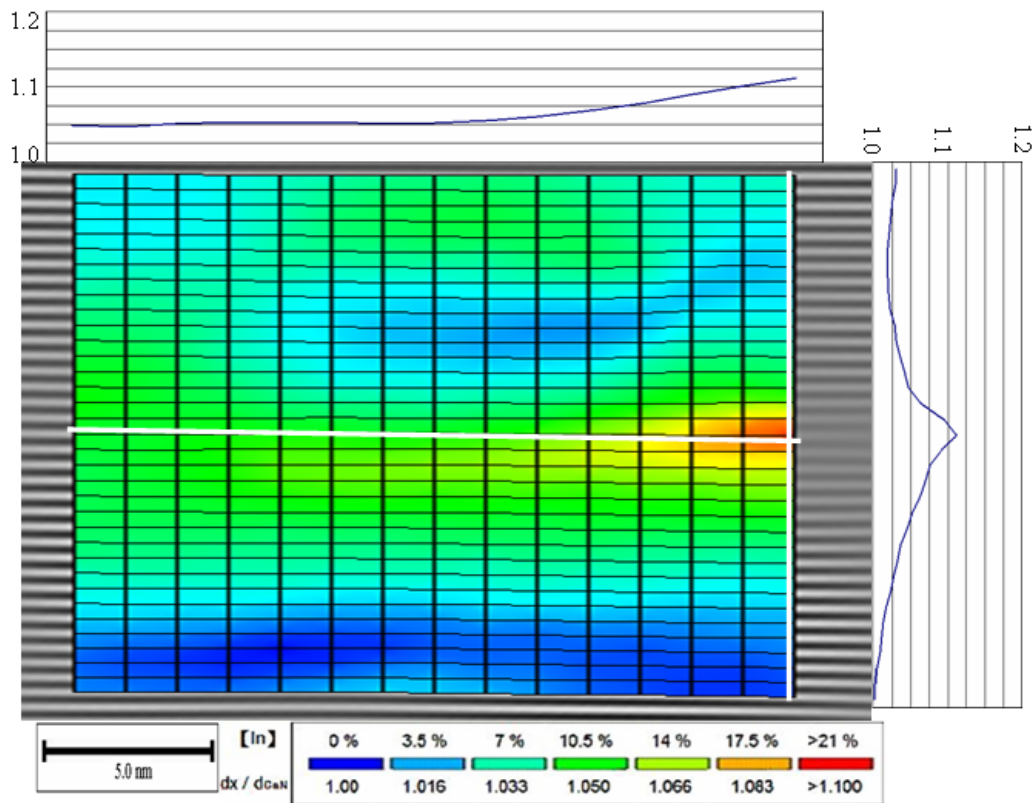


Fig. 4.3.5(b) An SSA image of 8nm-6P (the second well from the bottom).

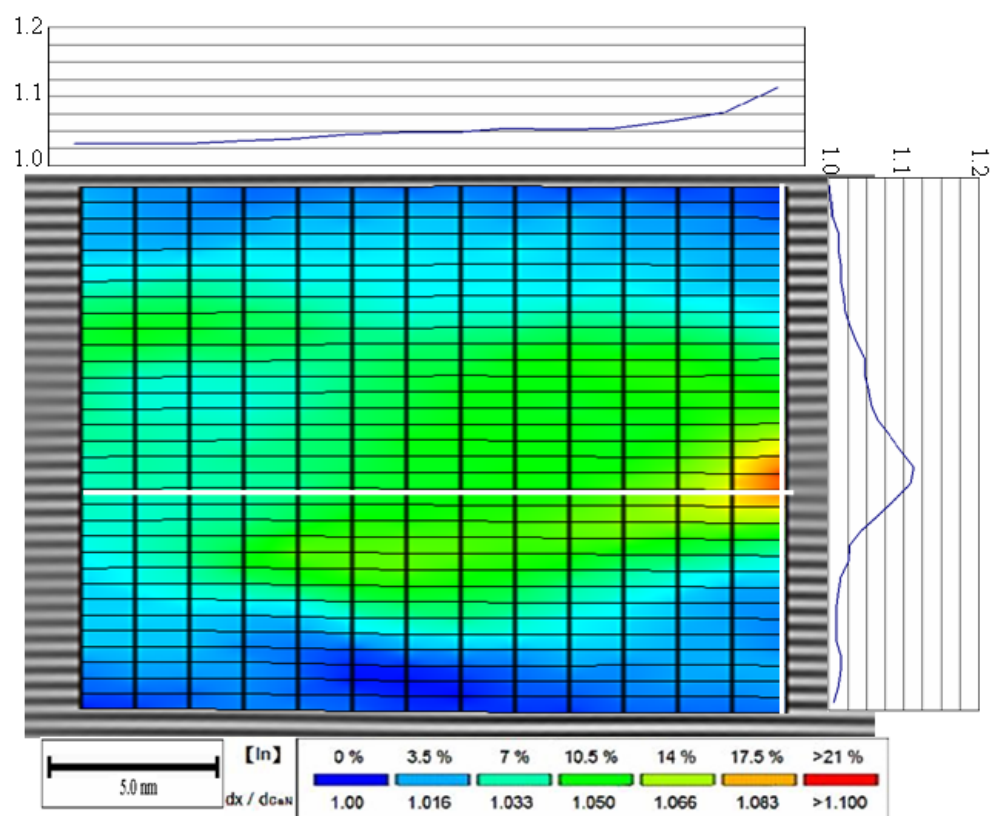


Fig. 4.3.5(c) An SSA image of 8nm-6P (the third well from the bottom).

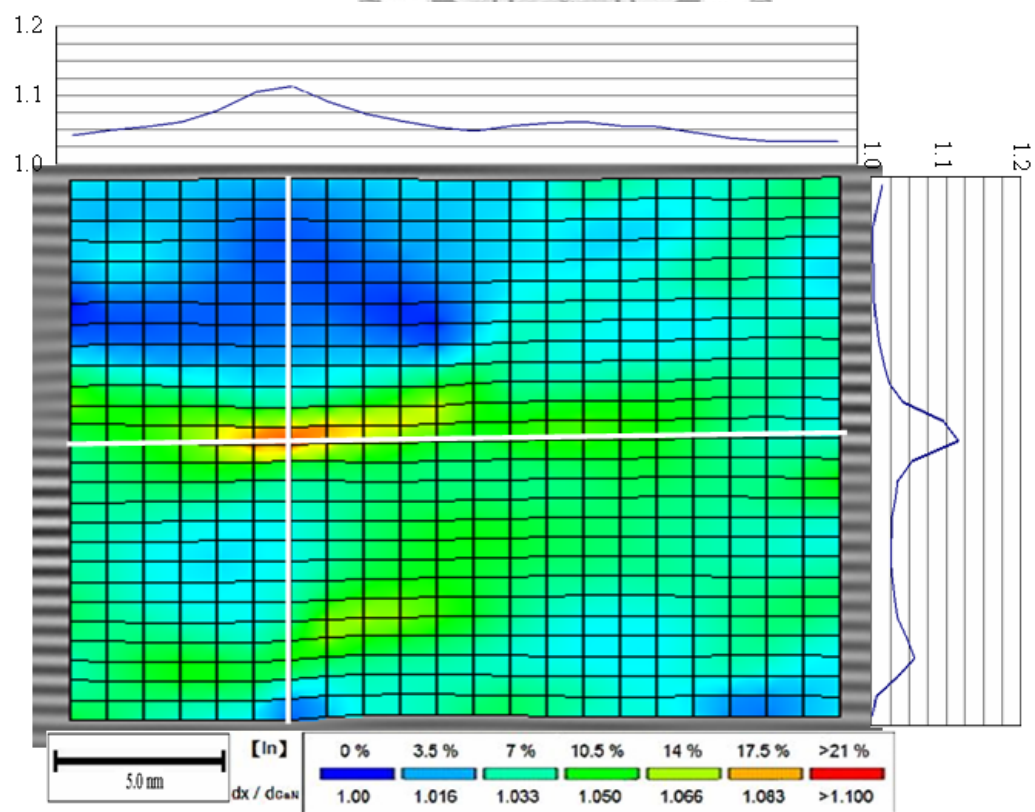


Fig. 4.3.5(d) An SSA image of 8nm-6P (the fourth well from the bottom).

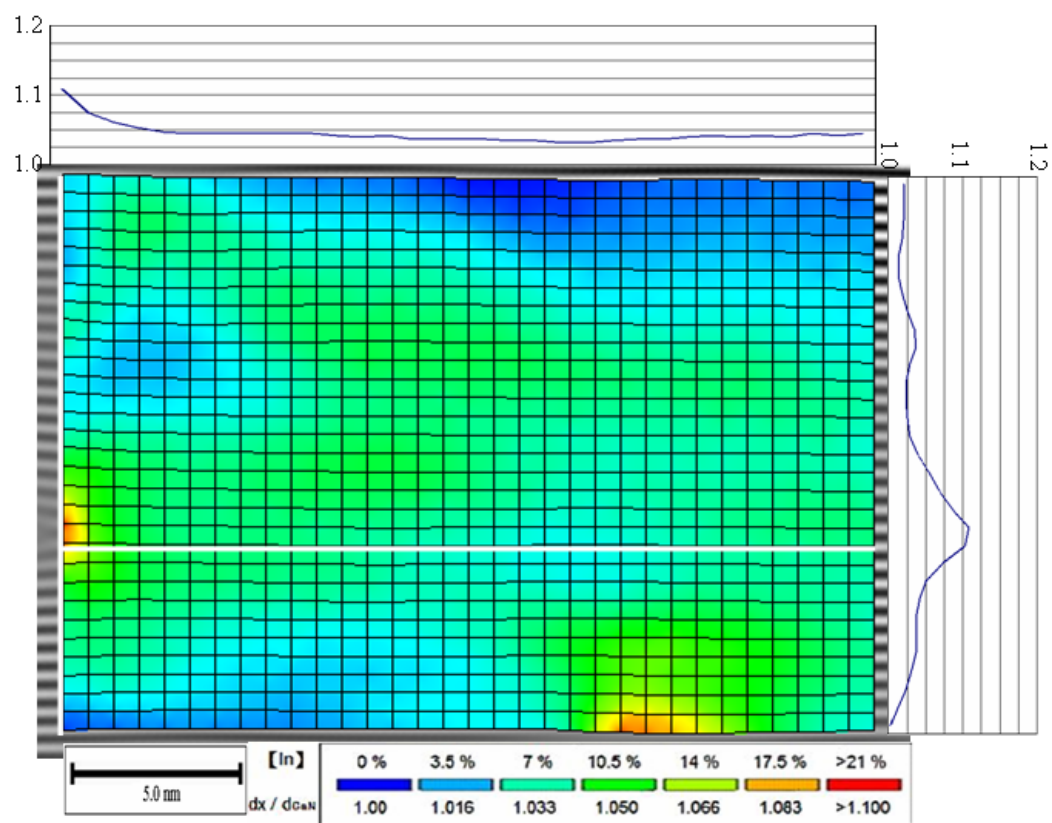


Fig. 4.3.5(e) An SSA image of 8nm-6P (the fifth well from the bottom).

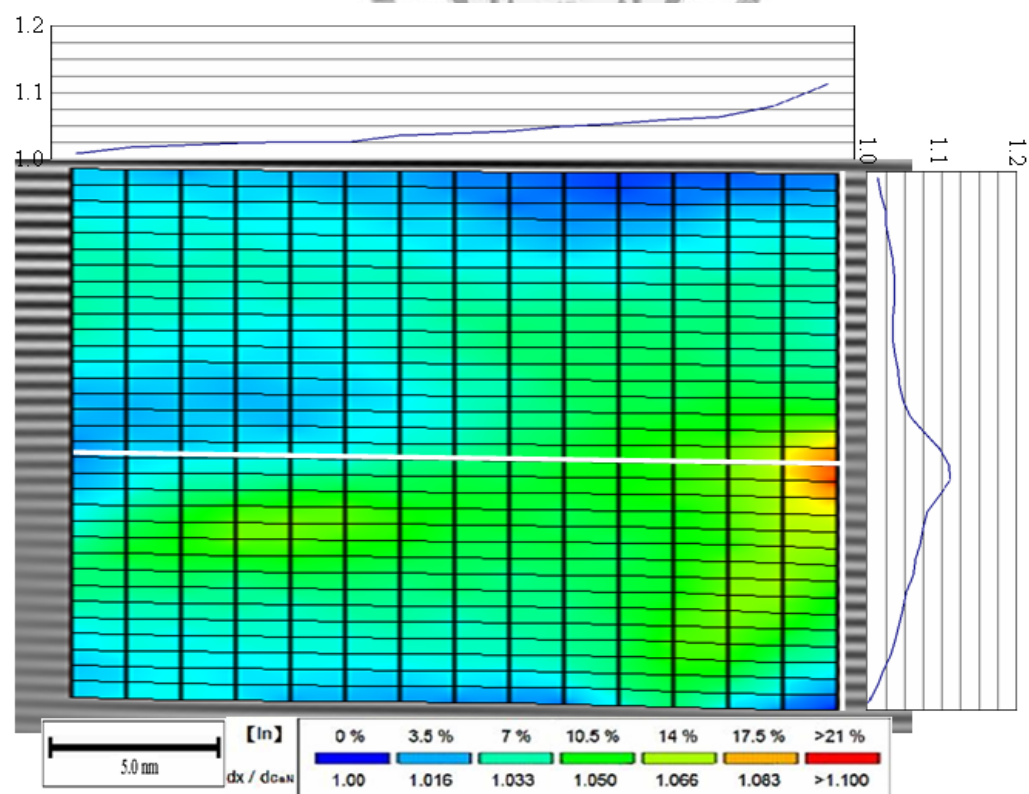


Fig. 4.3.5(f) An SSA image of 8nm-6P (the sixth well from the bottom).

Table 4.3.1 Indium composition fluctuation range (crest-to-valley) of the wells in the 10nm-5P and 8nm-6P samples.

<i>Sample</i>	<i>Layer</i>					
	1	2	3	4	5	6
<i>10nm-5P</i>	14.62	18.32	15.24	15.38	20.41	
<i>8nm-6P</i>	10.5	13.07	14.68	14.57	17.7	21.93



Table 4.3.2 Calibrated average indium contents of the wells in the 10nm-5P and 8nm-6P samples.

<i>Sample</i>	<i>Layer</i>					
	1	2	3	4	5	6
<i>10nm-5P</i>	10.08	10.23	16.03	16.29	12.92	
<i>8nm-6P</i>	12.52	12.08	12.14	11.98	11.80	11.83

Chapter 5

Conclusions

In the first part of this research, we applied HRTEM and SEM techniques to study the nanostructures of two series samples including single-heterostructures (SH) and double-heterostructures (DH). HRTEM results showed formations of indium droplets depicting a trend where the density of indium droplets decreased as the InGaN thickness decreased. In addition, SEM results showed that as the strain started to relax the surface roughness of these samples rose. RSM and PL measurements also demonstrated the variations of strain and indium composition of an InGaN layer in these two series samples. In the SH samples, InGaN with low (bottom) and high (top) indium contents can be identified. On the other hand, only a thin layer of relaxed InGaN in the middle of the DH samples can be observed. The indium composition trend, as measured by EDX, is consistent with the PL results. Owing to the above properties and sufficient absorption for solar cell applications, one can conclude that it is necessary to grow thinner and multiple InGaN layers.

The second part of this research compared the nanostructures of two InGaN/GaN multi-layers of different structures. PL measurements showed that the 10nm-5P sample only displayed a broad spectrum, whereas the 8nm-6P sample clearly showed two

spectral peaks. This result implied a better optical quality in the 8nm-6P sample than in the 10nm-5P sample. From the cross-section HRTEM images, one can see that the indium distribution was more uniform and the interfaces between the InGaN wells and GaN barriers were clearer in the 8nm-6P sample than in the 10nm-5P sample. The SSA calibrated average indium contents and indium composition fluctuation, which gave us local information about the two samples. Based on the SSA results, we find that the 10nm-5P sample has a larger indium composition fluctuation than the 8nm-6P sample. The EDX results are consistent with the SSA results. We concluded that the 8nm-6P sample (thinner InGaN thickness and thicker GaN barrier) generally had better crystal quality than the 10nm-5P sample.

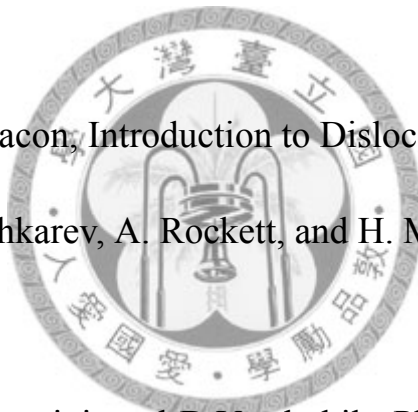


Reference

Chapter 1

- [1] S. Nakamura and G. Fasol, *The Blue Laser Diode* (Springer, Berlin, 1997).
- [2] H. Morkoç, *Nitride Semiconductors and Devices* (Springer, 1999).
- [3] J.H. Edgar, S. Stritite, I. Akasaki, H. Amano and C. Wetzel, *Gallium Nitride and Related Semiconductor* (1999).
- [4] X. Y. Sun, R. Bommen, D. Burckel, A. Frauenglass, M. N. Fairchild, and S. R. J. Brueck, G. A. Garrett and M. Wraback, S. D. Hersee, “Defect reduction mechanisms in the nanoheteroepitaxy of GaN on SiC,” *J. Appl. Phys.* **95**, 1450 (2004)
- [5] Valcheva, T. Paskova, I. G. Ivanov, R. Yakimova, Q. Wahab, S. Savage, N. Nordell, and C. I. Harris, “B implantation in 6H--SiC: Lattice damage recovery and implant activation upon high-temperature annealing,” *J. Vac. Sci. Technol. B* **17**, 1040 (1999)
- [6] S. Nakamura, *Jpn. J. Appl. Phys.* **30**, L1705 (1991).
- [7] J. H. EDGAR, S. STRITE, I. AKASAKI, H. AMANO and C. WETZEL, *Properties, Processing and Applications of Gallium Nitride and Related Semiconductor* (1999).

- [8] D. V. Lang and C. H. Henry, Phys. Rev. Lett. **35**, 1525 (1975).
- [9] S. Tomiya, E. Morita, M. Ukita, H. Okuyama, S. Itoh, K. Nakano, and A. Ishibashi, Appl. Phys. Lett. **66**, 1208 (1995).
- [10] T. Hino, S. Tomiya, T. Miyajima, K. Yamashima, S. Hashimoto and M. Ikeda, Appl. Phys. Lett. **76**, 3421 (2000).
- [11] X. H. Wu, C. R. Elsass, A. Abare, M. Mack, S. Keller, P. M. Petroff, S. P. DenBaars, J. S. Speck, and S. J. Rosner, Appl. Phys. Lett. **72**, 692 (1998).
- [12] D. Hull and D.J. Bacon, Introduction to Dislocations (2001).
- [13] G. Martin, A. Botchkarev, A. Rockett, and H. Morkoc, Appl. Phys. Lett. **68**, 2541 (1996).
- [14] F. Bernardini, Fiorentini, and D. Vanderbilt, Phys. Rev. B **56**, R10024-R10027 (1997).
- [15] S. H. Park and S. L. Chuang, J. Appl. Phys. **87**, 353 (2000).
- [16] I-hsiu Ho and G. B. Stringfellow, Appl. Phys. Lett. **69**, 2701 (1996).
- [17] S. Yu. Karpov, J. Nitride Semicond. Res. **3**, 16 (1998).
- [18] M.K. Behbehani, E.L. Piner, S.X. Liu, N.A. El-Masry and S.M. Bedair, Appl. Phys. Lett. **75**, 2202 (1999)
- [19] S. Nakamura, S. Pearton, and G. Fasol, The Blue Laser Diode, 2nd ed.



(Springer, Berlin, 2000).

[20] B. N. Pantha *et al.*, Appl. Phys. Lett. **93**, 182107 (2008).

[21] C. A. Parker *et al.*, Appl. Phys. Lett. **75**, 2776 (1999).

Chapter 2

[1] M. van Schilfgarde, A. Sher, and A.-B. Chen, J. Cryst. Growth **178**, 8 (1997).

[2] D. Gerthsen, E. Hahn, B. Neubauer, A. Rosenauer, O. Sch. on, M. Heuken, A. Rizzi, Phys. Stat. Sol. a **177**, 145 (2000).

[3] D. Gerthsen, E. Hahn, B. Neubauer, V. Potin, A. Rosenauer, M. Schowalter, Phys. Stat. Sol. c **0** 1668 (2003).

Chapter 3

[1] H. Hartono, P. Chen, S.J. Chua, and E.A. Fitzgerald, Thin Solid Films **515**, 4408–4411(2007).

